Doctoral Dissertation
Doctoral Program in Energy Engineering (35th Cycle)

Study of Ultra-low Emissions Diesel Combustion Systems by Synergetic Application of 3D-CFD and Single-Cylinder Engine

Salvatore Roggio

******

Supervisor(s):
Prof. Federico Millo, Supervisor
Dr. Andrea Piano, Co-Supervisor

Doctoral Examination Committee:
Mr. Daniel Christopher Bitsis, Southwest Research Institute
Dr. Carlo Beatrice, CNR – STEMS
Prof. José María García-Oliver, Universitat Politècnica de València
Dr. Yu Zhang, Cummins Inc.
Prof. Marco Badami, Politecnico di Torino

Politecnico di Torino
2023

Declaration

I hereby declare that, the contents and organization of this dissertation constitute my own original work and does not compromise in any way the rights of third parties, including those relating to the security of personal data.

Salvatore Roggio

2023

* This dissertation is presented in partial fulfillment of the requirements for **Ph.D. degree** in the Graduate School of Politecnico di Torino (ScuDo).

Acknowledgments

Firstly, I would like to thank PUNCH Torino S.p.A/ formerly General Motors Global Propulsion Systems for sponsoring this research activity. In particular, I would like to thank Dr. Francesco Concetto Pesce and Dr. Alberto Vassallo for their support during this research program.

I would like to thank Mr. Andrea Bianco of Powertech Engineering S.r.l. for his precious support in the development of the numerical models.

I would like to thank CMT – Motores Térmicos, Universitat Politècnica de València for supporting our research group on the optical engine analysis. In particular, I would like to express my gratitude to Prof. José Vicente Pastor Soriano, Prof. Antonio García Martínez, Dr. Carlos Micó Reche and Dr. Felipe Lewiski for their valuable and constant support.

I would like to thank my supervisor Prof. Federico Millo, for his wise guidance and constant support. Likewise, my gratitude goes to my co-supervisor Dr. Andrea Piano for his valuable suggestion and constant support during my research project. Lastly, I would like to thank all my colleagues for sharing this experience.

Abstract

Nowadays, for the diesel engine-based powertrains, the increasingly demanding CO_2 legislative targets and the need to comply with real-driving emission standards, are pushing toward an unprecedent technological innovation. In this scenario, the optimization of the combustion system can strongly minimize fuel consumption and emissions, while limiting the incremental cost due to the adoption of advanced aftertreatment systems. Regarding diesel engine, the design of the piston bowl has shown a strong impact on the air/fuel mixing process, enabling higher EGR tolerance for better soot-NOx trade-off.

During the early stages of the optimization process, the simulation codes have been assuming remarkable importance, providing a virtual test rig for the preliminary assessment of the best concept, while reducing the time and cost of the experimental tests. With this aim, a synergetic approach based on both 3D-CFD simulations and experimental tests was developed. Regarding the simulation methodology, an integrated and automated 1D-/3D-CFD coupling code was adopted. This approach featured a calibrated spray model and the SAGE chemical kinetic solver coupled with a detailed soot PM model for the in-cylinder soot mass prediction.

Thanks to the developed numerical model, the performances of different piston bowl designs for 1.6L diesel engine were investigated. Firstly, the numerical model was validated against the experimental tests that were carried out on a Single Cylinder Engine (SCE) for the baseline re-entrant bowl, showing great

accuracy both in terms of combustion and emissions. Then, two innovative piston bowl designs were investigated: a stepped-lip and a radial-bumps designs. In the stepped-lip design the protruding lip used for the baseline re-entrant bowl was replaced by a tapered lip, where the fuel injection split can improve the air utilization in the squish region. For the radial-bumps bowl, a number of radial bumps equal to injector nozzle holes was added in the outer bowl rim, aiming to mitigate the flame-to-flame interaction. These innovative designs showed an improved air/fuel mixing process, significantly reducing the fuel consumption and the engine-out soot emissions under full load and partial load engine operating conditions. Moreover, a sensitivity analysis over different engine calibration parameters showed that no further recalibration was needed with respect to the baseline calibration of the re-entrant bowl.

Once investigated the stepped-lip and the radial bumps designs, a further step in the optimization process was carried out. With this aim, to assess the potential of a synergy between these two pistons, a hybrid piston was designed. It combined a highly-reentrant sharp-stepped bowl and a number of radial bumps in the inner bowl rim equal to the injector nozzle holes. The hybrid piston was preliminary investigated through numerical simulations. Then, the numerical results were compared with the experimental data coming from an optical access engine. In this activity, the Combustion Image Velocimetry (CIV) and the OH* chemiluminescence techniques were used for the flame characterization. Then, the 2-color pyrometry KL data were considered for the soot analysis. For the direct comparison of the numerical and experimental data, a numerical methodology was developed, providing an equivalent KL in the 3D-CFD environment. Regarding the numerical analysis, the hybrid bowl has shown a strong improvement of the air/fuel mixing. This resulted in a great soot reduction potential without any fuel consumption penalties. The numerical flame evolution and the in-cylinder soot distribution showed a good agreement with the optical data. This suggested the extension of the phenomena observed in the optical

engine even under the real metal engine operating conditions. Finally, the results of the analysis were compared with experimental data of a SCE based on similar engine architecture. The experimental tests confirmed the great soot reduction potential of the hybrid bowl with respect to the conventional re-entrant bowl, while keeping comparable efficiency and NOx levels.

Contents

List of Figures

List of Tables

Abbreviations

AM	Additive Manufacturing
AMR	Adaptive Mesh Refinement
BMEP	Brake Mean Effective Pressure
BSFC	Brake Specific Fuel Consumption
BSNO$_x$	Brake Specific NO$_x$
BSSoot	Brake Specific Soot
CA10	Crank Angle at 10% of burned mass fraction
CA50	Crank Angle at 50% of burned mass fraction
CA50-90	Duration for 50-90% of burned mass fraction
CA75	Crank Angle at 75% of burned mass fraction
CA90	Crank Angle at 90% of burned mass fraction
CAD aEOI main	Crank Angle Degrees after End of Injection of Main Event
CAD aSOI	Crank Angle Degrees after Start of Injection
CAD aTDC	Crank Angle Degrees after Top Dead Center
CFD	Computational Fluid Dynamics
CIV	Combustion Image Velocimetry
DoE	Design of Experiment
ECN	Engine Combustion Network
EGR	Exhaust Gas Recirculation
EOI	End of Injection
FSN	Filter Smoke Number
GA	Genetic Algorithm
HR	Cumulative Heat Release
HRR	Heat Release Rate
ICE	Internal Combustion Engine
IMEP	Indicated Mean Effective Pressure
ISFC	Indicated Specific Fuel Consumption
ISNOx	Indicated Specific NOx

ISPM	Indicated Specific PM
IVC	Intake Valve Closure
KH-RT	Kelvin Helmholtz and Rayleigh Taylor
KL	Optical soot density
L	LOS path length
LOS	Line-of-sight
ML	Machine Learning
NL	Natural Luminosity
NTC	No Time Counter
NZE	Net Zero Emissions
PAH	Poly-cyclic Aromatic Hydrocarbons
PISO	Pressure Implicit with Splitting Operator
PIV	Particle Image Velocimetry
PM	Particulate Mimic
PSO	Particle Swarm Optimization
RANS	Reynolds-averaged Navier-Stokes
RDE	Real driving Emissions
RMZ	Radial Mixing Zone
RNG	Re-Normalization Group
SCE	Single-Cylinder Engine
SLM	Selective Laser Melting
SOI	Start of Injection
SR	Swirl Ratio
TDC	Top Dead Center
TKE	Turbulent Kinetic Energy
TVCS	Twin Vortex Combustion System
VGT	Variable Geometry Turbine
WP	Working Point
yOH	OH mass fraction
2C	2-color pyrometry technique

λ	Wavelength
$I_{b,\lambda}$	Monochromatic intensity of radiation of a black body
I_{λ}	Monochromatic intensity of radiation
ε_{λ}	Monochromatic soot emissivity
$T_{a,\lambda}$	Monochromatic apparent temperature
f_v	Soot volume fraction
τ_{λ}	Monochromatic soot transmissivity
ρ_{wall}	Wall reflectivity

Chapter 1

Introduction

1.1 Background

The global demand of passenger car and freight transportation is strongly increasing due to the growth of population and economic, resulting in higher carbon emissions. Nowadays, the transportation sector accounts for about 25% of the global anthropogenic CO_2 emissions and the highest contribution (77%) is due to the on-road vehicles [1]. In the absence of further policy action, the CO_2 emissions from transportation will significantly growth over the next 30 years. Therefore, to limit the global temperature change to 1.5°C in 2050, a significant improvement of the system efficiency and low GHG-emission technologies must be introduced in the transportation sector [1]. The electrification and hybridization have been considered as potential solution for replacing the conventional Internal Combustion Engine (ICE). This is the current trend for light-duty sector, while for medium- and heavy-duty applications the massive electrification is not a near-medium term solution. In this case, the weight of the batteries, the autonomy requests, the costs, and the lack of infrastructures can significantly affect the market penetration. Also, the manufactures and research groups are investing on the development of new technologies, such as innovative combustion modes [2,3] and alternative fuels (e.g., biofuels, hydrogen) [4–6], aiming to achieve the more stringent emissions targets. As shown in **Figure 1–1**, in the Net Zero Emissions (NZE) scenario, the share of oil in road transport demand decreases to 75% by 2030 thanks to the introduction of electricity, biofuels and hydrogen [7].

Nevertheless, by 2030 ICE vehicles still account for nearly 80% of the stock of cars, meaning that efficiency improvement remains critically important [7].

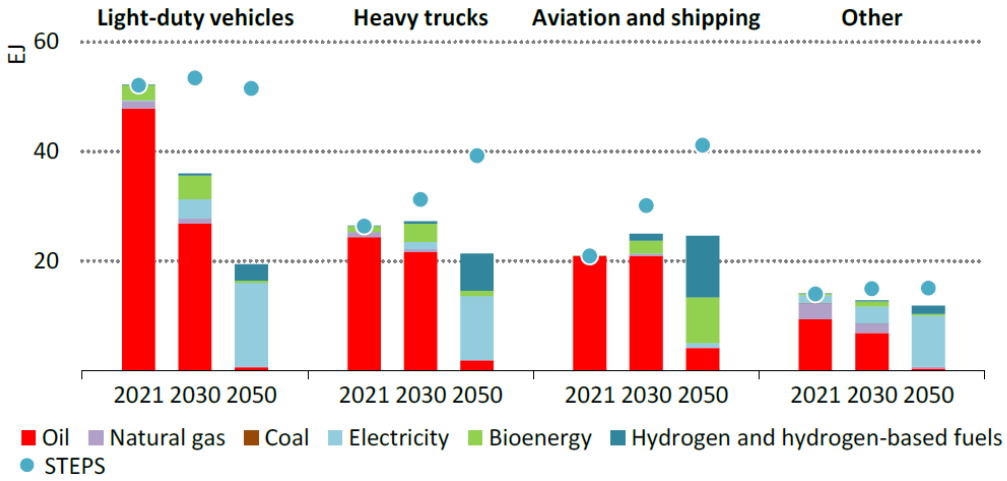

Figure 1–1: NZE Scenario: final energy consumption in transport by source and mode. From [7].

In this framework, although the number of new diesel vehicles decreased sharply, they will still be part of the market in the next years, especially in the light commercial vehicles and heavy-duty segments [8]. Regarding the emissions targets, diesel engines coupled with the recent aftertreatment systems technologies can respect the more stringent NOx targets under real-driving (RDE) conditions, without any significant fuel consumption worsening [9]. Nevertheless, the incremental cost due to after-treatment can significantly affect the total cost of diesel engine, affecting its market penetration [10–12]. Therefore, to mitigate the cost, the in-cylinder control of pollutant emissions will still play a crucial role. In this context, the combustion system design can significantly reduce the fuel consumption and the pollutant emissions [13].

1.2 Diesel piston design and optimization

The combustion chamber design plays a fundamental role in the generation of the flow field that supports the combustion process. The modern diesel combustion systems feature a flat cylinder head with a centrally mounted injector and a cavity on the piston (i.e., bowl volume) where the main part of the

combustion occurs. Adopting a flat cylinder head the mechanical strength is increased and a higher peak cylinder pressure is tolerated at the high loads. Also, the proper design of the piston bowl enhances the air/fuel mixing rate, thus leading to benefits on terms of emissions and fuel consumption [14]. **Figure 1–2** shows a scheme of the diesel piston features. The region outside the bowl volume is referred as squish volume and it is assumed to be unavailable for the combustion process [14]. It is common to evaluate the potential air utilization adopting the k-factor definition: the ratio between the bowl volume and the total volume at TDC (bowl volume + squish volume). Hence, the higher is the k-factor the higher is the air utilization. The central region below the injector is called piston pip and it is designed to increase the mixing in a region with reduced flow velocity [14]. For light-duty diesel engine, the bowl usually shows a reentrancy: the top of the bowl has lower diameter of the maximum bowl diameter, defining a piston lip [13], as shown in **Figure 1–2** – a. This design is typical for light-duty engines, usually operating at low-medium loads in urban cycles, for which the kinetic energy of the spray is not able to drive the mixing process and the piston design coupled with the bulk flow motion become crucial [13]. In these conditions, the re-entrant bowl can effectively improve the mixing behavior due to the higher swirl amplification and turbulent generation [15]. Indeed, the smaller diameter of the bowl with respect to the cylinder amplify the rotational velocity due to the momentum conservation. Also, a higher squish flow intensity is observed that results in higher turbulent generation with respect to an open bowl shape [15]. Conversely, for heavy-duty diesel engines, the higher loads results in longer injection durations, and the mixing is driven by the spray [13]. For this application, an open bowl shape is commonly used, as shown in **Figure 1–2** – b. The absence of the lip in the outer bowl rim provides a more robust piston design to face the high thermal loads. Also, these combustion systems are usually a negligible swirl ratio (quiescent), thus avoiding the need of a lip [13].

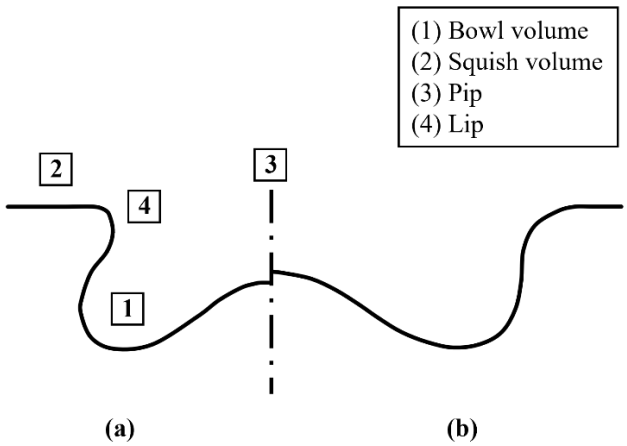

Figure 1–2: Scheme of the piston features. (a) Re-entrant bowl; (b) open bowl.

For the optimization of the combustion process, the best coupling among piston design, in-cylinder flow motion and spray characteristics should be considered. Due to the complexity of these interactions, a wide variety of solutions can be reached. Nevertheless, some main parameters are generally considered for the piston design optimization: the piston bowl diameter, the reentrancy, the lip/pip shape, and the squish height [14]. For the piston design, the bio-inspired algorithms, such as the genetic algorithm (GA) and the particle swarm optimization (PSO), can be used to find the optimum design strategies [16,17]. Nevertheless, these techniques require many generations to reach the convergence, increasing the computational times. Instead, the Design of Experiment (DoE) approach can run different configurations in parallel, leading to shorter times if sufficient computing resources are used [18]. Also, the machine learning (ML) potentials were used for the piston optimization, providing a pathway to transform complex physical processes into compact information [19,20]. In this case, the CFD results from DoE and GA analysis can be used as training dataset for the ML method.

Among the innovative piston designs, in this work the stepped-lip and radial-bumps pistons were investigated. Additional details about the geometrical features, the basic principles and the available results in literatures are provided in the following sections. Also, in the last years, a higher degree of geometrical complexity was possible for piston design thanks to the recent progress in the Additive Manufacturing (AM) techniques [21–23]. Thanks to AM approach an

innovative hybrid piston was designed, combining the stepped-lip and radial-bumps geometries. The details on the hybrid bowl are hereafter reported.

1.2.1 Stepped-lip design

In this piston design the protruding lip used for the re-entrant bowl was replaced by a chamfered lip. The basic idea is to direct the injected fuel toward the chamfered lip, creating two counter-rotating toroidal vortices and enhancing the air/fuel mixing [24]. Nevertheless, the beneficial flow structures induced by the stepped-lip design are strongly related to the spray targeting optimization [24]. Indeed, as observed by Bush et al. in [25], at partial load, a faster heat release rate in the late combustion phase (i.e., 50-90% of the burned mass fraction) can be reached only for a limited range of injection timing. An optical investigation through the combustion image velocimetry (CIV), highlighted a strong correlation between the enhanced burn rate and the formation of long-lasting toroidal vortices due to step geometry [26]. Also, the stepped-lip bowl can be beneficial for soot reduction, since the more evenly distributed fuel within the bowl and in the squish region increases the oxidation rate [27]. The Engine Combustion Network (ECN) adopted the soot natural luminosity (NL) technique for the assessment of a stepped-lip design [28]. This concept highlighted a strong reduction of soot NL with respect to the re-entrant bowl. In the last decades, one of the main alternatives to the conventional re-entrant bowl was represented by the stepped-lip combustion system [9,27,29–31] and **Figure 1–3** shows the stepped-lip piston profiles for different OEMs. In 2011 Ricardo patented the "Twin Vortex Combustion System" (TVCS) [29] which features a stepped-lip design. This piston design showed a strong improvement of the mixing process, enabling high EGR tolerance for NOx control coupled with high injection pressure for soot reduction [32]. Also, the TVCS design has shown the potential to reach the emissions targets even without any aftertreatment system for a JCB 4.4L off-highway diesel engines, as stated in [33]. In 2011, Styron et al. studied a stepped-lip geometry for a Ford 6.7L diesel engine [30]. This design showed a significant improvement of the fuel consumption and the soot-NOx trade-off, under low-speed and partial-load engine operating conditions [34]. Also, this design showed a reduced heat transfer losses with respect to the re-entrant bowl due to the lower bowl surface and the reduced flame propagation toward the liner [30]. A reduction in terms of heat transfer losses was also claimed by Toyota that designed a stepped-lip piston for a 2.8L diesel engine [31]. This heat loss reduction contributed to increase the fuel efficiency with respect to the re-entrant bowl. In

2013, the potential of the stepped-lip bowl in terms of soot reduction was also investigated by Doosan with its "Ultra-Low Particulate Combustion" [27]. This piston design was implemented in 2.4L off-road diesel engine and it was able to reach the emissions targets without any PM aftertreatment device. In 2016, the Daimler stepped-lip bowl was adopted for the Mercedes Benz OM654 2.0L diesel engine [35] and it was the first application of a stepped-lip design for a passenger car. This piston adopted an annular recess step instead of a tapered lip, enabling high air utilization in the squish region and reducing the heat transfer losses toward the cylinder wall. Therefore, a strong reduction in terms of soot and BSFC was reported with respect to the previous OM651 engine that implements a conventional re-entrant bowl.

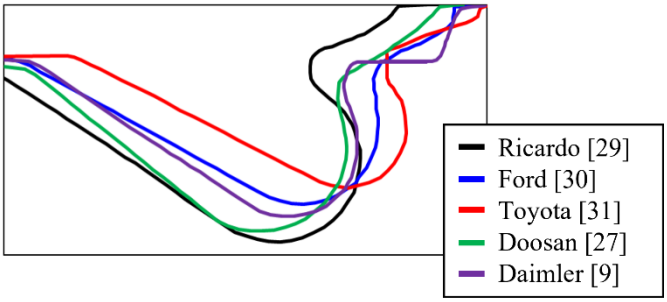

Figure 1–3: Stepped-lip piston profiles for different OEM.

1.2.2 Radial-bumps design

For low-swirl heavy-duty diesel engines, that typically feature an open bowl shape [14], the flame-to-flame interaction leads to lower combustion rate and higher soot formation [36]. This was overcome by Volvo in 2013 with the WAVE bowl [37], adding radial protrusions in the regions where two adjacent flames collide, as shown in **Figure 1–4**.

Figure 1–4: Volvo's WAVE piston. From [38].

The WAVE bowl flame evolution was investigated through simulations and optical techniques by Eismark et al. in [38]. The radial bumps provide a different collision angle of two adjacent flames, reducing the formation of rich stagnation zones and enhancing the flame velocity toward the piston center in the Radial Mixing Zone (RMZ), as also reported in **Figure 1–5**. The more intense RMZ results in higher air mixing onto the flame front. When the RMZ detaches from the piston wall, the trailing edge of the flame has higher air entrainment (see **Figure 1–5**), increasing the burn rate. This improved mixing process promotes a higher heat release rate in the mixing-controlled combustion phase with respect to the re-entrant bowl, providing up to 1% thermal efficiency increment [5].

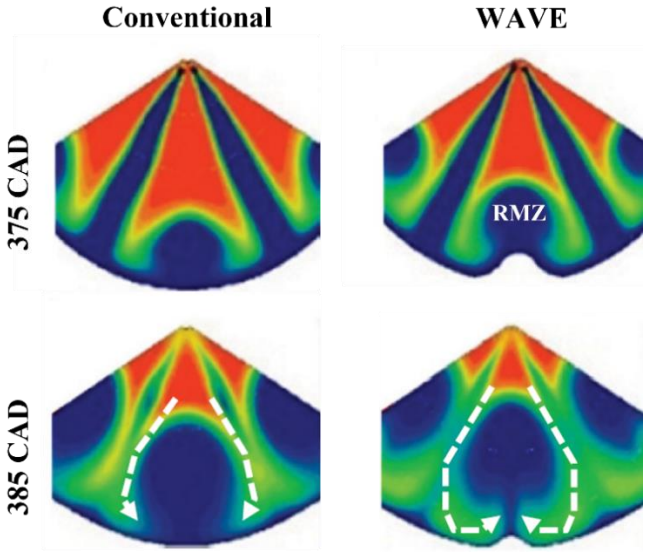

Figure 1–5: Development of the O2 field in double-sector CFD simulations of combustion. Left: conventional; right: WAVE. Adapted from [38].

Experimental tests on a Single Cylinder Engine (SCE) were carried out over different partial load working points, as reported in [38]. In this work, the WAVE bowl showed an improved soot-NOx trade-off, leading up to 80% soot reduction than with a conventional bowl. Also, this concept showed a further soot reduction by using an oxygenated fuel, controlling the NOx level with a higher EGR rate [39]. Recently, an optical investigation on the WAVE bowl was carried out, considering different diesel-like fuels [40]. The results highlighted that there is a strong correlation between the fuel density and the flame-to-wall interaction. Although the WAVE piston showed great potentials in terms of soot and fuel consumption reduction for a heavy-duty application, additional investigations are required to assess its effect for a swirl-supported light-duty diesel engine. For this application, the higher swirl ratio could affect the RMZ evolution, and the higher reentrancy could increase the flame recirculation toward the piston center, in the tumbling vortex. The adoption of a radial-bumps bowl was recently investigated for a light-duty engine through numerical simulations [41]. This work showed an improved air/fuel mixing with respect to a conventional re-entrant bowl. At partial load, a strong improvement of the soot-NOx and BSFC-BSNOx trade-off was reported, leading to 50% soot reduction and 5% BSFC reduction [41].

1.2.3 Hybrid design

Recently, the combination of the stepped-lip and the radial-bumps geometries was investigated as a further step toward the ultra-low soot emissions piston concept [23,42]. In these works, an innovative piston bowl design (named ‘hybrid’) was presented, featuring both a highly re-entrant sharp-stepped bowl and a number of radial bumps equal to the nozzle holes in the inner bowl rim, as reported in **Figure 1–6**.

Figure 1–6: Top view and isometric view of the hybrid piston. Adapted from [42].

Due to geometrical complexity, undercut features and durability request for a diesel engine application, a steel-based Additive Manufacturing (AM) technique was adopted. The AM oriented activity for the development of this design was shown in [42] and it is here briefly reported. The powder bed based Selective Laser Melting (SLM) technique required supports made by the same material of the component itself to avoid the collapse of the not self-supported features during the printing process. The AM design aims to reduce the number of this support, saving time/cost of the production and avoiding supports over unreachable areas. With this aim, the number of horizontal surfaces was reduced, adopting surfaces with 45° tilt angle. This design guideline allowed the printing of self-supporting walls as the inner skirt ribs and oil gallery. More in detail, the inner area of the piston was topologically optimized based on the different load conditions and constraints. **Figure 1–7** – a shows the inner skirt topological optimization to handle the piston during the printing process and to support the combustion loads. Also, a lattice structure was developed for the oil gallery, as highlighted in **Figure**

1–7 – b. The open cell frame of this structure highlighted the best compromise in terms of light weighting and oil recirculation.

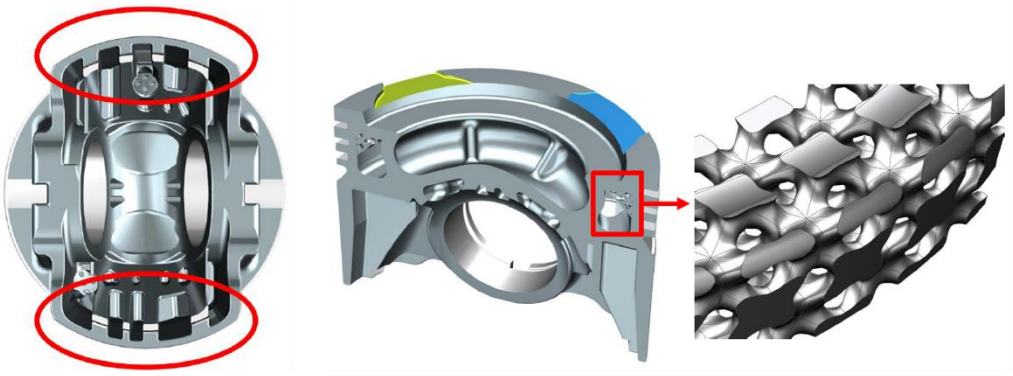

Figure 1–7: (a) Inner skirt topology optimization; (b) oil gallery open cell lattice structure. Adapted from [42].

Figure 1–8 shows an overview of the AM piston printing process sequences and the printing direction. The piston was printed layer-by-layer from the piston bottom to the piston bowl surface to facilitate the post-process operations. Then, a stress-relieving heat treatment was done, and the piston was removed from the printer platform. Finally, the supports of the structure were removed, and a further machining was carried out to increase the piston surface finishing.

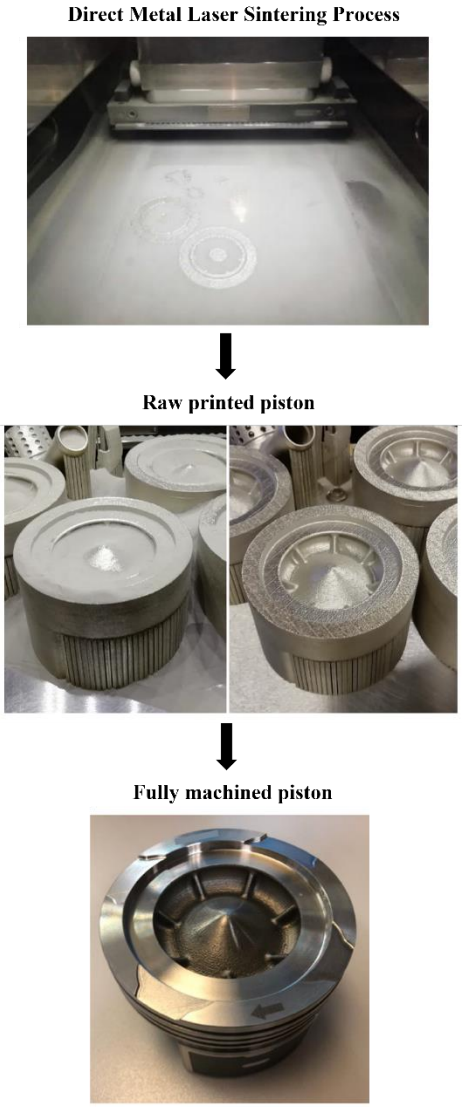

Figure 1–8: AM piston during the printing process. Adapted from [43].

The experimental tests on SCE showed for this innovative concept a significant soot reduction with any fuel consumption worsening, over different operating conditions [42,43]. A similar piston design was investigated by meaning of a single-cylinder optical access engine, providing further understanding on the flame evolution and soot process [44,45]. In particular, a higher flame reverse flow and faster late-cycle oxidation were observed with respect to a conventional re-entrant bowl [44]. Also, a higher soot oxidation rate in the late combustion

phase was highlighted, considering different engine load, fuel injection parameters and EGR rates [45]. Recent studies were focused on the combination of optical data and 3D-CFD simulations for the characterization of the flame and the soot formation/oxidation processes [46,47]. In this context, the simulation tool has the key role of virtual test rig for additional piston optimization studies, due to the high predictive capabilities and the reduced costs.

1.3 Research activity workflow

In this research activity, the performance of different piston bowl geometries for a 1.6L diesel engine was investigated by means of a synergetic approach based on both 3D-CFD simulations and experimental tests. Regarding the simulation methodology, an integrated and automated 1D-/3D-CFD coupling approach was adopted which includes a calibrated spray model and detailed chemistry. Once the numerical model was validated considering a conventional re-entrant bowl, two innovative bowl geometries were numerically investigated: a stepped-lip and a radial-bumps bowl. Firstly, the in-cylinder flow field and mixing process were investigated under non-reacting conditions for each combustion system. Then, the combustion simulations were carried under two different engine operating conditions, both at full load and part load. Additionally, a sensitivity analysis over different engine calibration parameters was carried out, providing further guidelines about the needs of the proposed designs in terms of engine calibration parameters, such as injection timing, swirl ratio, EGR rate and rail pressure. Once assessed the combustion improvement due to the stepped-lip and radial-bumps bowls, a further step on the combustion system optimization was carried out. To understand if there are synergies between these two pistons, an innovative hybrid piston was designed. The hybrid bowl combined a highly-reentrant sharp-stepped bowl and a number of radial bumps in the inner bowl rim equal to the injector nozzle holes. The hybrid bowl was firstly investigated through 3D-CFD simulations to assess the mixing and the combustion process. To maximize the potential benefits provided by the innovative hybrid piston bowl, a spray targeting optimization was carried out considering different injector protrusions and two swirl ratio levels. Then, the numerical results were compared against the experimental data coming from an optical access engine. The CIV and OH* chemiluminescence techniques were used for the characterization of the flame structure. Then, the 2-color pyrometry KL technique was adopted for the investigation of soot. To directly compare the numerical and experimental data, a numerical methodology was developed, providing an equivalent soot KL also in

the 3D-CFD environment. In the framework of a collaboration between PUNCH Torino S.p.A/ formerly General Motors Global Propulsion Systems and CNR – STEMS, an experimental activity was carried with a single-cylinder engine based on similar architecture and piston designs as the ones used in the numerical analysis. The results of the experimental campaign were used to experimentally confirm the potential benefits provided by the innovative hybrid piston bowl.

Chapter 2

Test case and methodology

2.1 Engine test case

The numerical analysis was carried out for a passenger car diesel engine whose main features are listed in **Table 2–1**. The engine is a 4-cylinder turbocharged compression ignition engine, featuring a state-of-art common rail fuel injection system with the latest generation of 8-hole solenoid injector with a maximum rail pressure of 2000 bar.

The baseline engine implements a conventional re-entrant piston bowl as highlighted in **Figure 2–1** – a. Then, different innovative geometries were investigated: the stepped-lip design (**Figure 2–1** – b), the radial-bumps design (**Figure 2–1** – c) and the hybrid design (**Figure 2–1** – d) which combines both a recess step and radial protrusions in piston bowl rim.

Table 2–1: Test engine main features.

Cylinders #	4
Displacement	1.6 L
Bore x Stroke	79.7 mm x 80.1 mm
Compression ratio	16:1
Baseline piston type	re-entrant
Turbocharger	Single-Stage with Variable Geometry Turbine (VGT)
Fuel injection system	Common rail Max Rail Pressure 2000 bar
Maximum power	100 kW @ 4000 rpm
Maximum torque	320 Nm @ 2000 rpm

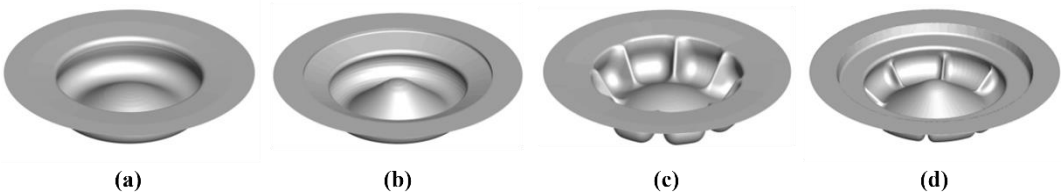

Figure 2–1: Piston bowl geometries under investigation. (a) Re-entrant; (b) stepped-lip; (c) radial-bumps; (d) hybrid.

Three different engine working points (WPs) were considered for the numerical analysis, as highlighted in the engine map of **Figure 2–2** and on **Table 2–2**. Two partial-loads engine operating conditions (WP1, WP2) were considered as representative of a typical type-approval driving cycle working points, while WP3 represent the rated power engine condition.

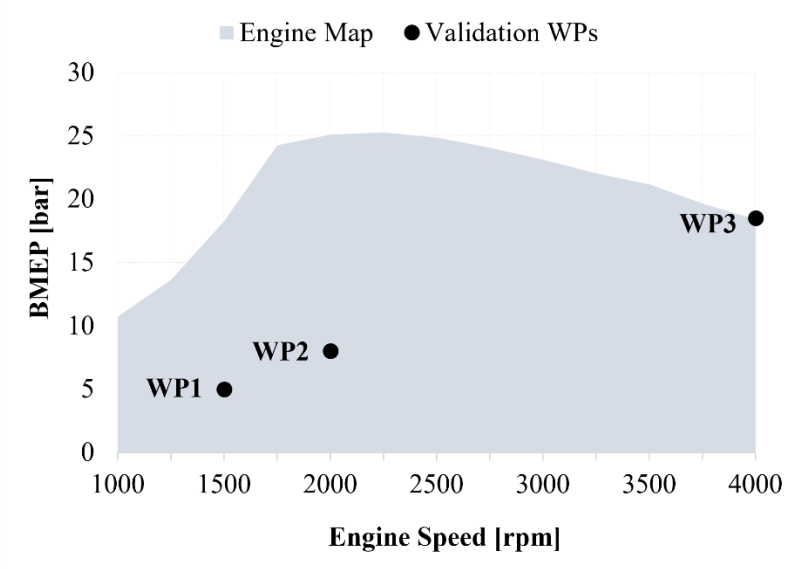

Figure 2–2: Engine working points on the engine map.

Table 2–2: Engine working points.

	Speed [rpm]	**BMEP [bar]**
WP1	1500	5.0
WP2	2000	8.0
WP3	4000	18.5

2.2 1D-/3D-CFD coupling methodology

The simulation methodology was based on 1D-/3D-CFD codes coupling, widely described in [48] and summarized in the block diagram of **Figure 2–3**. A 1D-CFD complete engine model was built in GT-SUITE and the validation results can be found in [49]. It provided the time-depending boundary conditions in terms of pressure, temperature and chemical species at intake and exhaust ports for the first step of the 3D-CFD simulation which is named 'cold flow'. This analysis was performed with the commercial software CONVERGE CFD and aimed to investigate the gas exchange process in terms of in-cylinder flow filed and thermodynamic conditions. The second step of the 3D-CFD analysis started at the Intake Valve Closure (IVC) and was the simulation of the compression stroke and the combustion process for a single sector of the full-cylinder geometry, centered along the spray axis. For the combustion simulation, a reliable injection rate profile was provided by a previously developed 1D-CFD injector model [50,51], requiring as input the rail pressure, the energizing and dwell times. Finally, the 3D-CFD combustion results were post-processed in the GT-SUITE environment, guarantying the same solution methodology of the 1D-CFD complete engine model.

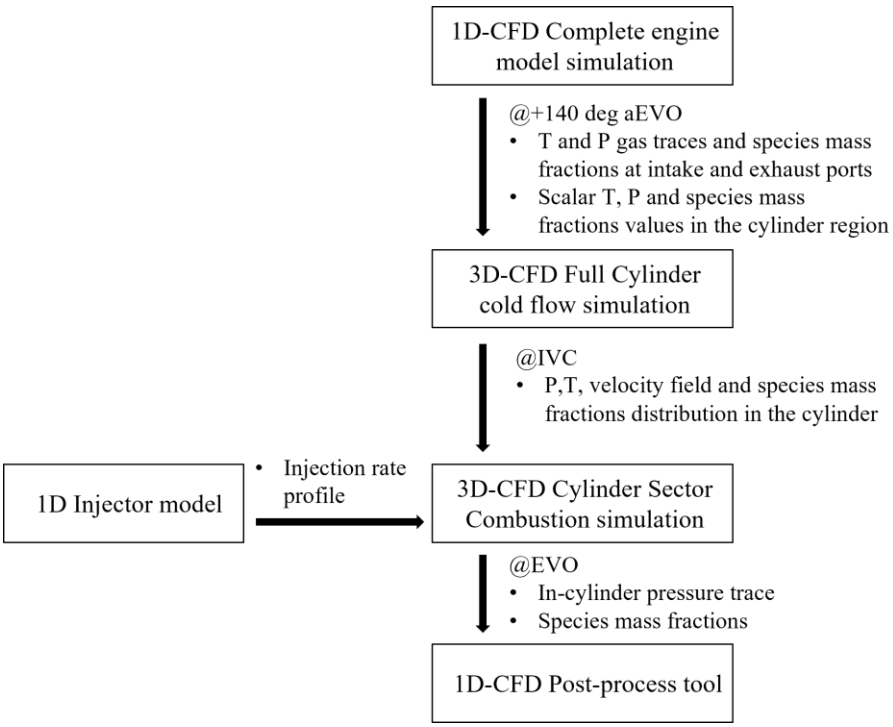

Figure 2–3: Flowchart of the simulation methodology.

2.2.1 1D-CFD models

The 1D-CFD complete engine model included all the subsystems as the turbocharger, the EGR circuit, all the pipes and volumes for the intake and exhaust systems. This engine model provided the boundary conditions for the 3D-CFD simulations. More in details, the pressure, temperature and species mass fraction boundary conditions were imposed at the intake and exhaust ports. The cylinder region was initialized in terms of thermodynamic and species concentration during the exhaust event.

For the injection modeling, only a limited set of experimental injection rates were available. Therefore, a reliable 1D-CFD model of a solenoid injector was built in GT-SUITE [50,51]. The injector model can predict the injection rate profile using as inputs the energizing time, dwell time and rail pressure.

2.2.2 3D-CFD models

For the 3D-CFD combustion simulation, the base grid size was equal to 0.5 mm for all the directions. The Adaptive Mesh Refinement (AMR) based on the velocity and temperature sub-grid criterion [52] allowed a grid refinement of 0.25 mm. In addition, a fixed embedding of 0.25 mm was also considered for the injector cone angle to properly predict the spray evolution. For the spatial discretization a second-order central difference scheme was selected, while the temporal discretization was a first order implicit Euler scheme in order to maintain stability. The conservation equations were solved by means of the Pressure Implicit with Splitting Operator (PISO) algorithm of Issa [53] and the Rhie-Chow scheme for pressure-velocity coupling [54]. The turbulence modeling was the Reynolds-averaged Navier-Stokes (RANS) based Re-Normalization Group (RNG) k-ε model [55] that guarantees the effects of flame-induced compression, expansion and rapid strain on the turbulent quantities [56]. The law-of-walls approach with standard wall function was adopted for the assessment of the boundary layers [57]. Then, the turbulent heat transfer was predicted through the O'Rourke and Amsden model [58]. The general setting in terms of mesh, turbulence and heat transfer models are summarized in **Table 2–3**.

The 'blob' injection method [59] was used for the spray model, considering a calibrated Kelvin Helmholtz and Rayleigh Taylor (KH-RT) model [59] for the breakup of droplets. A summary of the adopted spray sub-models is reported in **Table 2–4**.

Table 2–3: Mesh grid, turbulence and heat transfer models.

Fixed embedding	Injector spray cone angle
Adaptive Mesh Refinement (AMR)	Velocity, temperature sub-grid criterion [52]
Base grid	0.50 mm
Minimum grid	0.25 mm (AMR and fixed embedding)
Turbulence model	RNG k-ε model
Heat transfer model	O'Rourke and Amsden [58]

Table 2–4: Spray sub-models.

Discharge coefficient model	Cv correlation [52]
Breakup model	Calibrated KH-RT
Turbulent dispersion	O'Rourke model [60]
Collision model	No Time Counter (NTC) collision [61]
Drop drag model	Dynamic drop drag [62]
Evaporation model	Frossling model [60]
Wall film model	O'Rourke [63]

The breakup constants of the KH-RT model, the discharge coefficient and the spray angle values were used as calibration parameters to match the experimental spray penetration curves. These experimental data were obtained from constant volume vessel tests carried out at the University of Perugia [64,65] for a reference injection whose characteristics are reported on **Table 2–5**. The experimental injector current and the injection rate profile (i.e. two pilot injections and one main injection) used for the spray model calibration are shown in **Figure 2–4** – top. For the calibration of the spray model, the constant volume vessel was reproduced in the 3D-CFD environment. **Figure 2–4** – bottom compares the numerical and experimental results in terms of spray penetration for the three injections. The comparison shows a fairly good agreement for the two pilot injections, while some differences can be seen for the main injection. These differences could be related to the momentum transfer from the liquid jet to the air and the possible local variations of the air density inside the test vessel for large injection pulses. Nevertheless, considering that the size of the baseline bowl is approximately equal to 25 mm and the liquid spray penetration in the real engine operating conditions is limited, the obtained results can be considered acceptable for the study.

Table 2–5: Main characteristics of the reference injection data.

Vessel Pressure	11.28 bar
Vessel Temperature	20 °C
Rail Pressure	400 bar
ET-P2	0.215 ms
DT-P2	0.81 ms
ET-P1	0.21 ms
DT-P1	0.41 ms
ET-Main	0.32 ms

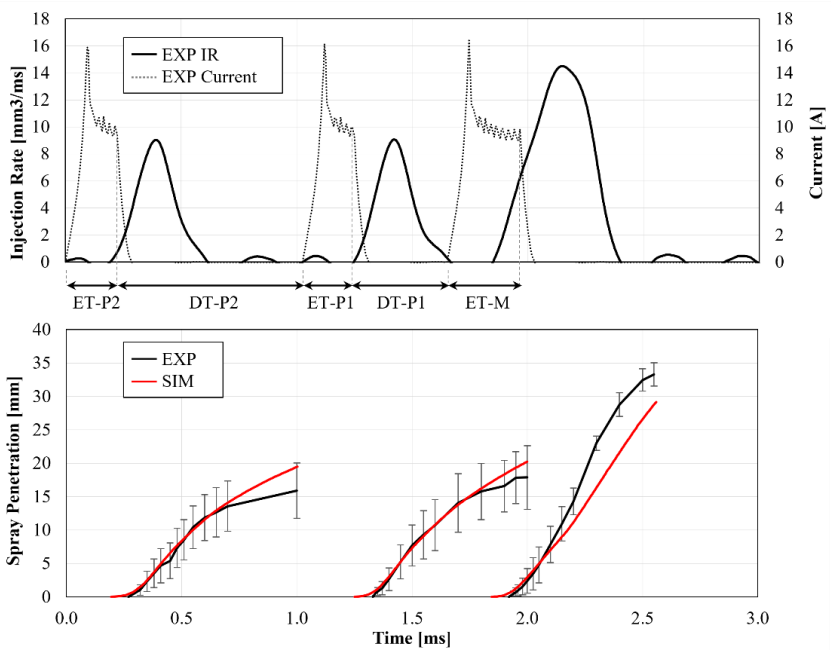

Figure 2–4: Top: Experimental injection current (dotted black) and hydraulic injection schedule (solid black). Bottom: Numerical spray penetration (red) compared with the experimental data (black) obtained for the conditions shown in **Table 2–5**.

For the combustion model, the SAGE detailed chemistry approach was adopted, featuring the Skeletal Zeuch reaction mechanism for the oxidation of N-Heptane (121 species, 593 reactions) [66]. Furthermore, the reaction scheme implements the Poly-cyclic Aromatic Hydrocarbons (PAH) soot precursor chemistry, allowing the Particulate Mimic (PM) soot model for the in-cylinder soot mass prediction [67–69]. The NOx reactions scheme is embedded in the reaction mechanism. **Table 2–6** shows the fuel surrogate, the reaction mechanism and the emissions models used in this study.

Table 2–6: Fuel surrogate, reaction mechanism and emissions models.

Fuel surrogate	N-Heptane
Reaction Mechanism	Skeletal Zeuch [66]
Species	121
Reactions	593
Soot precursor chemistry	Embedded in the reaction mechanism
Poly-cyclic Aromatic Hydrocarbons (PAH)	(A3R5-)
Soot model	Particulate Mimic (PM)
NOx chemistry	Embedded in the reaction mechanism

2.3 Model validation results

The numerical model was validated with respect to the experimental data on three different engine working points (see **Table 2–2**) for the conventional re-entrant design. The numerical results in terms of in-cylinder pressure and Heat Release Rate (HRR) are compared with the experimental data for each investigated working point on **Figure 2–5**. For the partial load WP1 (see **Figure 2–5** – a), a good agreement is obtained both in terms of in-cylinder pressure and HRR. The combustion timing is correctly captured for all the injection events. **Figure 2–5** – b shows the results for the partial load WP2. In this case the combustion duration and the ignition delay are both correctly captured by the numerical model. Lastly, also for the rated power operating conditions (WP3), as

shown in **Figure 2–5** – c, the combustion of pilot and main injection with high rail pressure are correctly predicted.

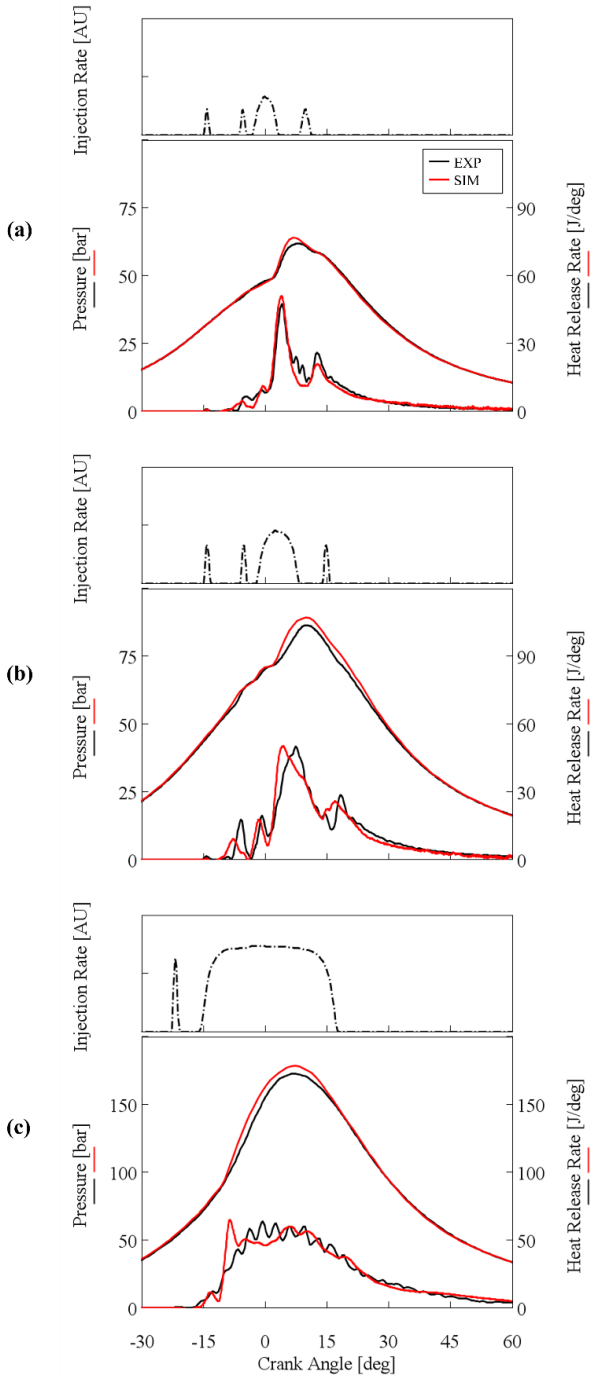

Figure 2–5: Model validation results in terms of in-cylinder pressure and Heat Release Rate. (a) WP1: 1500 RPM x 5.0 bar BMEP; (b) WP2: 2000 RPM x 8.0 bar BMEP; (c) WP3: 4000 RPM x 18.5 bar BMEP.

The predictive capabilities of the developed numerical model were also assessed in terms of the main combustion parameters. **Figure 2–6** shows a good agreement between the numerical and experimental results in terms of Peak pressure, CAD at Peak Pressure, 10-90% Combustion Duration and 50% of Mass fraction Burned (MFB50%).

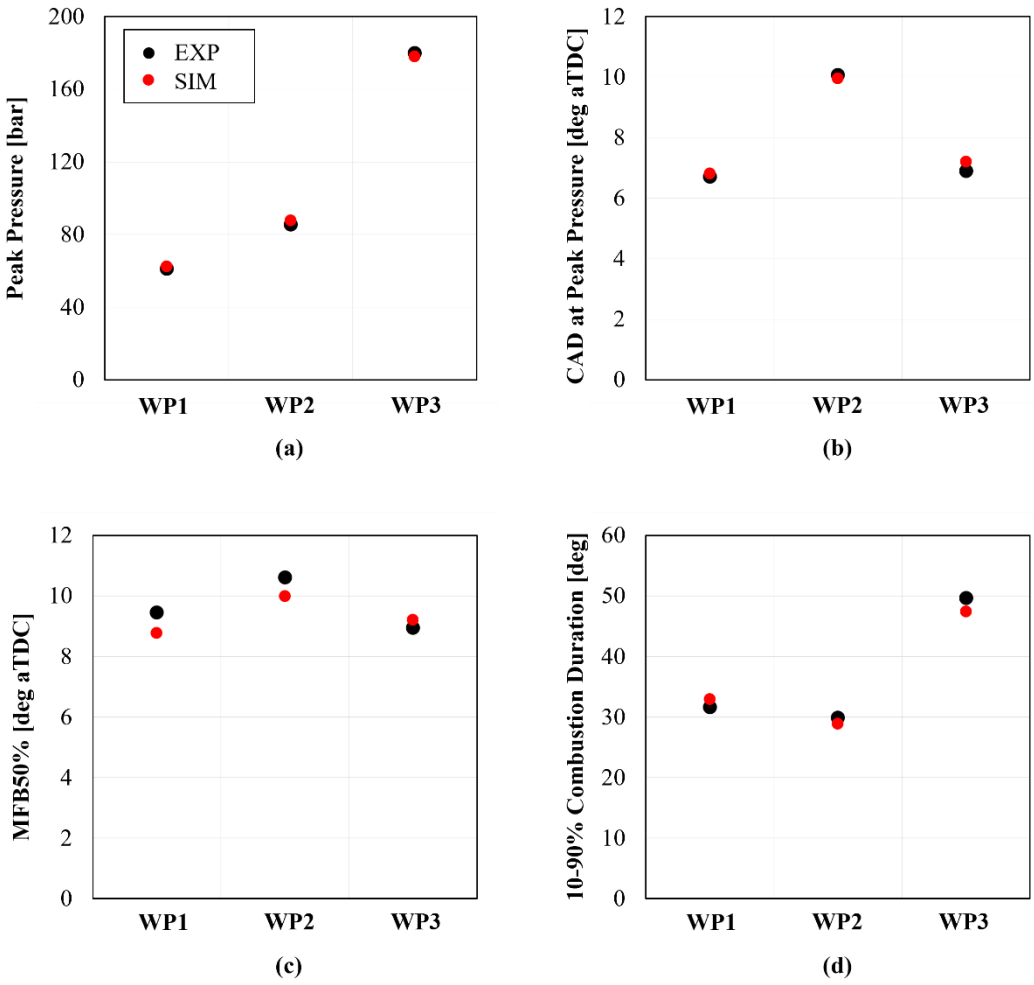

Figure 2–6: Model validation results. (a) Peak pressure; (b) CAD at Peak Pressure; (c) 10-90% Combustion Duration; (d) MFB50%.

As far as the pollutant emissions are concerned, **Figure 2–7** – a shows the NOx emissions for both the numerical and experimental data. A very good match can be observed in terms of trend over the three engine operating conditions. **Figure 2–7** – b highlights the comparison between the experimental Filter Smoke

Number (FSN) and the numerical in-cylinder soot mass at the exhaust valve opening. The experimental FSN trend is correctly captured by the numerical model.

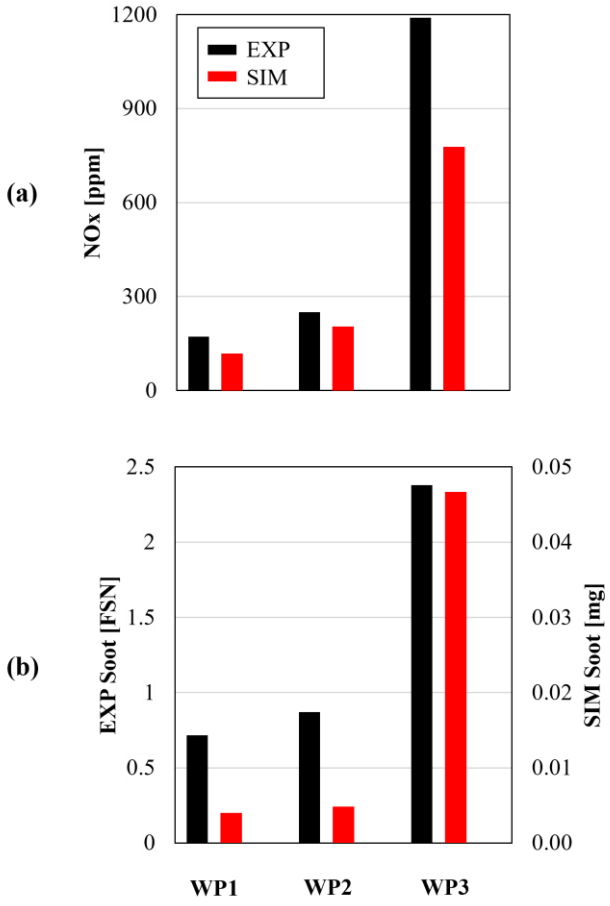

Figure 2–7: Model validation results. (a) NOx; (b) experimental FSN with respect to numerical soot mass.

2.4 Optical engine analysis

The experimental tests were performed on an optically accessible single cylinder engine, based on the same architecture as the engine used for the numerical analysis. The main features of the optical engine are summarized on **Table 2–7**. The stroke, bore and the cylinder head were kept equal to the original multi-cylinder platform. More details concerning the facility can be found in [45]. It is worth to note that the compression ratio of the engine is lower than the one

used in the simulations, since a lower position of the piston rings is required with respect to the conventional engine to avoid the lateral optical accesses when the piston is at the TDC.

Table 2–7: Optical engine main features.

Cylinders #	1
Displacement	402 cm^3
Bore x Stroke	80 mm x 80.1 mm
Compression ratio	12.5:1 (re-entrant)
	11.5:1 (hybrid)
Valve #	4

The instantaneous in-cylinder pressure was measured by means of a piezoelectric pressure transducer (AVL GH13P) and the signal was used for the calculation of the HRR. To this aim, an in-house tool which is based on the first law of thermodynamic was developed [70]. It is applied to the in-cylinder volume when the valves are closed and considers the wall heat transfer, the blow-by and the mechanical deformations which have a significant impact for an optical engine. A detailed description of the engine can be found in [71].

The optical access was based on the use of the Bowditch piston, equipped with a fully transparent piston head to mimic the flow dynamics of the original metal engine, as shown on **Figure 2–8**. Two different piston geometries were used, as highlighted in **Figure 2–9**. The first one (see **Figure 2–9** – left) is a conventional re-entrant bowl comparable with the one used in the baseline engine showed in **Figure 2–1** – a. The second one (see **Figure 2–9** – right) combines two different geometries: one half is the hybrid geometry adopted for the metal engine as shown on **Figure 2–1** – d, which include both annular recess step and the radial bumps; the other half of the piston features only the recess step. Nevertheless, to reduce the interaction among the different layout which is significant in the periphery of the bumps region, the central sector of the radial bumps side

(highlighted in red on **Figure 2–9**) was considered for the experimental investigation.

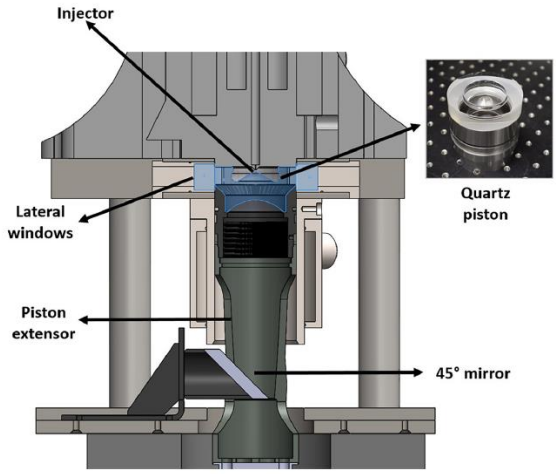

Figure 2–8: Optical engine representation and fully-transparent piston.

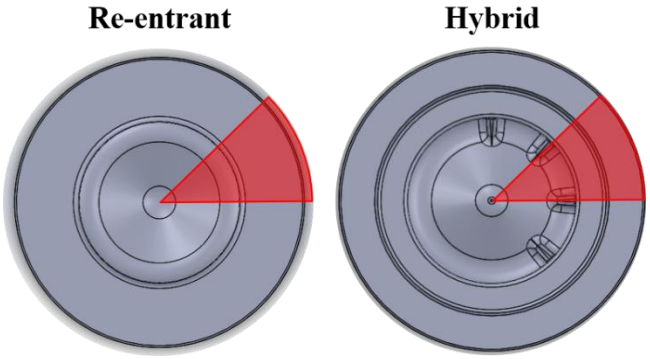

Figure 2–9: Piston bowl geometries adopted for the optical engine. Left: re-entrant; right: hybrid.

The engine load and speed were controlled by means of a Schenck electric dynamometer (220kW and 562nm). In addition, the test cell allowed the control of the intake air pressure and temperature. A screw compressor was used to pressurize the air which was dried and heat before reaching the intake ports, while a backpressure regulator was used to control the exhaust pressure. The engine was also equipped with settling chambers just upstream and downstream the engine to avoid the pressure pulses.

The experimental tests were carried out at 1250 RPM x 4.5 bar IMEP and due to the different compression ration among the investigated combustion systems (see **Table 2–7**), the intake pressure and pressures were adjusted to reach similar in-cylinder thermodynamic conditions for both cases, as shown in **Figure 2–10**. The differences in terms of intake pressure, intake temperature and air mass flow rate are highlighted on **Table 2–8**. Moreover, the exhaust pressure was also controlled to keep a constant difference of 0.2 bar with respect to the intake line.

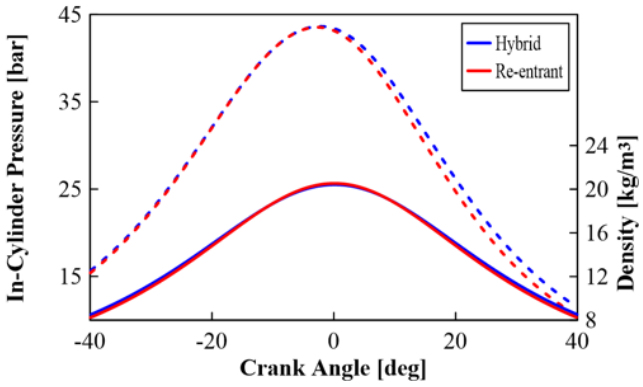

Figure 2–10: In-cylinder pressure (dashed line) and density (solid line) for the two investigated piston bowls.

Table 2–8: Engine intake operating conditions.

Piston type	**Intake Press.**	**Intake Temp.**	$\dot{m}_{air}$
re-entrant	1.9 bar	90 °C	7.26 g/s
hybrid	2.1 bar	120 °C	7.55 g/s

The injection strategy was the same for both the piston designs, leading to an engine load of 4.5 bar IMEP for both cases. The engine was operated under skip firing mode, injecting fuel one out of 20 cycles. In this way the fouling, the thermal stresses and the piston ring deterioration were minimized. As far as the fuel injection is concerned, the fuel was supplied by a conventional fuel pump into

a common rail injection system. The injector was controlled by a DRIVVEN® control unit, allowing complex injection strategies. In this experimental campaign, the injection schedule featured four injection pulses (two pilot, one main and post-injection) with an injection pressure of 670 bar.

2.4.1 Combustion Image velocimetry (CIV)

The CIV technique was used to characterize the flame movement thanks to the in-cylinder thermal radiation images. The algorithm is similar to the one used for the Particle Image Velocimetry (PIV) where the in-cylinder flow is seeded with particles that are illuminated by an external light source (laser sheet). Contrarily, for CIV no external light source is required since the incandescent soot acts as the tracking source. This approach can be adopted even for realistic bowl geometries under reactive conditions where the use of the conventional PIV is not allowed. More in detail, the use of realistic bowl geometries provides optical distortions on the images and its intensity depends on the distance between the radiation source and the bowl surface. The realistic bowl geometries used in this study provide mainly an image distortion in the radial direction and this affects mainly the velocity magnitude rather than the velocity direction. Therefore, the distortion effect should be considered in this analysis. Nevertheless, since the bowl geometries have similar features, the distortion is expected to be comparable, thus guaranteeing a robust comparison between the investigated designs.

The soot thermal radiation was registered by a high-speed CMOS camera (Photron SA-5) coupled with a Carl Zeiss Makro-Planar camera lens (100mm, f/2). The camera was set to record 25.000 frames per second with an exposure time of 6.6 μs. The image size was 512 x 512 pixels with 8.1 pixel/mm resolution, which was used to calibrate the CIV velocity flow fields. The pixel/mm ratio was obtained using as reference the outer diameter of the piston. The impossibility to address the distortion within the piston bowl motivated the selection of a reference not affected by optical deformation.

To obtain the instantaneous 2D velocity distributions a cross-correlation algorithm was used. The camera lens was set to the maximum aperture to guarantee enough sensitivity for the imaging system. Therefore, the depth-of-field is limited and when the piston is far from the TDC some blurring effect could be introduced. Nevertheless, since the CIV uses the soot clouds as tracer, this effect has no significant impact. The processing of the images was performed by means of PIVlab software [72]. It was applied to ensemble average images of 6 combustion cycles to minimize the impact of cycle-to-cycle variability and to obtain results directly comparable with the RANS simulation data. The time interval between images was set to 40 μs. The main processing parameters are listed in **Table 2–9**.

Table 2–9: CIV main processing parameters.

Interrogation window	1st pass: 32px size with 16px steps 2nd pass: 16px size with 8px steps
Data validation	- Standard deviation filter: $Thresh = \bar{u} \pm 8 \cdot \sigma_u$ - Local normalized median filter, with a threshold of 3 and ε = 0.1
Missing data interpolation	3x3 neighborhood interpolation

To directly compare the CIV resolved velocity flow field with the numerical results, the CFD velocity flow field was averaged along the cylinder axis, following the methodology described in [73]. More in detail, the average was

carried out considering the volume from a specific distance from the cylinder head and the bowl surface, thus avoiding during the injection event the spray core effect on the flow field. In addition, to further improve the comparison with CIV results, only the cylinder volume with a soot mass fraction higher than a user-defined value was considered. With this method, only a partial distribution of the velocity filed was computed, limiting the comparison to the region where higher soot content is localized.

2.4.2 OH* chemiluminescence

The radiation emitted by the excited-state of OH* was used to identify the near-stoichiometric high-temperature reaction region. To this aim, an intensified ICCD camera (Andor Solis iStar DH334T-18H-83) and a Bernhard-Halle UV lens (100 mm, f/2) were used. This platform led to 1024 x 1024 pixels images with 8.75 pixel/mm resolution. A bandpass filter was used in front of the camera to eliminate the radiation emitted by other sources. The filter had a transmission spectrum centered at 310 nm with 20 nm full width half maximum. The radiation was registered at 6 different crank angle degrees during the combustion process with an acquisition rate equal to 1 frame per cycle. The optical setup for the CIV and OH* analysis can be highlighted in **Figure 2–11**.

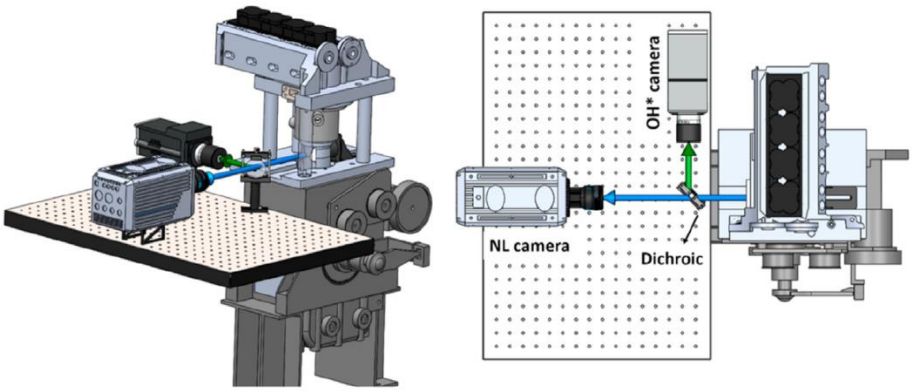

Figure 2–11: Optical setup for CIV and OH* analysis. Left: isometric view; right: top view.

The evolution of OH radicals was also analyzed thought CFD simulations and compared with the experimental OH* chemiluminescence images. With this aim, the numerical OH mass fraction (yOH) planar distribution over the whole computational domain was evaluated. Firstly, the yOH was traced and then each cell-value was averaged over the cylinder axis by means of **Eq. 2–1**:

$$yOH_{i,j}=\frac{1}{N}\sum_{k=1}^{N} yOH_{i,j,k} \qquad \text{Eq. 2–1}$$

where i, j, k represent the location of each cell in terms of x, y, z and N represents the total number of cell along the cylinder axis (z-axis) with not null $yOH_{i,j,k}$.

2.4.3 Optical soot density (KL)

Then 2-color pyrometry technique (2C) was used to evaluate the optical soot density (KL). It is based on the use of thermal radiation emitted by soot cloud at two different wavelengths. The spectrum of the thermal radiation emitted by a black body is described by the Planck's law of **Eq. 2–2**:

$$I_{b,\lambda} = \frac{C_1}{\lambda^5\left[e^{\left(\frac{C_2}{\lambda \cdot T}\right)}-1\right]} \qquad \text{Eq. 2–2}$$

where $I_{b,\lambda}$ is the monochromatic intensity of radiation of a black body, C_1 = $1.1910439\cdot10^{-16}$ $W\cdot m^2/sr$ and C_2 = $1.4388\cdot10^{-2}$ $m\cdot k$ are the first and second Planck's constants, λ is the wavelength and T is the temperature of the emitting source. However, the real source has a lower intensity of radiation (I_λ) than a black body at the same temperature. To account for this, **Eq. 2–2** is modified, introducing the emissivity (ε) as shown in **Eq. 2–3**:

$$I_\lambda = \varepsilon \cdot I_{b,\lambda} \qquad \text{Eq. 2–3}$$

For the soot particles, the emissivity can be expressed by the Hottel and Broughton empirical correlation [74] that is represented by **Eq. 2–4**:

$$\varepsilon_{soot}(KL,\lambda) = 1 - e^{-(KL/\lambda^{\alpha})} \qquad \text{Eq. 2–4}$$

where λ must be expressed in μm and α = 1.39 for most fuels within the visible range [75]. The KL is the optical soot density and denotes all the soot along the optical path. This parameter is directly linked to the soot volume fraction. The previous set of equations can be applied to the soot radiation at two different wavelengths to extract the soot temperature and the KL. To this aim, the apparent temperature ($T_{a,\lambda}$) was introduced as the temperature of a blackbody that emits the same radiation intensity of a non-blackbody at a different temperature and at a given wavelength [76]. Therefore, the measured intensity of radiation at each wavelength ($I_{\lambda,meas}$) can be evaluated as the radiation which is emitted by a blackbody at the corresponding $T_{a,\lambda}$, following the **Eq. 2–5**:

$$I_{\lambda,meas} = \frac{C_1}{\lambda^5\left(e^{\frac{C_2}{\lambda T_{a,\lambda}}} - 1\right)} \qquad \text{Eq. 2–5}$$

By substituting **Eq. 2–2**, **Eq. 2–4**, **Eq. 2–5** into **Eq. 2–3**, the KL factor can be computed by the following **Eq. 2–6**:

$$KL = -\ln\left\{1 - exp\left[-\frac{C_2}{\lambda}\left(\frac{1}{T_{a,\lambda}} - \frac{1}{T}\right)\right]\right\}^{\lambda^{\alpha}} \qquad \text{Eq. 2–6}$$

The KL is independent of the wavelength, therefore two equations with the same forms as **Eq. 2–6** can be written to evaluate the temperature of the soot surface, as highlighted in **Eq. 2–7**:

$$\left\{1 - exp\left[-\frac{C_2}{\lambda_1}\left(\frac{1}{T_{a,\lambda_1}} - \frac{1}{T}\right)\right]\right\}^{{\lambda_1}^{\alpha}} = \left\{1 - exp\left[-\frac{C_2}{\lambda_2}\left(\frac{1}{T_{a,\lambda_2}} - \frac{1}{T}\right)\right]\right\}^{{\lambda_2}^{\alpha}} \qquad \text{Eq. 2–7}$$

Once determined the temperature T, the KL was computed from **Eq. 2–6**.

The radiation emitted by the soot was detected by two identical system as highlighted in **Figure 2–12**. The radiation comes from the piston bottom which is the main optical access, and it is reflected by a 45 degrees mirror toward a beam splitter. The mirror splits the incident radiation by reflecting half of it towards the detection system 1 and transmitting the other half towards the system 2. Both system 1 and system 2 were composed by a high-speed CMOS camera (Photron SA-5), equipped 100 mm focal length lens with f/2 aperture (Carl Zeiss Makro-Planar). A 50 nm narrowband bandpass filter was placed in front of each lens to register only the radiation at a specific wavelength. Their transmission band was centered at 550 and 660 nm respectively, with +/- 10 nm full width half maximum. The cameras were triggered through the start of energizing, and both were synchronized to ensure the frame-to-frame correspondence. The acquisition rate was set at 25.000 fps for both the systems. However, a different exposure time was set for each system to maximize the used dynamic range: 10.05 μs was utilized for the 550 nm radiation while 6.65 μs was set to register 660 nm radiation. The image size was 512 x 512 pixels, with 8.1 pixel/mm resolution. A tungsten-ribbon calibration lamp (Osram Wi17G) was used to transform the digital signal from the cameras into intensity of radiation. To this aim, following the procedure described in [77], the calibration lamp was located on top of the piston (flat area) and the radiation was registered using the same optical set-up as the experiments.

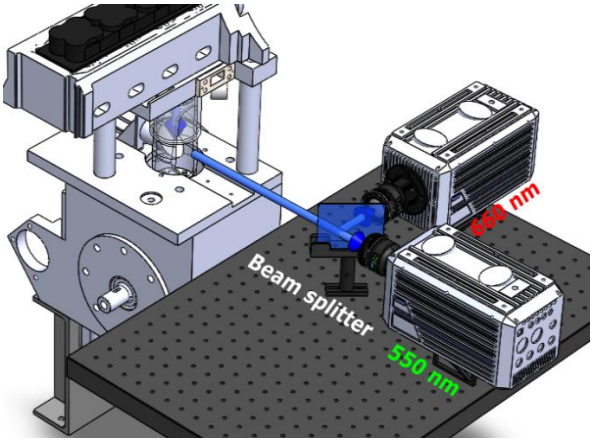

Figure 2–12: Optical setup for soot KL analysis.

To compare the optical 2D soot density KL with the numerical 3D soot distribution, a line-of-sight (LOS) integration methodology was used. With this

approach an interpretation of the third dimension along the optical depth was assessed, providing a 2D distribution even for the numerical results. Two different approaches were investigated. The first is based on the product of soot volume fraction (f_v) and the LOS path length (L), representing a quantitative measure of soot along the optical depth [78]. Thanks to the detailed kinetic mechanism and the PM soot model, the f_v distribution within the computational domain was assessed. Then, to obtain the f_vL planar distribution, the integration over the LOS was performed as highlighted in the **Eq. 2–8**:

$$(f_vL)_{i,j} = \sum_{k=1}^{N} (f_vL)_{i,j,k} \qquad \text{Eq. 2–8}$$

where i, j, k represent the location of each cell in terms of x, y, z, L is the cell vertical length and N represents the total number of cell along the LOS computational columns, as shown in **Figure 2–13**.

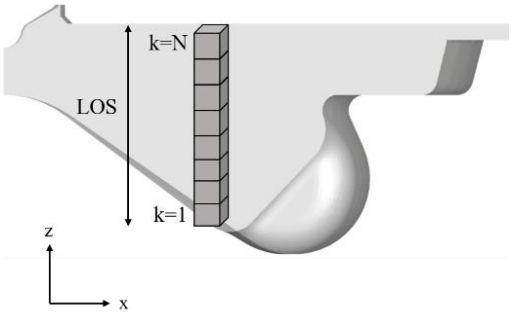

Figure 2–13: LOS computational column.

Although this quantity can be easily computed, the experimental f_vL is not directly measurable. Therefore, a further methodology based on LOS integration was employed to obtain an equivalent 2-color pyrometry method in the 3D-CFD environment, as shown in [79]. The 2-color pyrometry algorithm was adopted to extract the numerical soot-KL, by computing the bi-dimensional distribution of the monochromatic intensity of radiation (I_λ) for the same wavelengths (λ) adopted in the experimental analysis (550 and 660 nm). To this aim, the KL was computed for each cell of the computational volume through the **Eq. 2–9**, as suggested by the Kamimoto et al in [76]:

$$KL = 6\pi\, E(m) f_v L \qquad \text{Eq. 2–9}$$

where f_v and L are the soot volume fraction and the vertical length of each computational cell, respectively. E(m) is linked to the complex refractive index of soot particles (m) that is a function of the wavelength, but it can be considered constant in the visible spectra range [76]. In this work, E(m) = 0.245 was adopted, as also reported in [79] for a similar investigation on optical engine. By using the temperature and the KL of each computational cell, the I_λ was computed by means of **Eq. 2–2**, **Eq. 2–3** and **Eq. 2–4**. Then, for each column of cells as shown in **Figure 2–14**, the line-of-sight integration of I_λ was carried out, providing an interpretation of the vertical direction (cylinder axis) and providing a bi-dimensional distribution of I_λ. In this work, a homogeneous composition for the computational cell was assumed and only the soot was involved in the light transfer process, thus considering the surrounding gas fully transparent [79]. Moreover, assuming that the detector was at a sufficient distance from the emitting source, only the radiation emitted along the vertical direction can be considered [79]. In the radiation transfer process, only a part of the soot radiation passes through the domain. The fraction of the transmitted light was estimated by the soot transmissivity (τ_λ), following the Kirchhoff's law [80] and neglecting scattering, as the complement of the soot emissivity:

$$\tau_\lambda = 1 - \varepsilon_\lambda \qquad \text{Eq. 2–10}$$

The scheme and equations for the line-of-sight integration method are shown in **Figure 2–14**. Considering the light reflection induced by the cylinder head, a set of equations was defined for the two vertical direction: the upward direction from the piston to the head and the downward direction from the head to the piston. The intensity of radiation emitted by each cell-k along the upward ($I_{\lambda,k}\uparrow$) and downward ($I_{\lambda,k}\downarrow$) directions can be expressed by the sum of two contributions: the radiation emitted by the cell itself ($I_{\lambda,k}$) and the radiation transmitted from the adjacent cell, that is affected by the soot transmissivity. Considering the cell adjacent to the cylinder head, the radiation emitted in the upward direction is reflected by the wall with a certain reflectivity (ρ_{wall}). By integrating the equations first upward and then downward, the $I_{\lambda,out}$ for the two wavelengths was evaluated at the piston surface. Finally, following the 2-color pyrometry technique previously presented, the KL factor was computed also for the 3D-CFD environment.

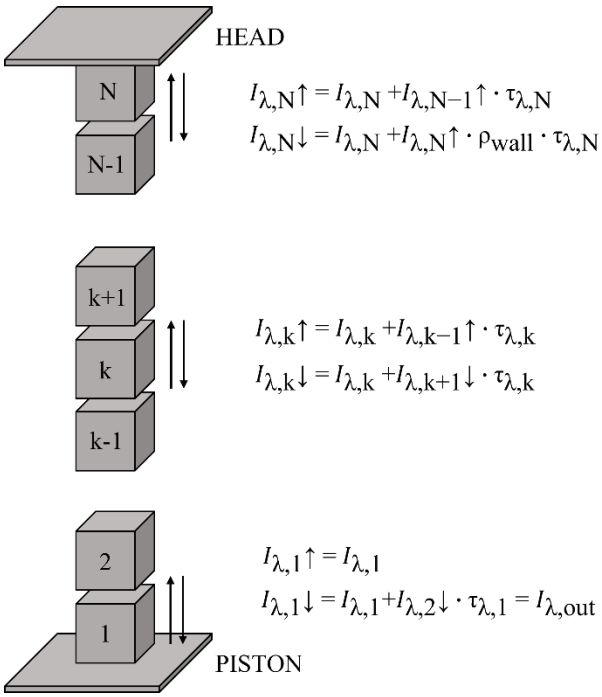

Figure 2–14: Scheme and equations for LOS computation.

Chapter 3

Stepped-lip and radial-bumps bowl designs

Part of the work described in this Chapter was also previously published in the following publications:

- Millo, F., Piano, A., Roggio, S., Bianco, A. et al., "Numerical Investigation on Mixture Formation and Combustion Process of Innovative Piston Bowl Geometries in a Swirl-Supported Light-Duty Diesel Engine," SAE Int. J. Engines 14(2):247-262, 2021, https://doi.org/10.4271/03-14-02-0015.
- Millo, F., Piano, A., Roggio, S., Pesce, F.C., Vassallo, A., Bianco, A., "Numerical Assessment on the Influence of Engine Calibration Parameters on Innovative Piston Bowls Designed for Light-Duty Diesel Engines," Energies, 15(10):3799, 2022, https://doi.org/10.3390/en15103799.

3.1 Introduction

Once assessed the predictive capabilities of the numerical model for the conventional re-entrant bowl, two innovative designs were numerically investigated: the stepped-lip and the radial-bumps bowls. The stepped-lip bowl

was designed following the geometrical features highlighted in [29]. Then, considering as basis the re-entrant bowl, a radial-bumps geometry was designed, adding a number of radial bumps equal to the injector nozzle holes in the outer bowl rim, as also shown in [37]. Both the proposed designs feature the same bore, squish height and compression ratio (i.e. 16:1) adopted for the re-entrant bowl. **Figure 3–1** shows the piston bowl geometries numerically investigated.

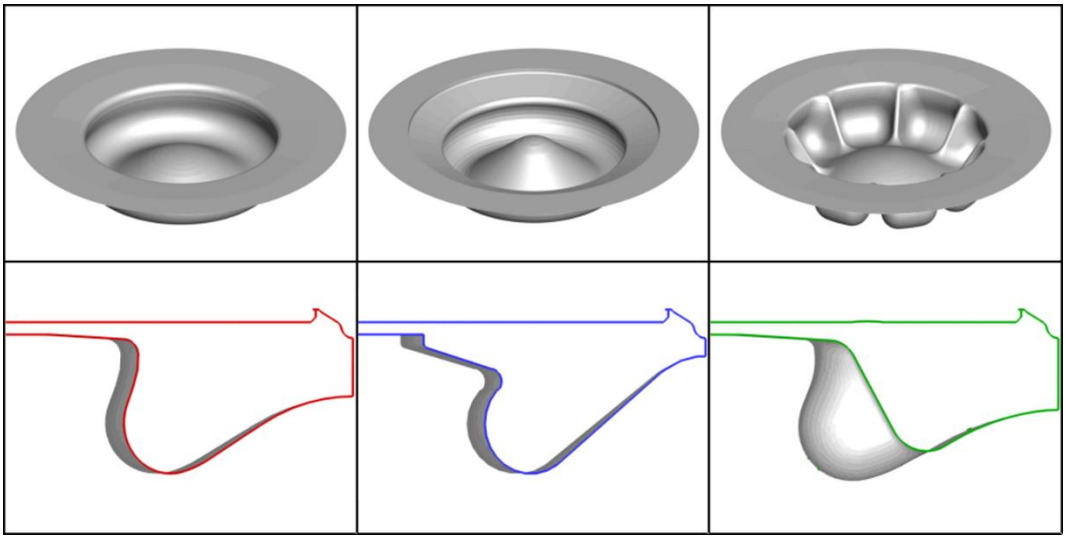

Figure 3–1: Piston bowl geometries under investigation. Left: re-entrant; middle: stepped-lip; right: radial-bumps.

In the first part of this chapter, the in-cylinder flow field and mixing process were investigated under non-reacting conditions for each combustion system. To this aim, the full cylinder geometry was investigated at rated power engine operating conditions (WP3). Then, a sector-mesh of the cylinder geometry was adopted for the combustion simulation under two different engine operating conditions: WP3 and the partial load WP1. Additionally, a sensitivity analysis over different engine calibration parameters was carried out, providing further guidelines about the needs of the proposed designs in terms of engine calibration. In this regard, at full load (WP3), the injection timing and the swirl ratio sensitivity were performed. Then, under the partial load WP1, different EGR rates at two rail pressure levels were assessed, showing the potential benefits in terms of efficiency and pollutant emissions.

3.2 3D-CFD analysis

3.2.1 Mixing-only analysis

The impact of the combustion system on the in-cylinder flow field and on the mixing process was assessed through numerical non-reacting simulation of the full cylinder geometry. The full load engine operating condition (WP3) was considered for the scope, since the more intense in-cylinder velocity magnitude can enhance the formation of turbulent structures. The results in terms of swirl ratio (SR) and turbulent kinetic energy (TKE) for each investigated combustion system are shown in **Figure 3–2**.

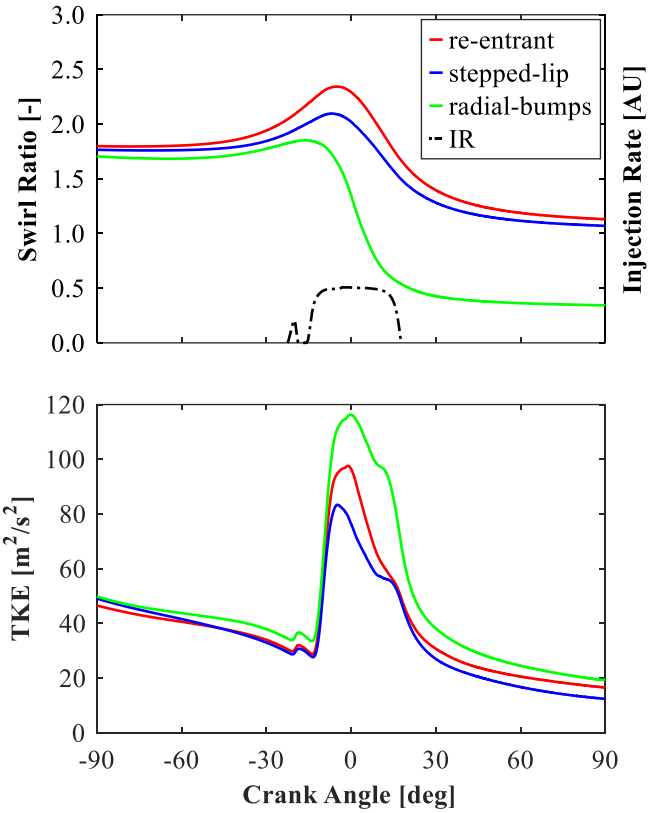

Figure 3–2: Swirl ratio (top) and TKE (bottom) evolutions for the analyzed combustion systems. WP3: 4000 RPM x 18.5 bar BMEP.

Regarding the SR evolution of **Figure 3–2** – top, reduced differences can be observed during the compression stroke until the Start of Injection (SOI) of the

pilot event. The radial-bumps bowl shows the lowest SR due to the radial bumps that break the swirling flow. Going toward the Top Dead Center (TDC), the stepped-lip bowl shows a lower swirl amplification. This is due to the lower squish area and the divergent tapered lip that reduces the squish flow intensity, as also reported in [81]. At TDC, the radial-bumps bowl shows the lowest swirl amplification although it has the same squish area of the re-entrant bowl. In this case, the swirl reduction is mainly due to the radial bumps that break the swirling flow. Also, the lower swirl leads to higher spray momentum transfer, causing a swirl collapse during the expansion stroke. Moreover, the interaction between the swirling flow and the radial bumps provides the highest TKE during the compression stroke and the main injection event, as highlighted in **Figure 3–2** – bottom. Contrarily, the stepped-lip bowl shows lower TKE than the re-entrant bowl, since the reduced squish area (lower squish flow) results in lower turbulent enhancement on the bowl lip [15]. In addition, for a conventional re-entrant bowl, the flow separation at the bowl lip [82] and the reverse squish flow [83] can further increase the turbulent generation.

The velocity distribution and the equivalence ratio distribution were analysed to understand the impact of different piston design on the mixing process. To this aim, three different planes were selected to show the results, as depicted in **Figure 3–3**. The plane A is a vertical plane centred along a single spray axis and it is placed between the intake and the exhaust valves to avoid the valve pockets and the glow plug interactions. The plane B and plane C are defined cutting two adjacent sprays located in the exhaust side, in the horizontal and in the spray axes directions, respectively.

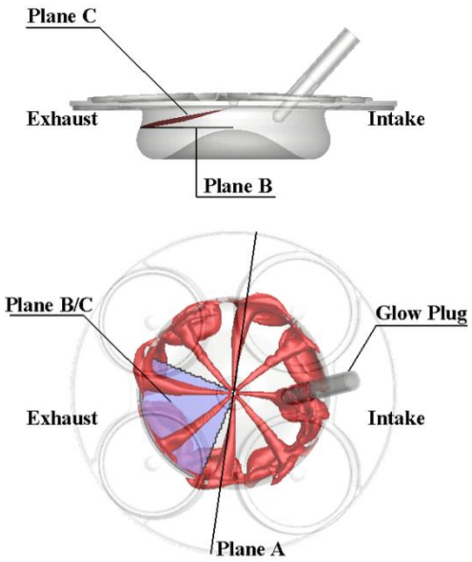

Figure 3–3: Planes selected to represent the numerical results and stoichiometric iso-surface at TDC.

The in-cylinder flow evolution was investigated in the plane A and plane B, considering the time before the injection event (**Figure 3–4**) and after the TDC, during the injection event (**Figure 3–5**). In particular, the analysis shows the velocity vectors tangential component contained in the selected cutting planes (named hereafter 'projected velocity'), with uniform size and coloured according to the projected velocity magnitude.

Figure 3–4 – a highlights the squish flow before the start of the injection event, at -23 CAD aTDC. The piston bowl geometry strongly affects the intensity of the squish flow. The re-entrant and the radial-bumps bowls highlight a more intense squish flow with respect to the stepped-lip bowl due to the higher squish area. Regarding **Figure 3–4** – b, the swirling flow for the re-entrant and the stepped-lip bowls is still retained. Contrarily, the radial-bumps design attenuates the swirling flow due to the radial bump geometry. In particular, a flow separation is shown in the bump tip which enhances the turbulent intensity and a low velocity region (stagnation zone) can be observed for the gas within two consecutive bumps.

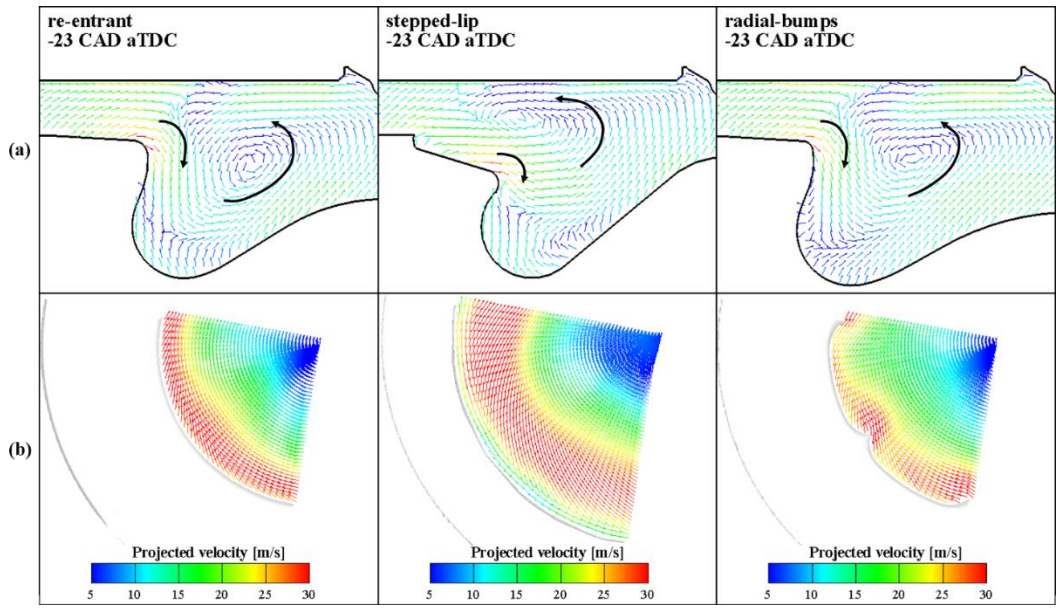

Figure 3–4: Velocity vectors at -23 CAD aTDC colored according to the magnitude of the projected velocity on the selected plane A (a) and plane B (b). Left: re-entrant; middle: stepped-lip; right: radial-bumps. WP3: 4000 RPM x 18.5 bar BMEP.

During the injection event at +5 CAD aTDC, the influence of the piston design on the flow structures becomes more evident, as highlighted in **Figure 3–5**. As shown for the plane A of **Figure 3–5** – a, the re-entrant bowl shows a toroidal vortex due to the spray-wall impingement and the piston motion, with a negligible fraction of the injected fuel that goes toward the squish area. Contrarily, the stepped-lip bowl leads to the fuel splitting at the step, resulting in two counter rotating toroidal vortices, as shown by the two black arrows. The radial-bumps bowl, although it features the same bowl curvature of the re-entrant bowl, leads to a more intense toroidal vortex due to the reduced interaction between the fuel jet and the swirling flow caused by the stagnation zone previously described. Regarding the plane B of **Figure 3–5** – b, high differences can be observed over the piston designs. The flow structure is still swirl supported for both the re-entrant and the stepped-lip bowls. On the contrary, the radial-bumps bowl strongly affects the swirling flow due to the bumps that break the swirl vortex. Moreover, the swirl flow moves the spray-wall impingement toward a higher curvature region close to the radial bumps. Therefore, the jet is redirected toward the consecutive sector, driving to the formation of an intense turbulent recirculating zone, as shown by the black arrow.

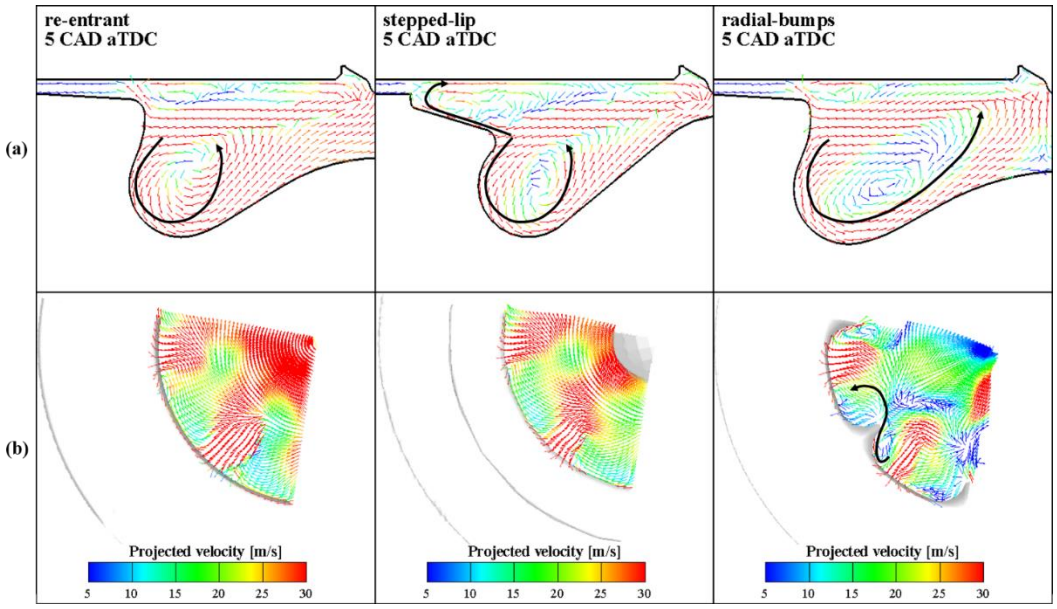

Figure 3–5: Velocity vectors at +5 CAD aTDC colored according to the magnitude of the projected velocity on the selected plane A (a) and plane B (b). Left: re-entrant; middle: stepped-lip; right: radial-bumps. WP3: 4000 RPM x 18.5 bar BMEP.

The mixture formation process was investigated during the injection event on the cutting plane A and plane C of **Figure 3–3**. The equivalence ratio distribution during the main injection event, at +5 CAD aTDC, is shown on **Figure 3–6**. Regarding the plane A of **Figure 3–6** – a, the re-entrant bowl shows the fuel jet that is mainly directed within the bowl, while only a small portion of the fuel jet propagates toward the squish area due to the reverse squish flow. For the stepped-lip bowl the fuel jet is more evenly distributed above the step and within the bowl, leading to higher air utilization in the squish area and thus enhancing the air/fuel mixing rate, as also shown in [84]. The radial-bumps bowl provides faster fuel propagation toward the bowl center due to the more intense toroidal vortex, previously highlighted. Considering the plane C (spray axes plane) of **Figure 3–6** – b, different jet surface fluctuations can be observed due to the interaction between the exhaust valves and the fuel sprays, for all the piston geometries under investigation. Both the re-entrant and the stepped-lip bowls show a tangential fuel jet propagation on the piston surface enhanced by the swirl motion. However, for the stepped-lip bowl a reduced jet-to-jet interaction is highlighted due to the fuel split that leads to higher upward jet velocity above the step. Regarding the radial-

bumps bowl, the jet-to-jet interaction is strongly reduced and the fuel jet is redirected by the bump toward the adjacent sector, where available oxygen is placed. Therefore, this fuel jet recirculation promotes faster air/fuel mixing onto the jet front.

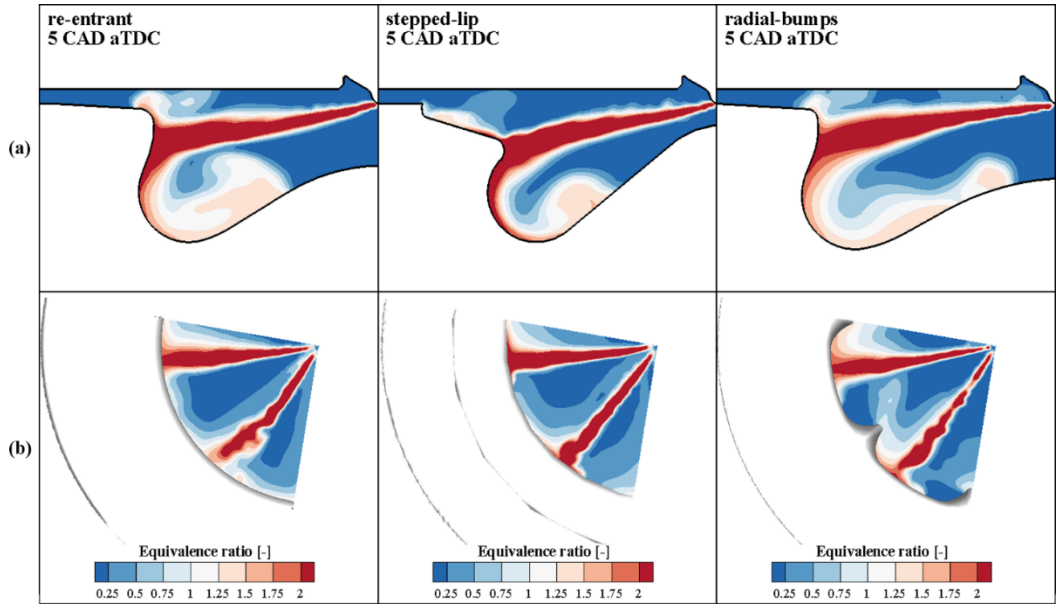

Figure 3–6: Equivalence Ratio contour plot at +5 CAD aTDC on the selected plane A (a) and plane C (b). Left: re-entrant; middle: stepped-lip; right: radial-bumps. WP3: 4000 RPM x 18.5 bar BMEP.

The equivalence ratio distribution was also assessed during the late phase of the injection event at +15 CAD aTDC, as shown in **Figure 3–7**. For the stepped-lip bowl, the spray-wall impingement occurs above the step surface and the fuel jet mainly propagates toward the cylinder head, leading to a poor air utilization within the bowl, as highlighted in **Figure 3–7** – a. Considering the spray axes plane of **Figure 3–7** – b, the jet-to-jet interaction for the radial-bumps bowl is still the main difference with respect to the re-entrant bowl. In particular, the recirculating flow on the bumps continues its evolution and a more evident jet-to-jet interaction near the bump tip appears, thus creating a more pronounced radial mixing zone.

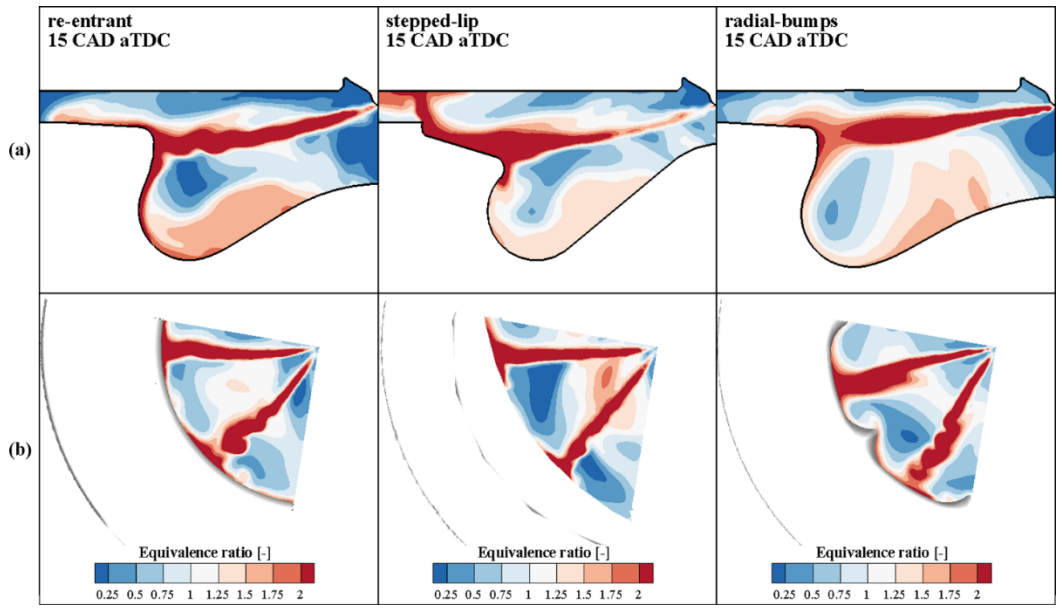

Figure 3–7: Equivalence Ratio contour plot at +15 CAD aTDC on the selected plane A (a) and plane C (b). Left: re-entrant; middle: stepped-lip; right: radial-bumps. WP3: 4000 RPM x 18.5 bar BMEP.

To further understand the piston bowl effect on the mixing process, a global index of the air/fuel mixing was defined on the basis of the equivalence ratio distribution within the combustion chamber. To this aim, at each crank angle, the total cylinder mass was binned by equivalence ratio into twenty intervals, starting from 0-0.1 bin which corresponds to the pure ambient gas and ending to 1.9-2 bin which is representative of the injected fuel mass. The resulting cylinder mass for each bin was divided by the total cylinder mass providing the cylinder mass fraction for each bin. Then, this quantity was plotted on a bar chart and collecting all the bar charts for each crank angle, a contour plot was defined, as shown in **Figure 3–8**. The equivalence ratio bins in the range 0.1-1 provide an index of the air/fuel mixing rate: high cylinder mass fraction within this range represents a higher air utilization. Before TDC, no significant variations can be observed over the investigated piston bowl designs, since the air/fuel mixing mainly occurs due to the fuel jet free propagation. From 0 to +10 CAD aTDC, both the stepped-lip and the radial-bumps designs highlight a higher cylinder mass fraction within the 0.1-1 equivalence ratio bin, thus leading to a higher mixing rate. At this stage, the stepped-lip bowl improves the air utilization due to the fuel splitting at the step, while the radial-bumps bowl improves the mixing rate due to the fuel jet

recirculation across the bumps. From +5 CAD aTDC, during the late phase of the main injection event, the stepped-lip bowl provides a reduced air/fuel mixing rate with respect to the radial-bumps bowl. Indeed, for the stepped-lip bowl the cylinder mass fraction is distributed in a smaller equivalence ratio range with high cylinder mass fraction in the 0.2-0.4 bin. This reduction in the air/fuel mixing rate is mainly due to the not favourable fuel split at the step, as shown in **Figure 3–7**. Conversely, the radial-bumps bowl highlights a continuous increment of the mixing rate, as denoted by the spreading of the cylinder mass fraction toward the stoichiometric range. This result appears even more evident going toward the end of injection, where the radial-bumps bowl highlights the peak of the cylinder mass fraction in the stoichiometric range.

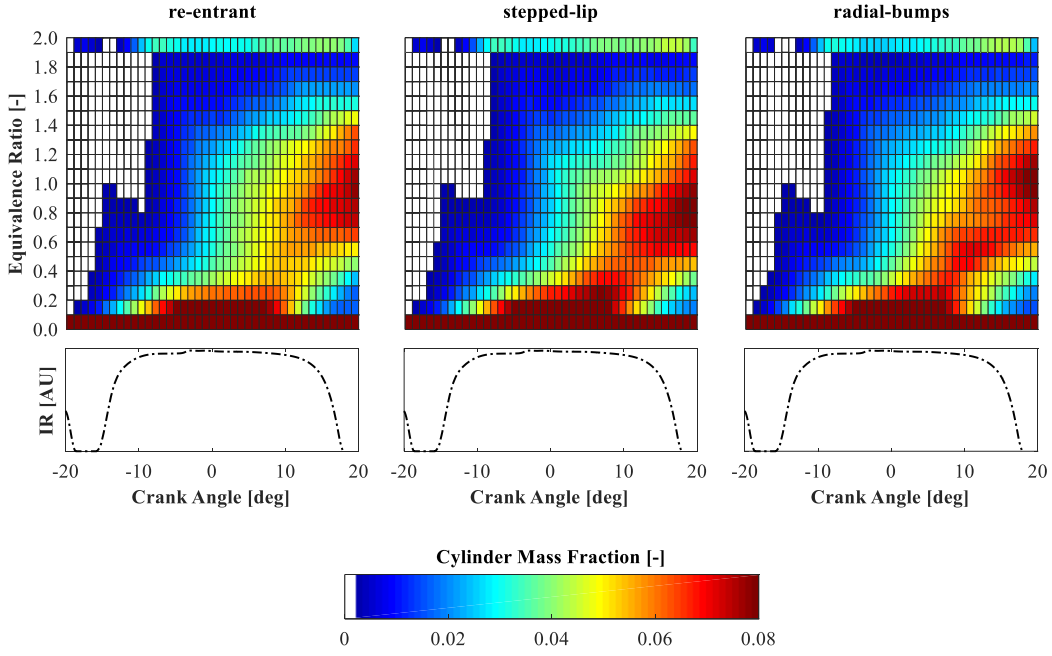

Figure 3–8: Cylinder mass fraction evolution for each equivalence ratio bin (top) and injection rate profile (bottom). Left: re-entrant; middle: stepped-lip; right: radial-bumps. WP3: 4000 RPM x 18.5 bar BMEP.

3.2.2 Combustion analysis

Once assessed the mixing process for each combustion system under investigation, the combustion analysis was performed, following the simulation methodology previously reported in the Simulation Setup section. **Figure 3–9**

shows the results in terms of heat release rate (HRR) and cumulative heat release (HR) under the full load engine operating conditions (WP3).

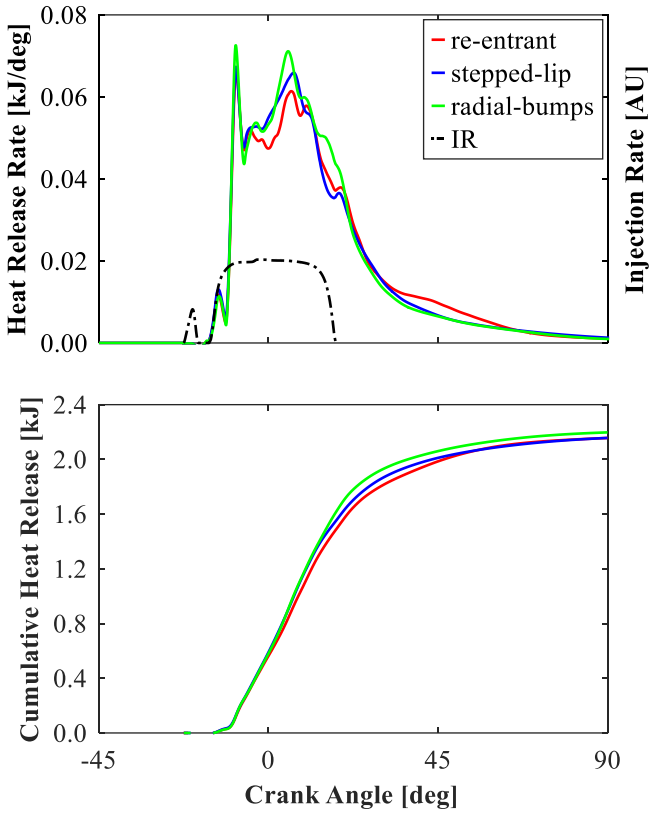

Figure 3–9: Top: Heat Release Rate and injection rate profile; bottom: Cumulative Heat Release. WP3: 4000 RPM x 18.5 bar BMEP.

Considering the HRR of **Figure 3–9** – top, the premixed combustion phase is not sensibly affected by the piston bowl design. Moving toward the TDC, some differences can be highlighted: the re-entrant bowl shows a reduced HRR with respect to the other piston bowls. At this stage, the combustion evolution is dramatically affected by the flame-to-wall and the flame-to-flame interactions which reduce the mixing rate onto the flame front, as also reported in [38]. As reported in **Figure 3–6**, under non-reacting conditions the re-entrant bowl highlights the strongest jet-to-jet interaction, and this effect becomes even more intense during the combustion due to the higher turbulence level. From 0 to +5 CAD aTDC, the combustion results confirm what was expected by the mixing

analysis. Indeed, both the stepped-lip and the radial-bumps bowl show a higher HRR with respect to the re-entrant bowl due to the faster air/fuel mixing rate. From +5 CAD aTDC to EOI, the stepped-lip bowl leads to lower HHR and HR than with the radial-bumps bowl. Indeed, as already observed in non-reacting conditions, the stepped-lip bowl provides a lower mixing rate due to unfavourable fuel split on the step. This result is also confirmed in [34], where the unbalanced fuel split on the step showed a detrimental effect on the combustion efficiency, especially at high load and high speed conditions. Conversely, the radial-bumps design shows the highest HRR in mixing-controlled combustion phase due to the more intense air/fuel mixing rate, as confirmed by **Figure 3–8**. After the EOI of main event, the re-entrant bowl leads to a comparable HR than with the stepped-lip bowl, reaching similar 10-90 combustion duration, due to the higher swirl ratio that efficiently mixes the residual fuel. In conclusion, keeping constant the injected fuel, the higher HRR for the radial-bumps bowl provides a 3.3% brake power increment with respect to the re-entrant bowl. Instead, for the stepped-lip bowl, a negligible delta brake power (0.3%) is obtained with respect to the re-entrant bowl.

At partial load (WP1), an investigation on soot evolution was carried out to understand the effect of different combustion systems on the soot formation and oxidation processes. The results of the detailed PM model in terms of soot mass and net soot formation rate are highlighted in **Figure 3–10**. After the EOI of main event, the radial-bumps bowl leads to lower soot mass with respect to the re-entrant and the stepped-lip bowls. Indeed, minimizing the flame-to-flame interaction and enhancing the air/fuel mixing result in a strong reduction of the net soot formation rate, as highlighted in **Figure 3–10** – bottom. For the stepped-lip bowl, during the after-injection burn-out, the soot mass and its net formation rate are higher than with the re-entrant bowl. However, moving ahead in the combustion process, the burn-out of the residual rich zones has a fundamental impact on soot oxidation rate [36]. At this stage, the stepped-lip bowl highlights the higher soot oxidation rate, resulting in a comparable engine-out soot emission than with the radial-bumps bowl.

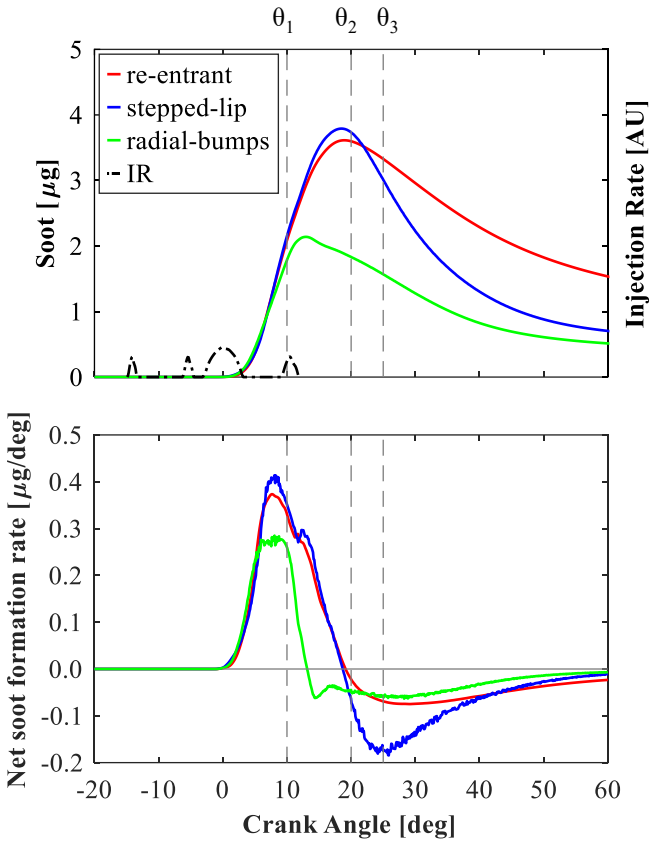

Figure 3–10: Soot PM model results for the nominal EGR rate. Top: In-cylinder Soot mass; bottom: Net formation rate of in-cylinder soot mass. WP1: 1500 RPM x 5.0 bar BMEP.

To further investigate the piston bowl impact on soot emission, the in-cylinder soot mass evolution was analysed. To this aim, the mass of the computational domain was divided depending on the soot mass density of each cell and considering as reference the maximum soot density obtained with the re-entrant bowl. The in-cylinder mass with a soot density in the range 20-40% of the maximum value (bin 1) was considered as representative of the low soot density class, while the in-cylinder mass with a soot density in the range 60-80% of the maximum value (bin 2) was selected to show the high soot density class. **Figure 3–11** shows the bin 1 (blue) and bin 2 (red) soot-density iso-surfaces at the three different crank angle degrees highlighted in **Figure 3–10**.

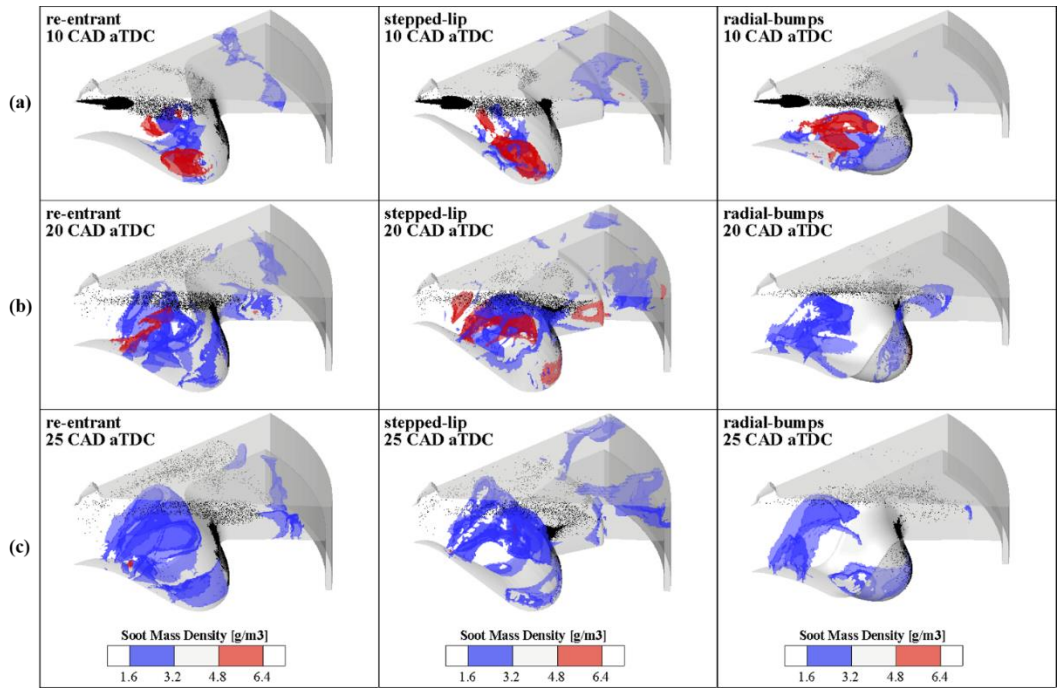

Figure 3–11: Bin 1 (blue) and bin 2 (red) soot density iso-surfaces. The liquid fuel is represented by the black parcels. Left: re-entrant; middle: stepped-lip; right: radial-bumps. WP1: 1500 RPM x 5.0 bar BMEP.

At θ_1 = +10 CAD aTDC

Figure 3–11 – a shows the soot density distribution after the EOI of main event. Both the re-entrant and the stepped-lip bowls provide an intense high soot density region in the sector periphery due to the flame-to-flame interaction. Contrarily, the radial-bumps bowl minimizes this effect and lower soot density can be observed in the sector periphery. In addition, the more intense tumbling vortex, as highlighted on **Figure 3–5**, moves the flame and therefore the bin 2 high soot density region toward the piston center, where the available oxygen will improve the soot oxidation.

At θ_2 = +20 CAD aTDC

Figure 3–11 – b shows the effect of the after-injection burn-out on soot evolution. The re-entrant bowl shows a partial oxidation of the high soot density zone, while in the stepped-lip bowl the flame is directed above the step where the after-injection combustion mainly occurs. Moreover, due to the higher bowl

curvature, the flame recirculation within the bowl interacts with the after-injection flame on the spray axis, thus leading to higher bin 2 soot formation. For the radial-bumps bowl, both the after-injection combustion and the faster flame motion toward the piston center leads to a significant soot oxidation process and the bin 2 region is fully oxidized.

At θ_3 = +25 CAD aTDC

As outlined in **Figure 3–11** – c, moving ahead in the cycle, all the combustion systems can oxidize the bin 2 high soot density region. More in detail, the stepped-lip bowl shows a significant improvement of the soot oxidation rate, as previously observed in **Figure 3–10**. Although the after-injection above the step leads to higher soot formation in the squish region, the fuel previously injected within the bowl finds more available oxygen which helps the soot oxidation, as also noted in [84]. Moreover, the higher bowl curvature enhances the upward velocity of the flame within the bowl, leading to a higher mixing rate with respect to the re-entrant bowl.

3.2.3 Trade-offs

At partial load WP1, the combustion systems sensitivity in terms of engine-out emissions and fuel consumption was performed over an EGR sweep. The EGR rate was modified by varying the gas species concentration, thus keeping constant the volumetric efficiency, and analyzing only the dilution and thermal effects. To keep constant the engine load, the main injection energizing time was varied. **Figure 3–12** shows the trade-offs over the EGR sweep: Brake Specific Soot (BSSoot) versus Brake Specific NOx (BSNOx) is on **Figure 3–12** – left, while Brake Specific Fuel Consumption (BSFC) versus BSNOx is on **Figure 3–12** – right. The trade-offs were normalized with respect to the baseline engine configuration (i.e., nominal EGR – re-entrant bowl). Both the stepped-lip and the radial-bumps bowls show an improved BSSoot-BSNOx trade-off with respect to the re-entrant bowl. At baseline BSNOx, a 40% and 50% BSSoot reduction is reached by the stepped-lip and radial-bumps bowls, respectively. Concerning the BSFC-BSNOx trade-off, no significant improvement can be assessed for the stepped-lip bowl. Contrarily, the radial-bumps bowl shows a strong reduction of BSFC (-5%) at baseline BSNOx, providing an unusual but desirable flatness in the trade-off over the EGR sweep. Therefore, the beneficial flow motion induced

by the radial bumps is not affected by the EGR rate, confirming that the main driver is the improved mixing process induced by the combination of radial bumps and swirl motion, as reported in [41].

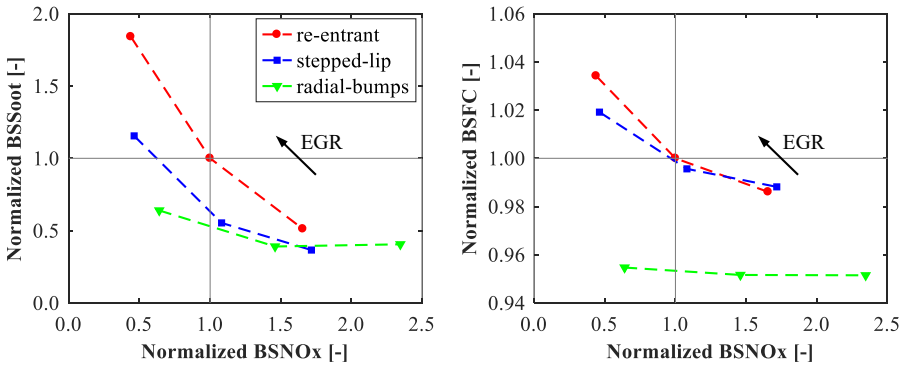

Figure 3–12: EGR sweep: normalized trade-offs with respect to baseline engine configuration. Left: BSSoot-BSNOx trade-off; right: BSFC-BSNOx trade-off. WP1: 1500 RPM x 5.0 bar BMEP.

3.3 Engine calibration parameters

3.3.1 Start of injection sensitivity

The injection timing has a fundamental role to maximize the potentials of a bowl design since the injection timing affects the spray targeting thus leading to different spray-wall interaction. Therefore, at rated power conditions (WP3), a sensitivity on the start of injection (SOI) was carried out, keeping the injected fuel mass constant. To this aim, three different SOI were assessed: the nominal SOI for the re-entrant bowl (baseline) and +5/+10 CAD with respect to the baseline SOI. The SOI sweep results were reported in terms of mass fraction burned data (CA 10, 50, 75, 90) in **Figure 3–13** – a.

As expected, the initial combustion phase is not affected by the bowl design variation, as highlighted by the CA10 data over the SOI sweep. Then, the innovative bowl geometries start to affect the combustion process in the mixing-controlled combustion phase, as shown by the CA50 which is slightly advanced for both the stepped-lip and the radial-bumps bowls. The differences become even more evident in terms of CA75, and both the innovative designs (stepped-lip and radial-bumps) provide advanced combustion with respect to the re-entrant bowl

for each investigated SOI. During the late phase of combustion, the piston designs provide a different behavior depending on SOI. The CA90 data for the re-entrant bowl are quite constant by changing the SOI. Contrarily, the stepped-lip bowl highlights a strong increment of CA90 by retarding the SOI, as also experimentally assessed in [25]. Indeed, in the late injection phase, the spray-wall impingement occurs above the step, providing lower air utilization within the bowl. For the radial-bumps bowl, the highest difference at the baseline SOI with respect to the re-entrant bowl can be observed. By retarding SOI, the deviation from the CA90 of the re-entrant bowl is reduced. Therefore, the radial protrusions in the outer bowl rim provide higher benefits when the optimal spray targeting is adopted.

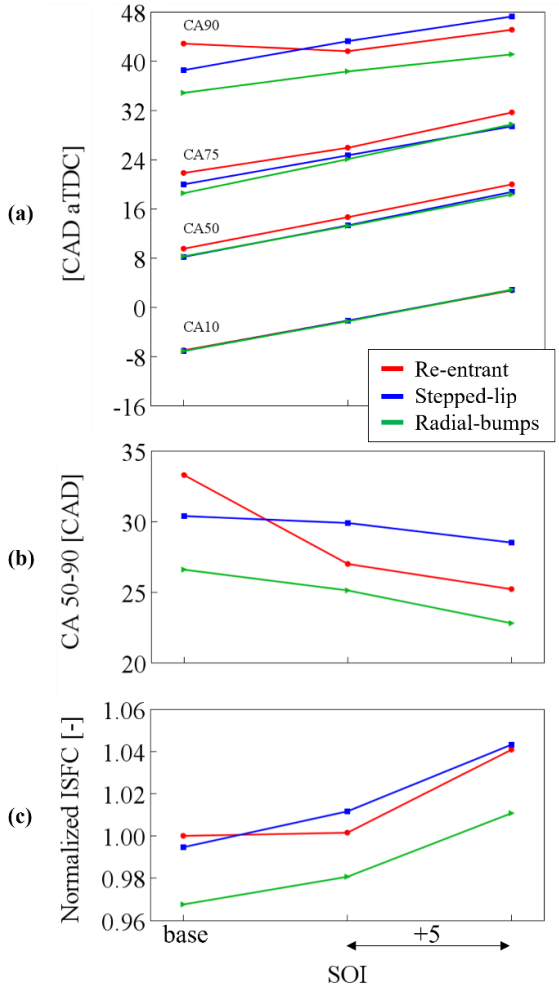

Figure 3–13: SOI sweep results. (a) Mass fraction burned data; (b) CA50-90; (c) ISFC normalized with respect to baseline engine configuration (bowl: re-entrant; SOI: base). WP3: 4000 RPM × 18.5 bar BMEP.

To further understand the injection timing sensitivity, the duration of the last phase of the mixing-controlled combustion, represented by CA50-90, was investigated as shown in **Figure 3–13** – b. The radial-bumps bowl provides lower CA50-90 than with the re-entrant bowl for each SOI under investigation. However, the higher deviation from the re-entrant bowl can be highlighted for the baseline SOI, suggesting once again that a proper spray targeting is required to maximize the radial bumps benefits. For the stepped-lip bowl, retarding SOI leads to higher combustion duration with respect to the other designs due to the unbalanced fuel split at the step. **Figure 3–13** – c shows the ISFC normalized with respect to the baseline engine configuration (i.e., baseline SOI – re-entrant bowl). The radial-bumps bowl with the baseline SOI shows the lowest ISFC, leading to -3% reduction with respect to the re-entrant bowl. This result is comparable with the outcome of an experimental activity for a similar bowl design in a heavy-duty diesel engine application [5]. In this work, up to +1% of thermal efficiency was obtained over different high-load engine operating conditions. For the stepped-lip bowl at the baseline SOI, a ISFC reduction of 1% was assessed. Nevertheless, by retarding SOI, the stepped-lip bowl provides a worsening of the ISFC with respect to the re-entrant bowl, confirming the crucial role of the fuel split for an efficient combustion.

3.3.2 Swirl ratio sensitivity

The swirl ratio effect on the piston bowl design has been previously reported under non-reacting conditions for the full-cylinder geometry. Then, to further understand the swirl impact on the combustion process, a swirl ratio at the IVC equal to zero was imposed, zeroing the velocity components perpendicular to the cylinder axis. The HRR and the cumulative HR for each swirl ratio under investigation (i.e., nominal and zero) are shown in **Figure 3–14**. For each piston design under investigation, the zeroed swirl ratio provides a reduced air/fuel mixing during the pilot injection event, reducing the over-leaning of the fuel jet and leading to more intense pilot combustion. Due to this effect, the premixed combustion intensity of the main injection is reduced. Among the piston bowls under investigation, the stepped-lip bowl is the less affected by the swirl ratio variation due to the more open geometry and the main flow structures are the toroidal vortices in the cylinder axis plane. Contrarily, the cumulative HR for the re-entrant and the radial-bumps bowls is strongly affected by the swirl ratio. More in detail, the HR with the re-entrant bowl start to be affected by the different swirl ratio after the EOI. At this stage, the zeroed swirl ratio reduces the air/fuel mixing

of the residual fuel on the late cycle, leading to slower combustion and thus reducing the cumulative HR. For the radial-bumps bowl, the HRR is significantly reduced during the injection event in the case of null swirl ratio. Therefore, also the radial-bumps bowl requires a higher swirl ratio to increase the air/fuel mixing rate.

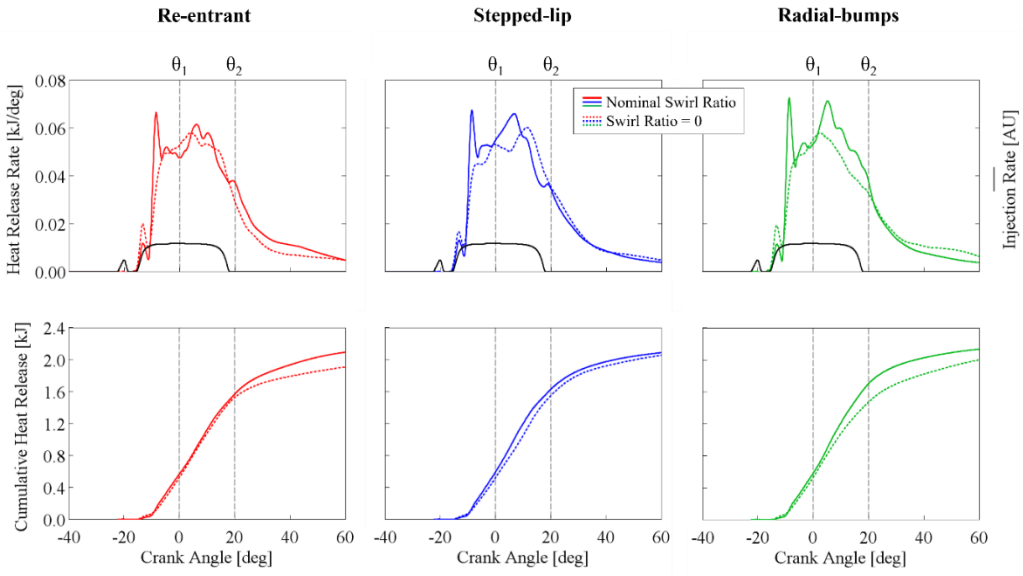

Figure 3–14: Swirl ratio results. Top: Heat release rate and injection rate; bottom: cumulative heat release. Left: re-entrant; middle: stepped-lip; right: radial-bumps. WP3: 4000 RPM × 18.5 bar BMEP.

To further understand the swirl ratio impact for each piston bowl under investigation, the equivalence ratio distribution was analyzed. To this aim, two cutting planes were selected to show the numerical results (the spray axis plane and the cylinder axis plane), while the 1500 K isoline was selected as representative of the flame front. **Figure 3–15** and **Figure 3–16** highlight the equivalence ratio distribution for the nominal swirl ratio and the zeroed swirl ratio, respectively.

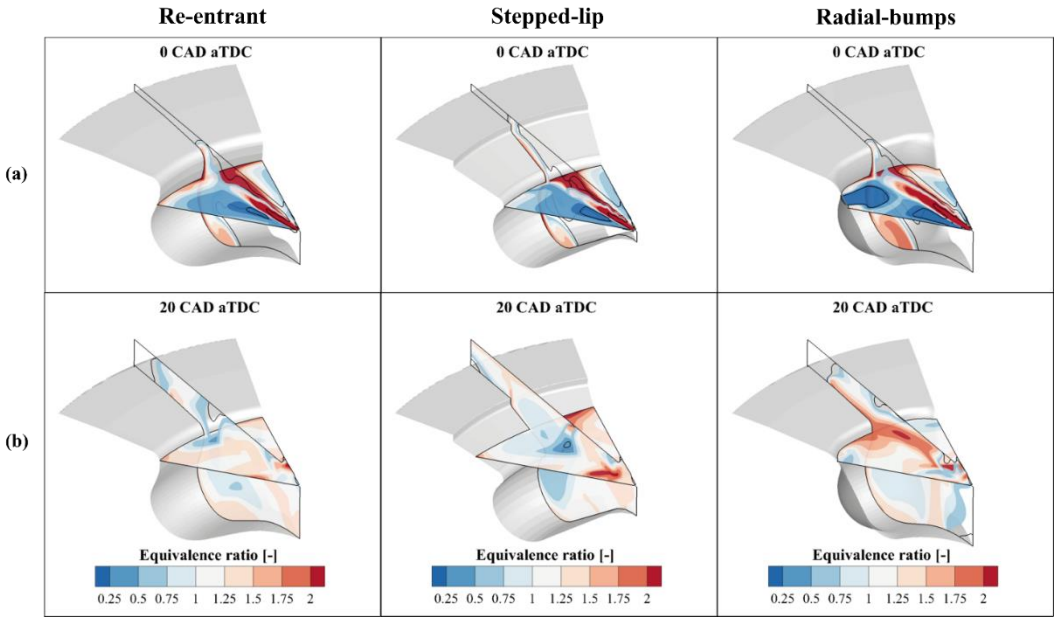

Figure 3–15: Nominal swirl ratio: equivalence ratio contour plot on the spray axis and cylinder axis planes. Black line: the constant temperature at 1500 K. (a) 0 CAD aTDC; (b) 20 CAD aTDC. Left: re-entrant; middle: stepped-lip; right: radial-bumps. WP3: 4000 RPM × 18.5 bar BMEP.

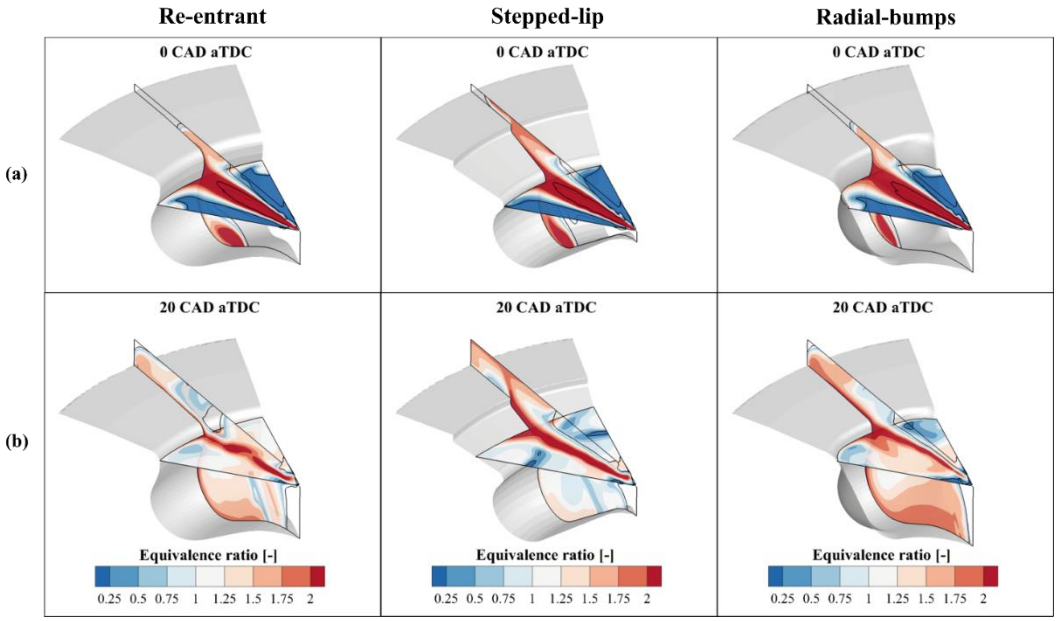

Figure 3–16: Zeroed swirl ratio: equivalence ratio contour plot on the spray axis and cylinder axis planes. Black line: the constant temperature at 1500 K. (a) 0 CAD aTDC; (b) 20 CAD aTDC. Left: re-entrant; middle: stepped-lip; right: radial-bumps. WP3: 4000 RPM × 18.5 bar BMEP.

At TDC considering the nominal swirl ratio of **Figure 3–15** – a, the stepped-lip and the radial-bumps bowls show a reduced flame-to-flame interaction with respect to the re-entrant bowl. Indeed, the stepped-lip bowl reduces the flames collision thanks to the higher flame velocity upward above the step. Interestingly, the radial-bumps bowl provides not only a reduced flame-to-flame interaction but also a different flame propagation along the bowl surface. The swirling flow leads an asymmetrical spray-wall interaction, and the fuel is driven by the bump toward the consecutive sector, where the available oxygen increases the air/fuel mixing. Instead, regarding the zeroed swirl ratio of **Figure 3–16** – a, a symmetric spray-wall interaction can be observed for all the piston bowls, providing a more intense radial-mixing zone (RMZ) especially for the re-entrant and the radial-bumps bowls. However, the behavior of the RMZ for the radial-bumps bowl is strongly affected by the geometry of the bump, as also noted in [38]. The bumps lead the fuel jets toward the cylinder center where the available oxygen enhances the air/fuel mixing. Nevertheless, this recirculation is intense only in the upper-bump region, while in the bottom-bump region the tumbling vortex is the main flow structure thanks to the high bowl reentrance, as highlighted in **Figure 3–5**. Therefore, the radial-bumps bowl leads to a more effective air/fuel mixing with the nominal swirl ratio due to the beneficial flow structures enabled by the combination of the swirling flow and the bump geometry. At +20 CAD aTDC, after the EOI of main event, the global air/fuel mixing for the re-entrant bowl is strongly affected by the swirl ratio. **Figure 3–15** – b shows for the nominal swirl ratio an almost homogeneous equivalence ratio near the stoichiometric range, while with the zeroed swirl ratio (**Figure 3–16** – b) the fuel rich zones are still present. Hence, the residual fuel is slowly oxidized, and this results in lower HRR in the late cycle as observed in **Figure 3–14**. Considering the stepped-lip bowl, the equivalence ratio distribution within the bowl is similar for both the swirl ratios. Indeed, for this piston design the air/fuel mixing is mainly guided by the fuel split on the step and this is slightly affected by the swirl ratio. Consequently, the HRR in the late cycle is comparable for the two different swirl ratios. For the radial-bumps bowl, the combination of high swirl ratio and the bumps still play a crucial role in the air/fuel mixing, providing a more homogenous mixture in the late cycle with respect to the zeroed swirl ratio case.

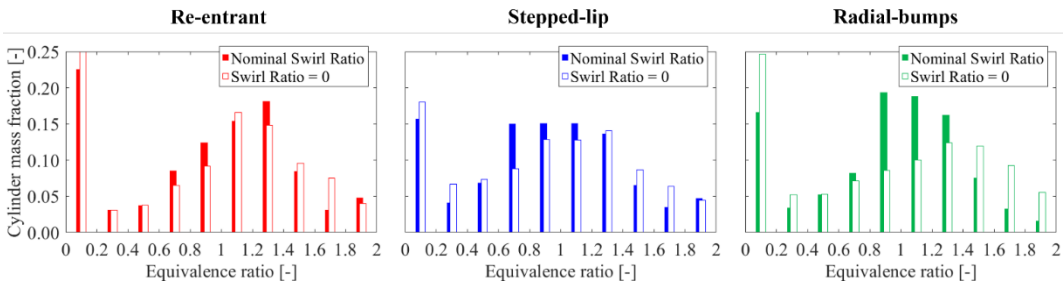

Figure 3–17: Equivalence ratio bins distribution for nominal and null swirl ratio at +20 CAD aTDC. Left: re-entrant; middle: stepped-lip; right: radial-bumps. WP3: 4000 RPM × 18.5 bar BMEP.

To highlight the swirl ratio impact on the combustion process, at +20 CAD aTDC the total cylinder mass was divided by the equivalence ratio into ten intervals, as highlighted in **Figure 3–17**. For all the piston bowls under investigation, the nominal swirl ratio provides the mode of the distribution closer to the stoichiometric range, suggesting faster combustion process. However, the radial-bumps bowl highlights the highest sensitivity to the swirl ratio, resulting in a strong increment of the cylinder mass fraction in the 0.8-1.2 equivalence ratio range under the nominal swirl ratio.

3.3.3 EGR and rail pressure sensitivity

At the partial load WP1, different EGR rates and rail pressure levels were investigated. Three EGR rates were adopted: the baseline EGR for the re-entrant bowl and +/-5%. The EGR rate was varied by changing the gas species concentration at the IVC. Then, for each EGR rate, two rail pressure were considered: the baseline value and +50%. The injection profile for the higher rail pressure was obtained thanks to the injector model developed in [25,26]. For each investigated calibration, the engine load was kept constant by controlling the energizing time of the main injection. **Figure 3–18** shows the EGR and rail pressure sensitivity in terms of ISFC, Indicated Specific NOx (ISNOx) and soot. All the results are normalized with respect to the baseline engine configuration (i.e., re-entrant bowl – nominal EGR – nominal rail pressure). **Figure 3–18** – a shows under nominal EGR and rail pressure a reduced ISFC for the stepped-lip and the radial-bumps bowl with respect to the re-entrant bowl (-1% and -4%, respectively). Then, going toward higher EGR rate, a further ISFC reduction can be observed for both the stepped-lip and the radial-bumps bowls, thus suggesting

higher EGR tolerance thanks to the enhanced mixing process. As previously assessed, the radial-bumps bowl leads to higher HRR and the resulting higher temperature provides higher NOx as shown in **Figure 3–18** – b. However, thanks to higher EGR tolerance, a further increase on the EGR rate can be used to control NOx. Regarding the soot emissions of **Figure 3–18** – c, both the stepped-lip and the radial-bumps bowls highlight an impressive soot reduction, -40% and -60% at baseline EGR, respectively. Moreover, the radial-bumps bowl shows a flat trade-off over the EGR sweep, thus confirming that a higher EGR can be adopted for NOx control without any soot penalties. After the EGR sensitivity, the rail pressure was increased of +50% with respect to the nominal condition and the results are reported in **Figure 3–18** with dashed lines. As expected, by increasing the rail pressure the ISFC is further improved due to the higher premixed combustion. Nevertheless, the radial-bumps bowl with the baseline rail pressure still shows lower ISFC with respect to the other bowls with higher rail pressure. Additionally, the enhanced premixed combustion provides higher flame temperature, resulting in higher NOx formation. However, the radial-bumps bowl shows the lowest NOx increment with respect to the baseline rail pressure. Considering the soot emissions, the higher rail pressure provides a strong soot reduction thanks to the improved spray atomization that mitigates the soot formation. It is worth to note that at baseline EGR, the re-entrant bowl with higher rail pressure leads to comparable soot than with the radial-bumps bowl at baseline rail pressure. Therefore, the soot reduction reached by increasing the rail pressure with the re-entrant bowl can be also obtained for the radial-bumps bowl due to the improved mixing, thus limiting any losses due to the higher power demand of the high-pressure fuel pump.

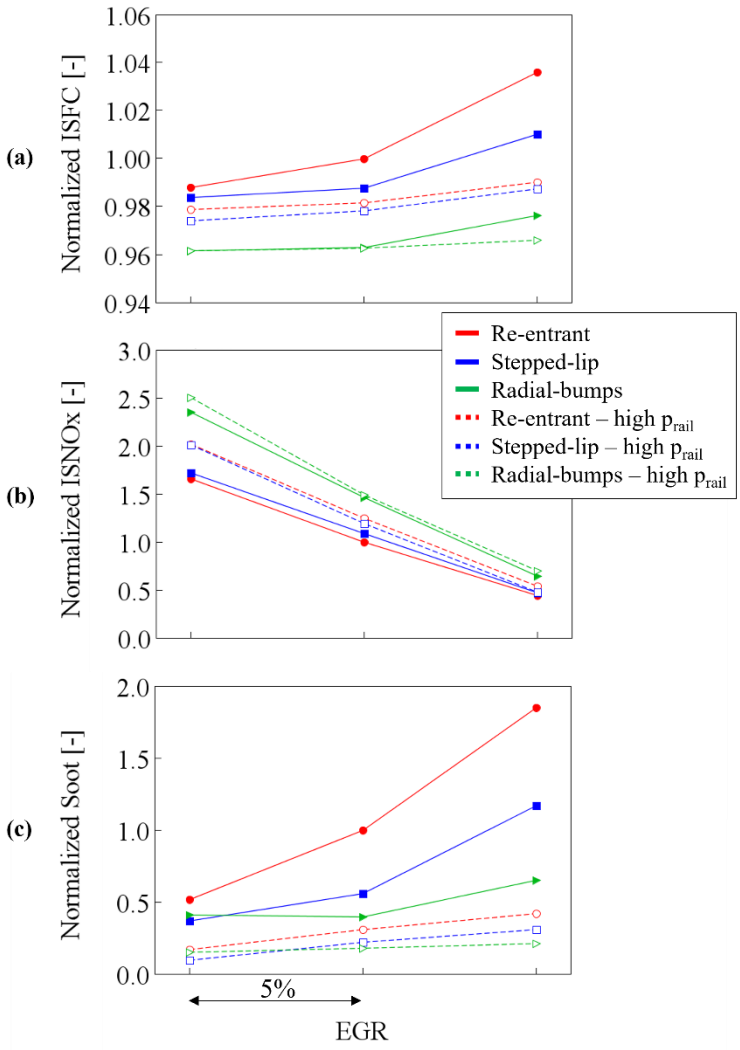

Figure 3–18: EGR and rail pressure sweep. (a) ISFC; (b) ISNOx; (c) soot normalized with respect to baseline engine configuration. WP1: 1500 RPM × 5.0 bar BMEP.

Chapter 4

Hybrid bowl design

Part of the work described in this Chapter was also previously published in the following publications:

- Millo, F., Piano, A., Roggio, S., Bianco, A. et al., "Numerical Assessment of Additive Manufacturing-Enabled Innovative Piston Bowl Design for a Light-Duty Diesel Engine Achieving Ultra-Low Engine-Out Soot Emissions," SAE Int. J. Engines 15(3):2022, https://doi.org/10.4271/03-15-03-0022.
- Millo, F., Piano, A., Roggio, S., Pastor, J.V. et al., "Mixture formation and combustion process analysis of an innovative diesel piston bowl design through the synergetic application of numerical and optical techniques," Fuel, 2022, 309:122144, https://doi.org/10.1016/j.fuel.2021.122144.
- Piano, A., Roggio, S., Millo, F., García, A. et al., "Numerical and optical soot characterization through 2-color pyrometry technique for an innovative diesel piston bowl design", Fuel, 2023, 333:126347, https://doi.org/10.1016/j.fuel.2022.126347.

4.1 Introduction

In order to understand the potential synergies between the stepped-lip and the radial-bumps designs, an innovative piston bowl proposal was designed, named

'hybrid'. It combines an annular recess step and a number of radial bumps equal to the injector nozzle holes in the inner bowl rim. The proposed combustion system features the same bore and squish height of the re-entrant bowl, while a reduced compression ratio (i.e 15:1) was considered. The adoption of lower compression ratio for the new combustion system was proposed by the supplier as enabler for a lightweight yet high-power density engine and for the improvement of the engine-out emissions [85]. The 15:1 compression ratio was selected as best balance between rated power, emissions and cold startability requirements. **Figure 4–1** – right shows the hybrid piston bowl under investigation.

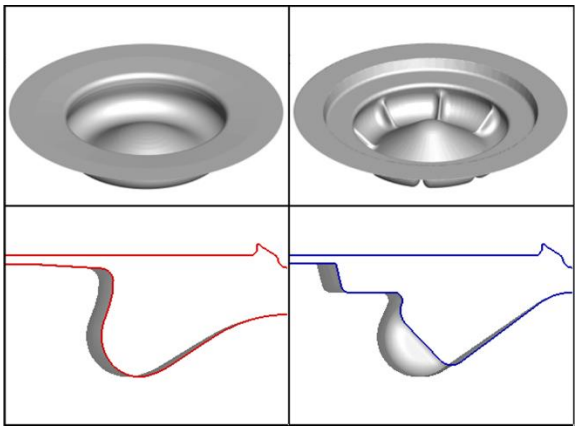

Figure 4–1: Piston bowl geometries under investigation. Left: re-entrant; right: hybrid.

In the first part of the chapter, the in-cylinder flow field and the mixing process were investigated under non-reacting conditions. To this aim, the full cylinder geometry was assessed at the partial load engine working point 1500 RPM x 4.6 bar of Indicative Mean Effective Pressure (IMEP). Then, the sector mesh was adopted for the combustion simulations under the three different engine working points highlighted in **Table 2–2**. The combustion analysis was carried out keeping the engine calibration parameters adopted for the conventional re-entrant design, thus highlighting only the effect of a novel piston design on the combustion process. Then, to maximize the potential benefits provided by the innovative hybrid piston bowl, a spray targeting optimization was carried out considering different injector protrusions and two swirl ratio levels. In the last part of the chapter, the 3D-CFD results were compared with experimental data obtained from an optical access engine based on the same engine architecture. With this aim, the Combustion Image Velocimetry (CIV) and OH* chemiluminescence techniques were adopted for the characterization of the flame

structure. Then, the numerical soot distribution was compared with the 2-colour pyrometry optical soot density (KL). For the purpose, two numerical methodologies were designed as previously discussed in the chapter '2.4 Optical engine analysis'. It is worth noting that just a qualitative comparison between 3D-CFD and experimental results was performed due to the intrinsic differences in terms of engine layout (i.e., metal engine vs optical engine). Indeed, the piston used for the optical access engine showed lower heat transfer due to lower quartz heat conductivity, and higher mechanical deformation [71]. Moreover, the optical engine was affected by a not negligible blow-by which was instead not modeled in the 3D-CFD environment.

4.2 3D-CFD analysis

4.2.1 Mixing-only analysis

The effect of the piston bowl design on the in-cylinder flow field and the mixing process was investigated through non-reacting simulations of the full-cylinder geometry. With this analysis the spray/wall interaction was investigated, avoiding the combustion influence on the turbulent structures. **Figure 4–2** shows the evolution of the swirl ratio and the injection rate profile for the piston bowls under investigation.

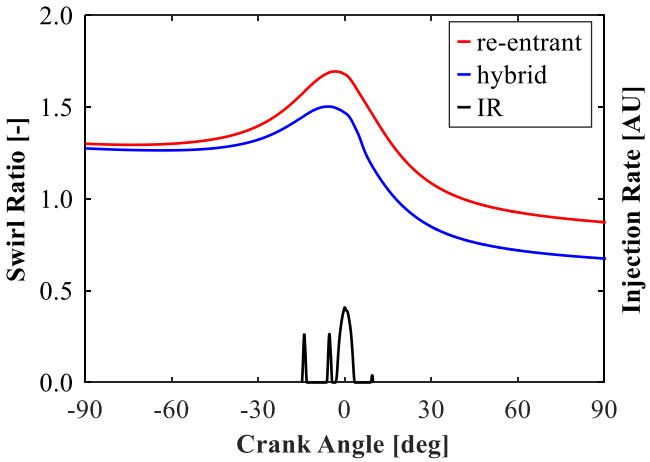

Figure 4–2: Swirl ratio and injection rate profile for the analyzed combustion systems. Engine operating condition: 1500 RPM x 4.6 bar IMEP.

Near the TDC, the re-entrant bowl shows higher swirl amplification than the hybrid design. This is due to the combined effect of the stepped-lip and radial-bumps bowls. Indeed, on one side the reduced squish area for the hybrid design (see **Figure 4–1**) provides a lower squish flow and thereby lower swirl amplification, as previously observed in **Figure 3–4**. On the other side, the radial bumps break the swirling flow, thus reducing its intensity. To further understand the radial bumps impact on the swirl motion, the velocity field was assessed at the Start of Injection (SOI) on a plane Z cutting the radial bumps in the upper region. **Figure 4–3** shows at -14 CAD aTDC the component of the velocity vectors that is tangential to the plane Z (called 'projected velocity'), with uniform size and colored according to the projected velocity magnitude.

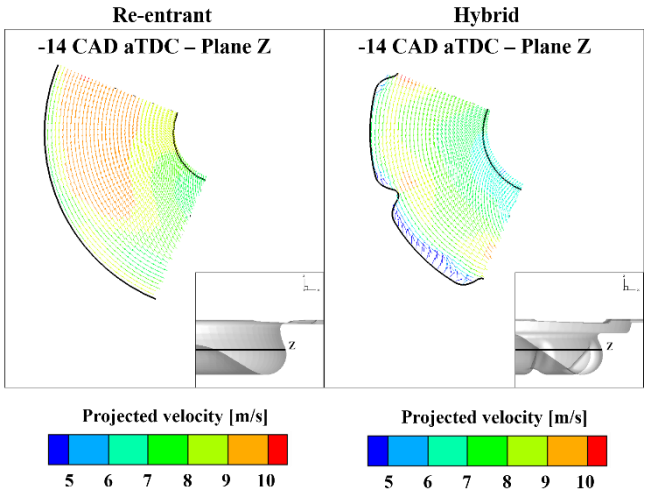

Figure 4–3: Velocity vectors at -14 CAD aTDC colored according to the magnitude of the projected velocity on the selected plane Z. Left: re-entrant; right: hybrid. Engine operating condition: 1500 RPM x 4.6 bar IMEP.

The flow field for the re-entrant bowl is governed by the swirl motion, while for the hybrid bowl is strongly affected by the bump geometry. The turbulence level is enhanced by the flow separation occurring on the bump tip, while a reduction of velocity can be observed in the stagnation zone between two consecutive radial bumps. Then, the piston bowl effect on the flow field was also investigated after the EOI of main event for three different horizontal planes, parallel to the cylinder head, as highlighted in **Figure 4–4**. The plane Z1 refers to the step region, while both the plane Z2 and Z3 refers to the radial bump region, in the upper and bottom part, respectively.

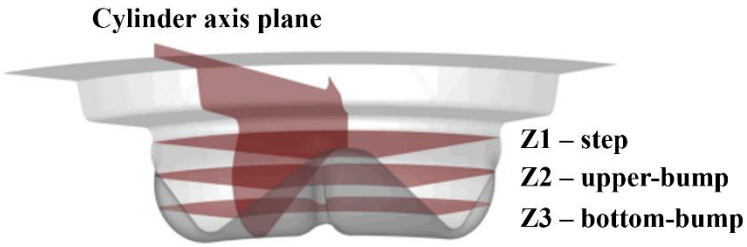

Figure 4–4: Planes selected to represent the numerical results.

The projected velocity in the selected planes at +5 CAD aTDC is shown in **Figure 4–5**. Considering the plane Z1, the flow motion is swirl supported for both the piston bowls under investigation, as reported in **Figure 4–5** – a. In addition, the jet-to-jet interaction with the hybrid bowl is minimized due to the spray split on the step, which reduced the jet tangential propagation and redirects the jet above the step. For the plane Z2 of **Figure 4–5** – b, the radial bumps impact on the flow field is clearly visible. The hybrid design remarkably affects the swirling flow, breaking its organized macro structures between two consecutive bumps. Near the bump tip, the high jet momentum is redistributed as vortices over the bump profile and consequently, the jet-to-jet interaction is reduced with respect to the re-entrant bowl. For the plane Z3 of **Figure 4–5** – c, two counter rotating vortices can be observed due to the jet-to-jet interaction. Instead, the bottom-bump curvature for the hybrid design results in higher fuel jet propagation towards the piston center. Nevertheless, due to the swirling flow, the spray/wall interaction occurs asymmetrically close to the bump region.

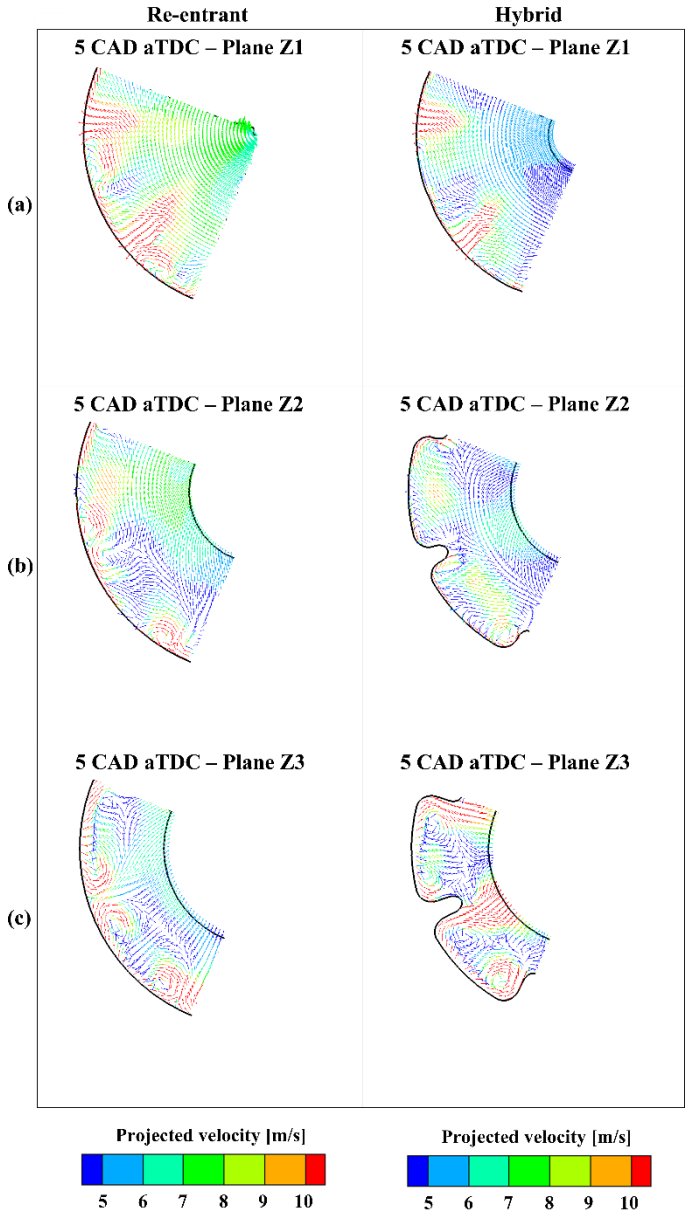

Figure 4–5: Velocity vectors at +5 CAD aTDC colored according to the magnitude of the projected velocity on the selected cutting planes Z1 (a), Z2 (b) and Z3 (c). Left: re-entrant; right: hybrid. Engine operating condition: 1500 RPM x 4.6 bar IMEP.

The piston bowl impact on the mixing process was analyzed thanks to the equivalence ratio distribution after the EOI of main event, at +5 CAD aTDC, as shown in **Figure 4–6**. Firstly, the vertical plane passing through the spray axis and the cylinder axis (Cylinder axis plane of **Figure 4–4**) was considered as reported

in **Figure 4–6** – a. The hybrid bowl highlights a more intense tumbling vortex that drives the fuel jet toward the bowl center. Considering the plane Z1 of **Figure 4–6** – b, the re-entrant bowl shows a more intense jet-to-jet interaction in the step region. In the upper region of the bump (plane Z2 of **Figure 4–6** – c), the radial bumps for the hybrid design minimize the jet-to-jet interaction and the fuel jet is driven into the consecutive sector, as highlighted by the black arrow. This results in higher air/fuel mixing onto the jet front due to the available oxygen present in the region. The different fuel jet evolution can be also observed in the bottom region of the bump (plane Z3 of **Figure 4–6** – d). In this zone, for the hybrid bowl the jet propagation toward the piston center is remarkably enhanced, as confirmed by the higher fuel concentration within the black circle. Therefore, the available oxygen located in the piston center improves the air/fuel mixing into the jet front.

The equivalence ratio distribution was also investigated during the post injection event, at +10 CAD aTDC, as shown in **Figure 4–7**. During the post injection, the more intense tumbling vortex for the hybrid bowl drives the fuel jet toward the bowl center. This effect is clearly visible for the vertical plane of **Figure 4–7** – a and the plane Z1 of **Figure 4–7** – b. Moving to the upper region of the bump (plane Z2 of **Figure 4–7** – c), the re-entrant bowl highlights the merging of two adjacent fuel jets that reduces their propagation toward the dome. Instead, the radial bumps of the hybrid design can keep the two adjacent jets separate, thus avoiding extremely fuel rich zones. Therefore, a reduced air/fuel mixing rate is expected for the re-entrant bowl during the late phase of the injection. Considering the bottom region of the bump (plane Z3 of **Figure 4–7** – d), both the piston bowls highlight the higher fuel concentration near the piston center, but for the hybrid bowl the fuel rich cloud is reduced due to the higher tumbling vortex.

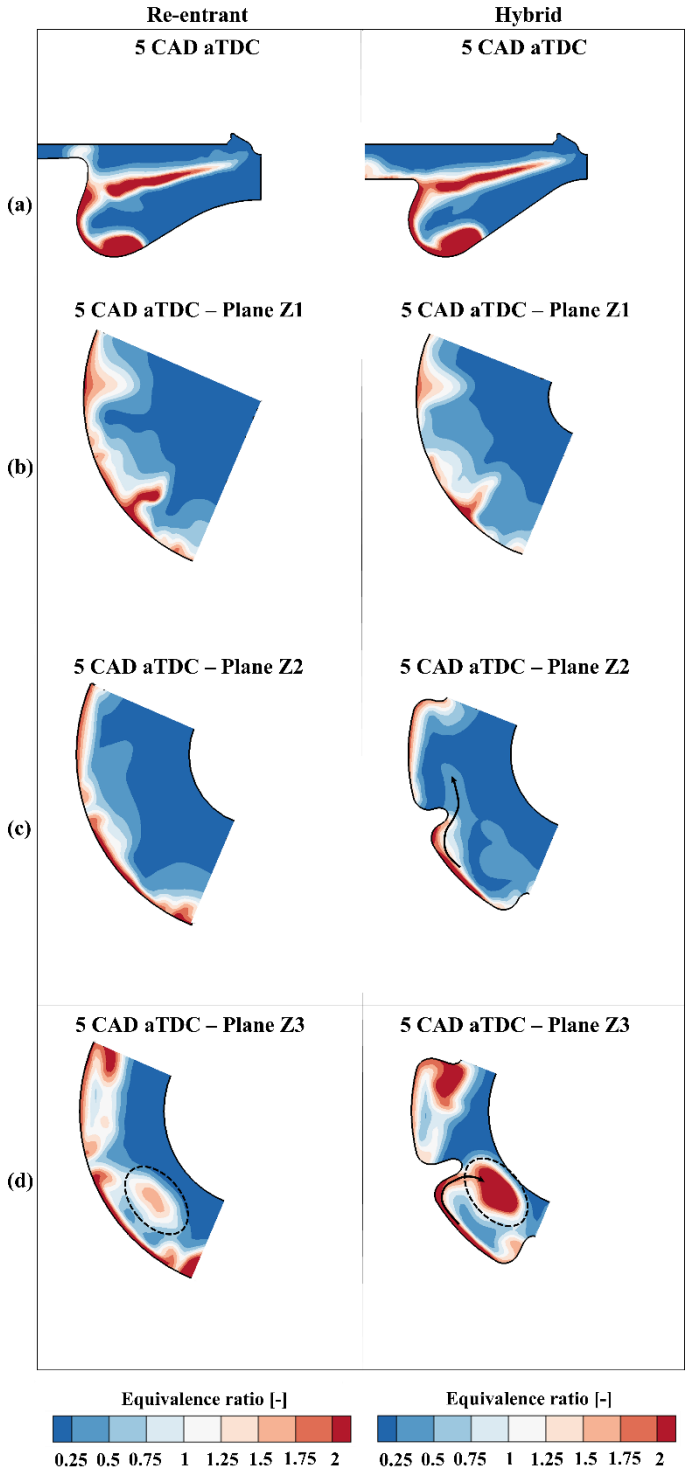

Figure 4–6: Equivalence Ratio contour plot at +5 CAD aTDC on the selected cutting planes: vertical plane (a), Z1 (b), Z2 (c) and Z3 (d). Left: re-entrant; right: hybrid. Engine operating condition: 1500 RPM x 4.6 bar IMEP.

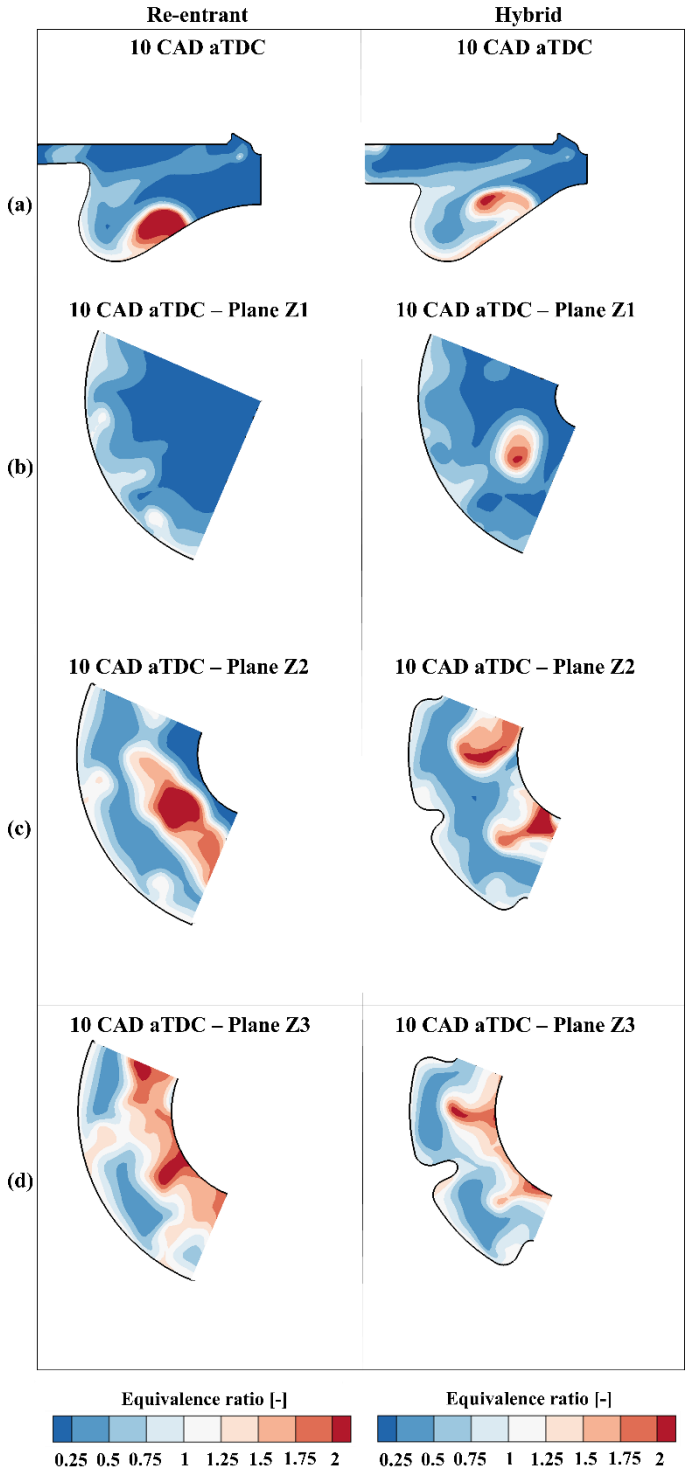

Figure 4–7: Equivalence Ratio contour plot at +10 CAD aTDC on the selected cutting planes: vertical plane (a), Z1 (b), Z2 (c) and Z3 (d). Left: re-entrant; right: hybrid. Engine operating condition: 1500 RPM x 4.6 bar IMEP.

For the global characterization of the mixing process, the mixing rate index already described in **Figure 3–8** was used. More in detail, the total cylinder mass was binned by equivalence ratio in twenty intervals from 0.0 to 2.0, where the 0.1-0.2 bin represents the intake flow (pure ambient gas combined with EGR), while the 1.9-2 bin corresponds to the injected fuel mass. Then, the cylinder mass fraction for each bin was traced on bar chart and a contour plot was designed collecting all the bar charts for each crank angle, as outlined in **Figure 3–8**. Finally, to better identify the difference between the re-entrant and the hybrid bowls, the cylinder mass fraction delta (cylinder mass fraction$_{hybrid}$ – cylinder mass fraction$_{re\text{-}entrant}$) was assessed, as reported in **Figure 4–8**. After the EOI of main event, from +5 CAD aTDC, the hybrid bowl leads to faster air/fuel mixing. Indeed, a negative delta is highlighted in the rich equivalence ratio bins (1-1.9), while a positive delta is shown in the 0.2-0.8 equivalence ratio bins, close to the global average value 0.5. Similar results are highlighted after the EOI of post injection, from +10 CAD aTDC. The hybrid bowl shows a negative delta for both the intake flow composition (0.1-0.2 bin) and the equivalence ratio bins 1.2-1.9. This is due to the enhanced air/fuel mixing rate that results in higher positive delta in the equivalence ratio bins 0.2-0.8, close to the global average value 0.5.

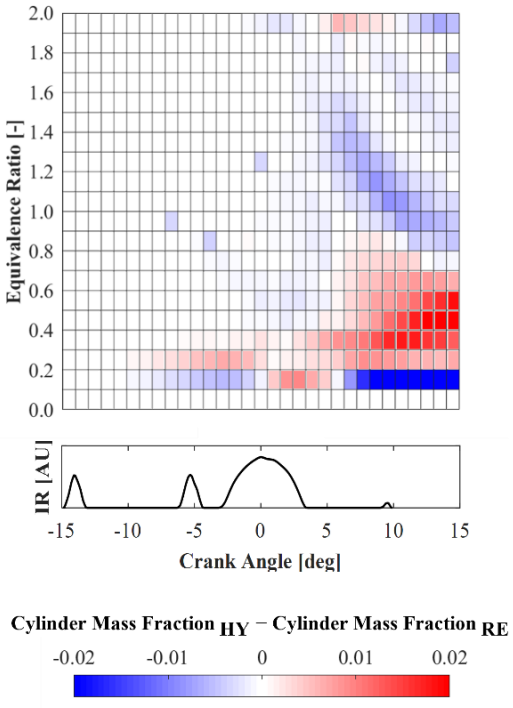

Figure 4–8: Cylinder mass fraction difference between hybrid and re-entrant bowls. Engine operating condition: 1500 RPM x 4.6 bar IMEP.

4.2.2 Combustion analysis

Once assessed the mixing process, the combustion system effect on the combustion evolution was carried out. With this aim, the HRR and the injection rate profile for the three different WPs highlighted in **Table 2–2** were considered. **Figure 4–9** shows the HRR for the full load engine operating conditions (WP3). From -20 to -5 CAD aTDC, during the free jet development, the piston bowl geometry does not affect the combustion and the HRR are comparable. Going toward the TDC, the hybrid bowl highlights a more intense HRR with respect to the re-entrant bowl, due to the improved air/fuel mixing process. Close the EOI, the HRR become again comparable, due to the higher fuel concentration that goes above the step of the hybrid design, resulting in lower air utilization within the bowl. Then, in the late cycle the re-entrant bowl shows higher HRR than with the hybrid design due to the higher residual fuel to be burned.

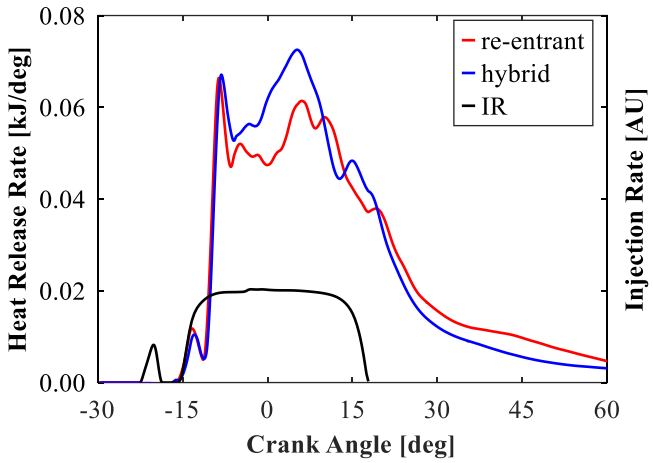

Figure 4–9: Heat Release Rate and injection rate profile. WP3: 4000 RPM x 18.5 bar BMEP.

For a deeper investigation of the combustion process, the equivalence ratio distribution was assessed during the main injection event, as shown in **Figure 4–10** for the three horizontal planes defined in **Figure 4–4**. In this case, a two-sector representation was chosen to better highlight the radial bump region. Focusing on the step region (plane Z1 of **Figure 4–10** – a), the hybrid bowl shows a reduced flame-to-flame interaction, since the fuel jet redistribution above the step reduces the tangential velocity of the flame over the bowl surface. For the upper bump

region (plane Z2 of **Figure 4–10** – b), the radial bumps strongly mitigate the flame-to-flame interaction and simultaneously drive the flame toward the consecutive sector, where a high oxygen concentration is present, as highlighted by the black dashed arrow. This effect improves the air entrainment onto the flame front and thereby the combustion rate, as observed in the HRR of **Figure 4–9**. Going to the bottom bump region (plane Z3 of **Figure 4–10** – c), the re-entrant bowl shows a strong interaction between the two adjacent flames, thus limiting the oxidation rate. Instead, for the hybrid design the adjacent flames appear well separated by the radial bumps and the surrounding oxygen can be efficiently mixed, thus leading to a faster combustion process.

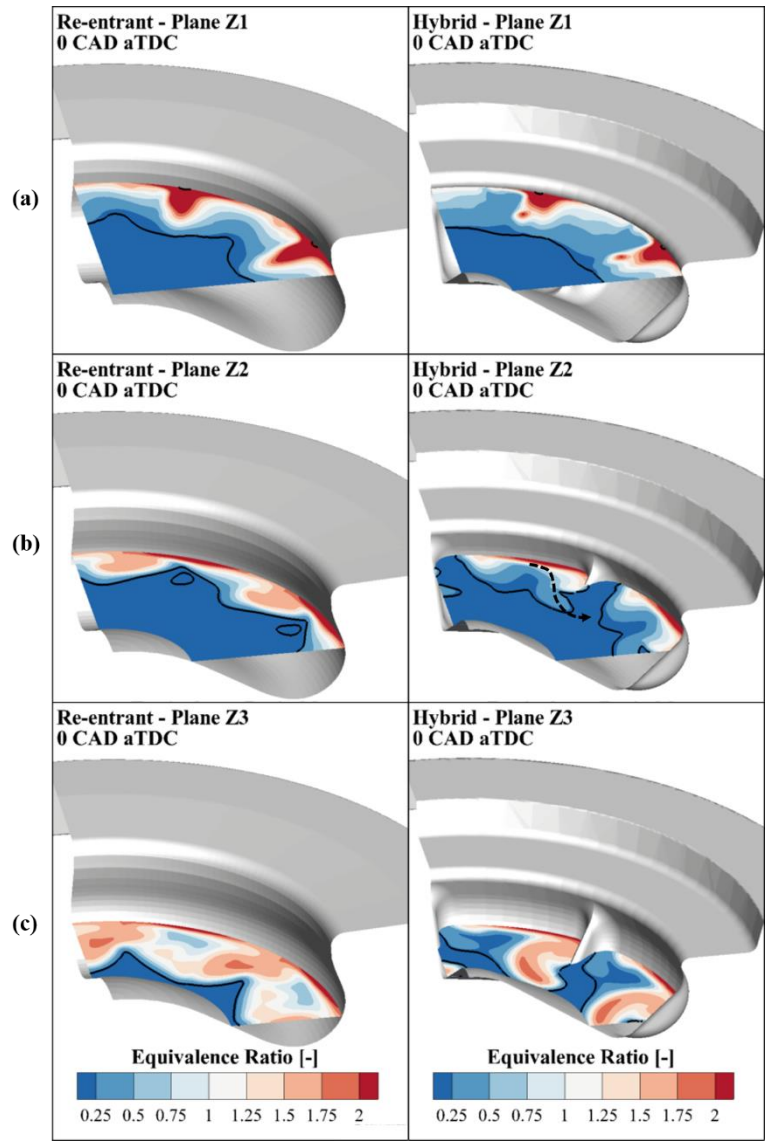

Figure 4–10: Equivalence Ratio contour plot at TDC on the selected cutting planes Z1 (a), Z2 (b) and Z3 (c). Black line: isoline at constant temperature equal to 1500K. Left: re-entrant; right: hybrid. WP3: 4000 RPM x 18.5 bar BMEP.

The combustion process was also investigated under partial load engine operating conditions (WP1 of **Table 2–2**) and the HRR for each piston design is shown in **Figure 4–11**. The re-entrant bowl shows a higher premixed main combustion close to the TDC. Indeed, the higher swirl ratio for the re-entrant bowl (as highlighted in **Figure 4–2**), reduces the intensity of the flame impingement on the bowl surface. The resulting improved air entrainment

enhances the combustion rate. However, after the EOI of main event, the re-entrant bowl shows a reduced combustion rate due to the higher flame-to-flame interaction. During the after injection burn-out, the hybrid design highlights a higher HRR thanks to the fuel slit on the step that increases the fuel concentration in the squish region, enhancing the air utilization as also observed in [84].

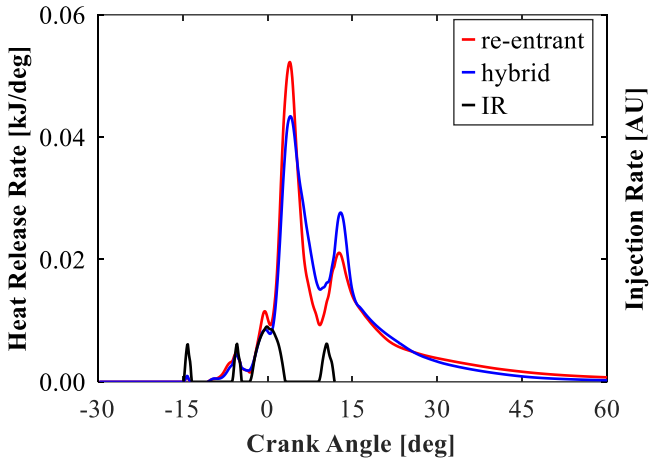

Figure 4–11: Heat Release Rate and injection rate profile. WP1: 1500 RPM x 5.0 bar BMEP.

Once assessed the combustion behavior, the impact of piston design on the soot formation/oxidation process was investigated thanks to the PM soot model. The results of the model in terms of soot mass and net soot formation rate are reported in **Figure 4–12**. After the EOI of main event, the hybrid design shows a reduced net soot formation rate which results in lower soot mass with respect to the re-entrant design. This is due to the reduced flame-to-flame interaction and the improved air utilization enabled by the hybrid design. Going ahead in the combustion, from the EOI of after event to +35 CAD aTDC, during the burn-out of the residual rich zones, the hybrid design shows a strong increment of the soot oxidation rate with respect to the re-entrant bowl. A deeper investigation on the in-cylinder soot mass distribution was also carried out. To this aim, the computational domain was divided in bins depending on the soot mass density of each cell, as already described for **Figure 3–11**. Specifically, the bin 1 is representative of region with low soot density, while the bin 2 represents the high soot density region. **Figure 4–13** shows the bin 1 (blue) and bin 2 (red) soot-density iso-surfaces at the two crank angle degrees, θ_1 and θ_2 (+10 and +25 CAD

aTDC), highlighted in **Figure 4–12**. At $\theta = \theta_1$, after the EOI of main event (**Figure 4–13** – a), the re-entrant bowl highlights a wider red zone into the periphery of the sectors due to the flame-to-flame interaction that increases the soot formation. Contrarily, the hybrid design mitigates this effect, and a lower soot density can be observed in the periphery of the sectors. Instead, the highest soot content is localized in the centre region between two consecutive radial bumps. In addition, the fuel split on the step promotes the combustion in the squish region where a cloud of low soot density can be observed. Late in the combustion, at $\theta = \theta_2$, the high soot density zones are fully oxidized for both the piston bowls, as highlighted in **Figure 4–13** – b. Nevertheless, the re-entrant bowl shows a higher soot mass within the bowl. For the hybrid design, the radial bumps promote a faster flame recirculation toward the available oxygen in the cylinder centre. Also, the soot mass above the step previously formed is fully oxidized. Therefore, the combination of the radial bumps and the step leads to a stronger soot mass oxidation for the hybrid design.

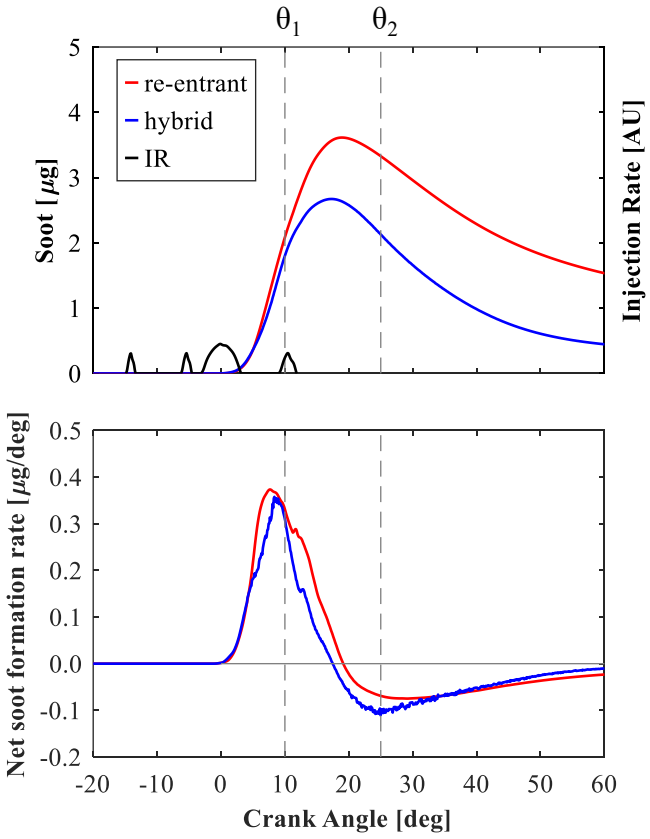

Figure 4–12: Soot PM model results. Top: In-cylinder Soot mass; bottom: Net formation rate of in-cylinder soot mass. WP1: 1500 RPM x 5.0 bar BMEP.

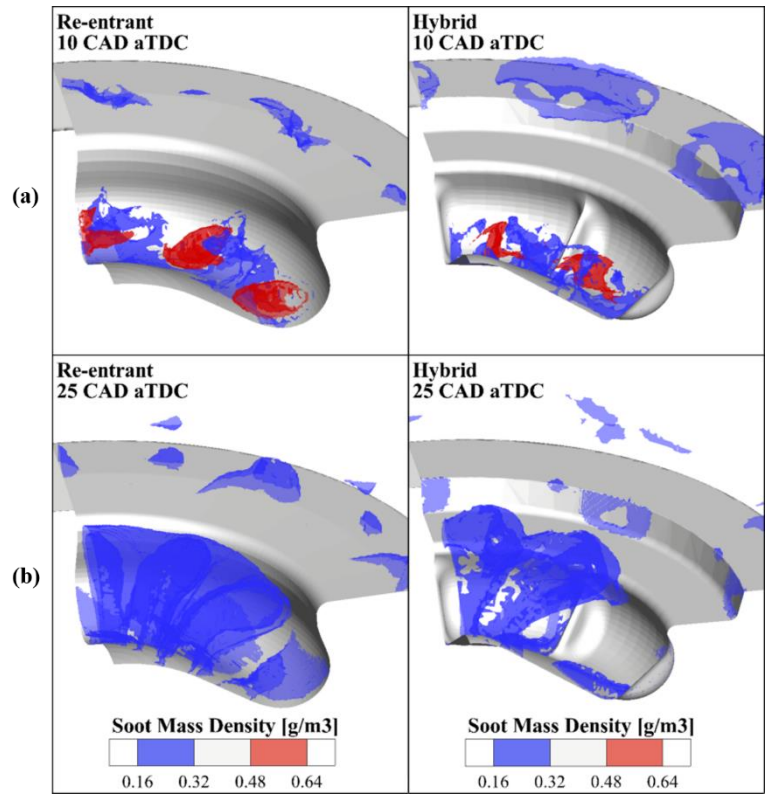

Figure 4–13: Bin 1 (blue) and bin 2 (red) soot density iso-surfaces. Left: re-entrant; right: hybrid. WP1: 1500 RPM x 5.0 bar BMEP.

The combustion and soot emission analysis were also carried out at the WP2 of **Table 2–2**. **Figure 4–14** shows the HRR for each piston design under investigation. As already observed for WP1, near the EOI of main event, when the flame-wall and flame-to-flame interactions are crucial for the combustion process, the hybrid bowl highlights a more intense HRR than with the re-entrant bowl. Also, for WP2 the difference in terms of HRR becomes even more evident due to the increased injected mass.

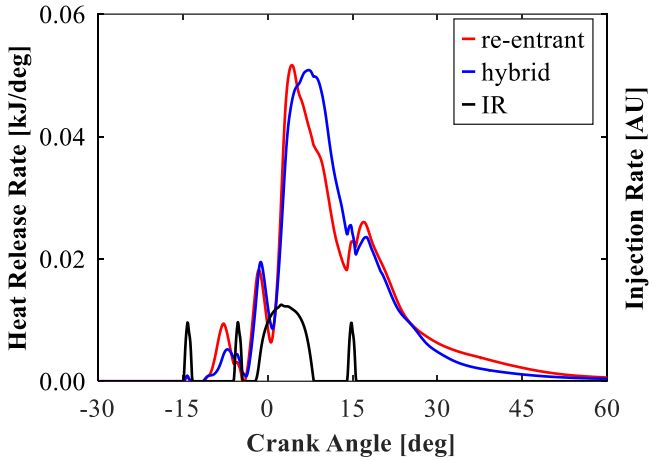

Figure 4–14: Heat Release Rate and injection rate profile. WP2: 2000 RPM x 8.0 bar BMEP.

The retarded injection timing and the higher after injection mass with respect to WP1 could impact the soot oxidation process, therefore a further investigation on soot evolution was carried out. **Figure 4–15** shows the soot mass and net soot formation rate for each bowl under investigation. After the EOI of main event, the hybrid bowl shows a reduced soot due to the lower net soot formation rate. Nevertheless, the soot attenuation is lower with respect to the WP1, since the higher injected mass after the TDC leads to higher fuel concentration above the step, where a more intense soot formation is expected. Going ahead in the combustion, from +15 to +30 CAD aTDC, different behavior can be observed between the two piston designs. The re-entrant bowl shows a continuous reduction in terms of net soot formation rate. Conversely, the hybrid design provides a double steps trend of the net soot formation rate. In the first step, the soot oxidation is balanced by the higher soot formation due to the after-injection combustion, thus leading to a stable net soot formation rate. In the second step, the net soot formation rate decreases, reaching similar value than with the re-entrant bowl.

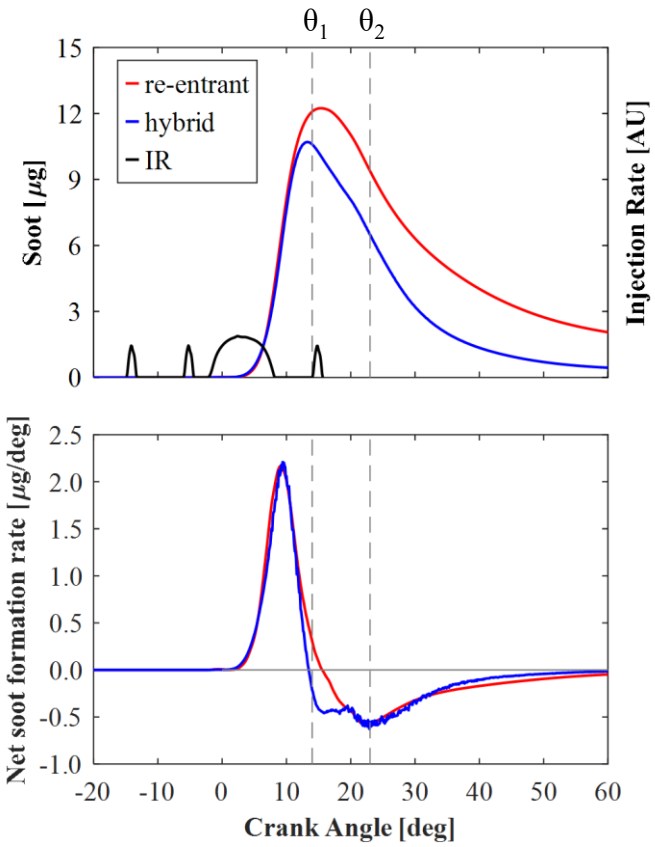

Figure 4–15: Soot PM model results. Top: In-cylinder Soot mass; bottom: Net formation rate of in-cylinder soot mass. WP2: 2000 RPM x 8.0 bar BMEP.

The soot density distribution was also investigated, as already described for WP1. **Figure 4–16** reports the low soot density (bin 1) and high soot density (bin 2) iso-surfaces at two crank angle degrees, $\theta_1$and θ_2, highlighted in **Figure 4–15**. As already observed for WP1, after the EOI of main event ($\theta = \theta_1$), the re-entrant bowl promotes higher soot formation in the periphery of the sectors due to the flame-to-flame interaction. Instead, for the hybrid design two different regions with high soot density can be observed. On one side, the higher tumbling vortex shifts the flame toward the cylinder center, thus leading to higher air entrainment. On the other side, the fuel split on the step increases the fuel concentration above the step, thus resulting in higher soot formation in the squish region. This behavior is more evident than with WP1 due to the higher injected mass after the TDC. During the combustion of the after injection ($\theta = \theta_2$), the piston bowls

shows different behavior. For the re-entrant bowl, the after injection impingement with piston bowl rim, thus limiting its propagation in the squish region and an intense soot formation is observed in the jet periphery (see the black dashed circles). For the hybrid bowl, the enhanced flame recirculation toward the piston center leads to a strong interaction between the flame and the after injection spray core, increasing the soot formation and providing the stable phase of the net soot formation rate (see **Figure 4–15** – bottom). However, the after injection goes above the step (see the black dashed circle) and its combustion increases the local temperature, thus promoting a faster soot oxidation in the squish region.

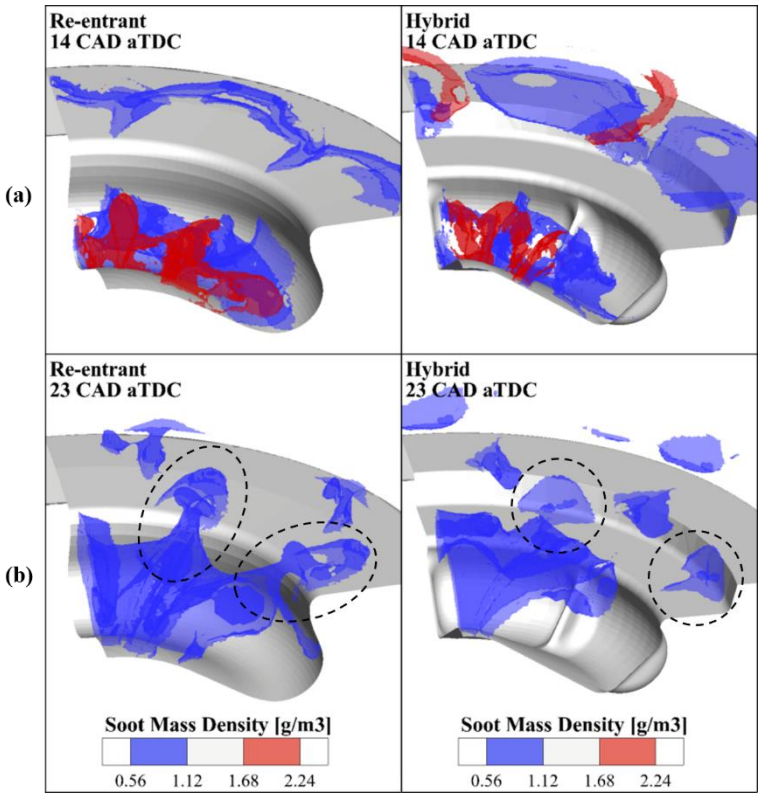

Figure 4–16: Bin 1 (blue) and bin 2 (red) soot density iso-surfaces. Left: re-entrant; right: hybrid. WP2: 2000 RPM x 8.0 bar BMEP.

4.2.3 Trade-offs

At partial load engine operating conditions (WP1, WP2), the combustion systems sensitivity in terms of engine-out emissions and fuel consumption was performed over an EGR sweep. The injection strategy (i.e., energizing time, dwell time and rail pressure) was unchanged and equal to the baseline calibration, over the EGR sweep. **Figure 4–17** reports the soot-BSNOx and the BSFC-BSNOx trade-offs for the WP1. The results are normalized with respect to the baseline configuration, which is the re-entrant bowl with nominal EGR rate. The hybrid bowl leads to a flatness in the soot-BSNOx trade-off that allows a strong soot reduction even with high EGR for NOx control. At the baseline BSNOx, the hybrid design provides 70% soot reduction with respect to the re-entrant bowl, confirming the great potential on soot reduction thanks to the combination of the step and the radial bumps. Focusing on the BSFC-BSNOx trade-off, similar trends are highlighted for the two investigated piston bowls. At nominal EGR, the hybrid bowl provides less than 1% BSFC reduction. However, the improved mixing for the hybrid bowl allows an increment of the EGR with a negligible BSFC increment (less than 1%). **Figure 4–18** shows the soot-BSNOx and the BSFC-BSNOx trade-offs for the WP2. Even for this engine operating condition, the hybrid bowl provides a significant improvement of the soot-BSNOx trade-off. At baseline BSNOx, a 70% soot reduction is reached together with a slight improvement of the BSFC (-1%).

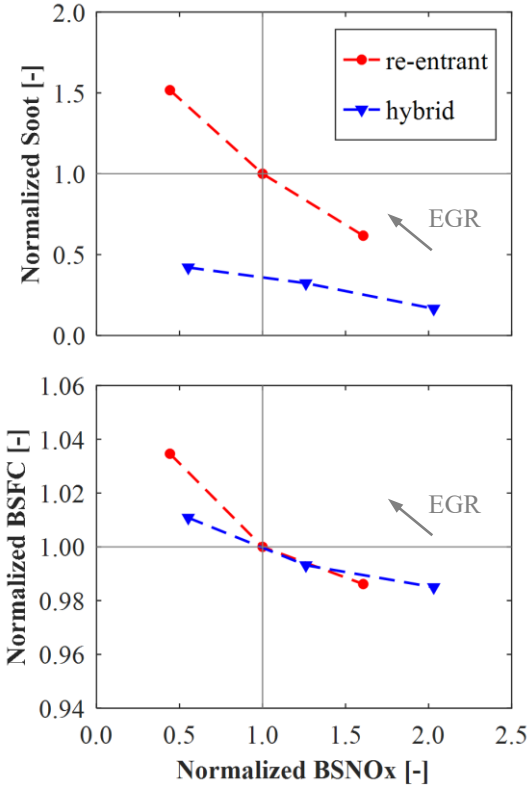

Figure 4–17: EGR sweep: normalized trade-offs with respect to baseline configuration. Top: Soot-BSNOx trade-off; bottom: BSFC-BSNOx trade-off. WP1: 1500 RPM x 5.0 bar BMEP.

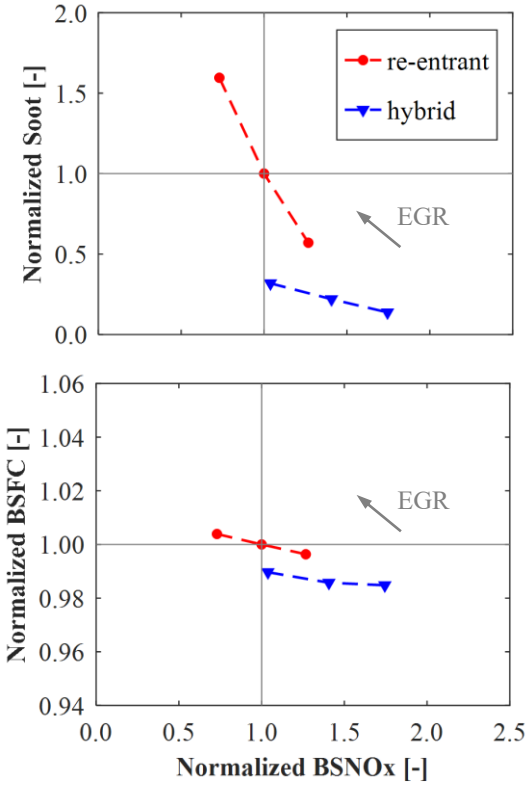

Figure 4–18: EGR sweep: normalized trade-offs with respect to baseline configuration. Top: Soot-BSNOx trade-off; bottom: BSFC-BSNOx trade-off. WP2: 2000 RPM x 8.0 bar BMEP.

4.2.4 Spray targeting optimization

To maximize the potential benefits thanks to the hybrid bowl, a spray targeting optimization was carried out by varying the injector protrusion. For this analysis, the baseline engine calibration in terms of boost pressure, EGR rate and injection parameters was considered. Additionally, two different swirl ratios (SR) were investigated, the baseline SR and half of the baseline SR. **Figure 4–19** shows the four injector protrusions under investigation: the nominal protrusion that is equal to the one adopted for the re-entrant bowl (0), 1mm and 2mm below (-1, -2), and 1mm above (+1) the nominal position. The optimization of the spray targeting was performed at the rated power conditions (WP3 of **Table 2–2**), and then validated at the partial load (WP1).

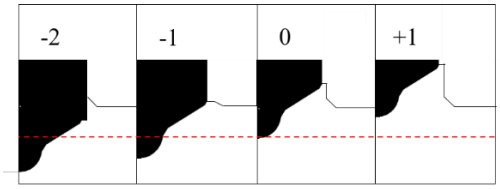

Figure 4–19: Injector protrusions for spray targeting optimization.

Figure 4–20 shows the soot-BSNOx and BSFC-BSNOx trade-offs for the WP3. The results are normalized with respect to the baseline engine configuration that is the re-entrant bowl with nominal protrusion and SR. At the nominal SR, the hybrid design shows a strong sensitivity to the injector protrusion especially in the soot-BSNOx trade-off. In particular, the nominal protrusion leads to the highest soot reduction with respect to the re-entrant bowl (-40%). Then, moving to different protrusions results to higher soot, due to the unbalanced fuel split on the step. This effect also reduces the mixing-controlled combustion phase, thus leading to higher BSFC. Instead, considering the nominal protrusion (0) a 2% BSFC reduction is reached with respect to the re-entrant bowl. Halving the SR, the soot-BSFC sensitivity is reduced, as well as the NOx emissions. Even for this SR, the nominal protrusion provides the best result in terms of soot and BSFC. Nevertheless, with the halved SR, the hybrid design provides 2 times higher soot and +3% BSFC with respect to the re-entrant bowl. This suggests that the hybrid bowl requires higher SR to increase the air/fuel mixing and thus the combustion rate.

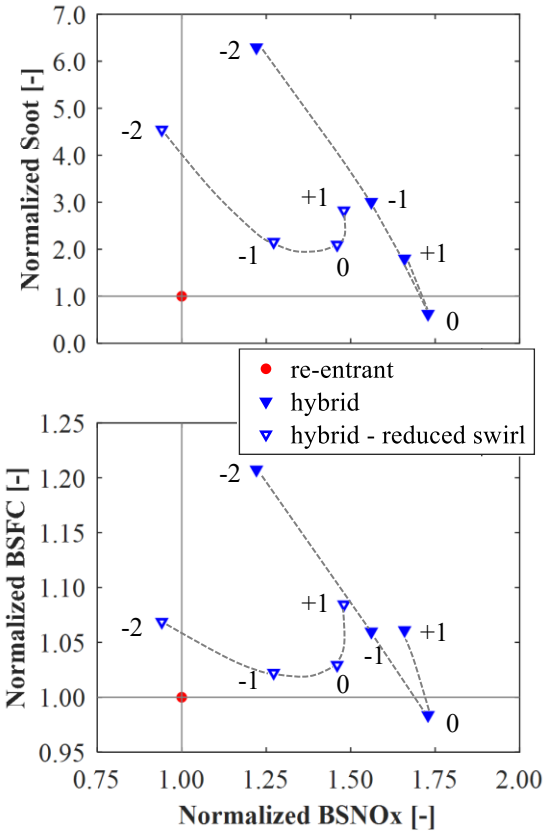

Figure 4–20: Injector protrusion sensitivity for two swirl ratio levels: normalized trade-offs with respect to the baseline configuration. Top: Soot-BSNOx trade-off; bottom: BSFC-BSNOx trade-off. WP3: 4000 RPM x 18.5 bar BMEP.

To better understand the injector protrusion sensitivity on the combustion process, a fuel rich mass index was designed as the cylinder mass with an equivalence ratio higher than 1.5 divided by the total cylinder mass, following the **Eq. 4–1**. Then, the cylinder rich mass fraction provides an index of the soot emission formation due to the rich mixture combustion.

$$\text{Cylinder rich mass fraction} = \frac{\text{Cylinder mass}_{\text{equiv ratio}>1.5}}{\text{Cylinder mass}} \qquad \text{Eq. 4–1}$$

This index was evaluated for two different computational volume: the whole combustion chamber and the volume below the horizontal plane cutting the step at TDC, as shown by the blue volume of **Figure 4–21**. By means of this volume's definition, quantitative information on the fuel split were evaluated. The results of the analysis are shown in **Figure 4–23**, for the three crank angle degrees during the injection event highlighted in **Figure 4–22**.

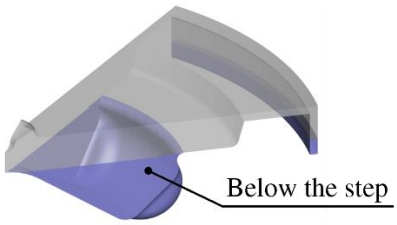

Figure 4–21: 'Below the step' volume defined as the volume below the horizontal plane cutting the step at TDC.

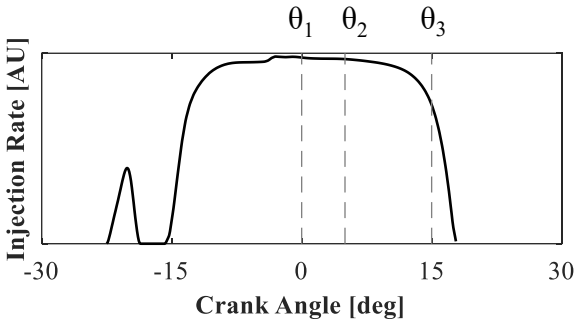

Figure 4–22: Injection Rate profile and crank angle degrees for injector protrusion sensitivity. WP3: 4000 RPM x 18.5 bar BMEP.

At TDC (**Figure 4–23** – a), the total cylinder rich mass is comparable for each injector protrusion, thus suggesting a similar air/fuel mixing rate although the different fuel split on the step. Instead, a significant variation of the cylinder rich mass below the step is observed by varying the injector protrusion. As shown in **Figure 4–20**, the highest soot and BSFC reduction are obtained with the nominal injector protrusion, where the optimal fuel split is observed: 50% of total cylinder rich mass is below the step. At +5 CAD aTDC, the -2 and -1 injector protrusions show a higher cylinder rich mass that is mainly located below the step. Therefore, the higher fuel concentration within the bowl promotes the soot formation, while

the reduced air utilization in the squish region decreases the combustion rate. The +1 injector protrusion, even without the optimal fuel split, shows a total cylinder rich mass that is comparable with the nominal injector protrusion, thus suggesting a similar oxidation rate. Near the EOI, at +15 CAD aTDC, the differences among the tested injector protrusions are more evident. The -2 and -1 injector protrusions show a remarkable increment of the cylinder rich mass, resulting in higher soot formation below the step, as already observed in **Figure 4–20**. In addition, the higher residual fuel below the step extends the combustion duration, thus leading to higher BSFC with respect to the nominal protrusion. Even with +1 injector protrusion, the total cylinder rich mass is higher than with the nominal injector protrusion due to the higher fuel concentration above the step. This fuel is not efficiently oxidized, leading to higher soot content and longer combustion duration.

The equivalence ratio distribution was reported in **Figure 4–24** to highlights the flame evolution by varying the injector protrusion, for the three crank angle degrees shown in **Figure 4–22**. Specifically, the equivalence ratio contour plot was analyzed for a vertical plane cutting the cylinder axis and spray axis, while the isoline at 1500K (black line) was chosen as representative of the flame front. At TDC (**Figure 4–24** – a), for the -2 injector protrusion the flame mainly propagates toward the piston center and the available oxygen in this region increases the air entrainment. Decreasing the injector protrusion, a higher flame redistribution above the step can be observed, thus leading to a higher air utilization in the squish region. Therefore, at this stage, similar air utilization is obtained by the propagation of the flame toward the cylinder center or the squish region, thus confirming the similar trend highlighted in **Figure 4–23** – a. At +5 CAD aTDC (**Figure 4–24** – b), the -2 and -1 injector protrusions lead to reduced air utilization in the squish region. In addition, the flame recirculation toward the cylinder center interacts with the spray core increasing the cylinder rich mass. The nominal injector protrusion provides a balanced fuel split on the step, maximizing the air utilization both within the bowl and above the step. Also, the interaction between the flame recirculation and the spray core is avoided. With the +1 injector protrusion, the flame is pushed above the step where a higher air utilization is shown, simultaneously reducing the oxidation within the bowl with respect to the nominal protrusion. Close to the EOI, at +15 CAD aTDC (**Figure 4–24** – c), the -2 and -1 injector protrusions show a strong increment of the rich mass within the bowl than with nominal protrusion, thus leading to higher soot formation within the bowl and not using the available oxygen in the squish region.

Decreasing the injector protrusion, the flame is mainly directed above the step toward the cylinder head where the lower available oxygen results in higher soot formation.

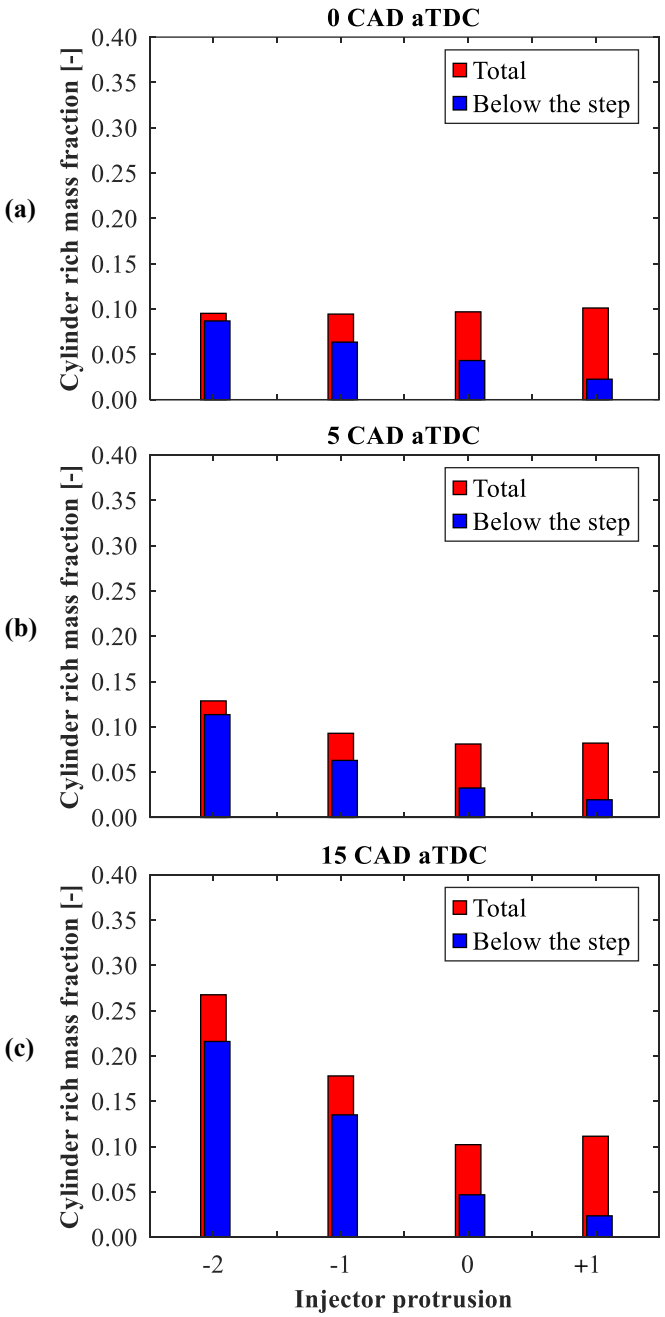

Figure 4–23: Cylinder rich mass fraction (equivalence ratio higher than 1.5) for the whole combustion chamber (Total) and below the horizontal plane cutting the step at TDC (Below the step). WP3: 4000 RPM x 18.5 bar BMEP.

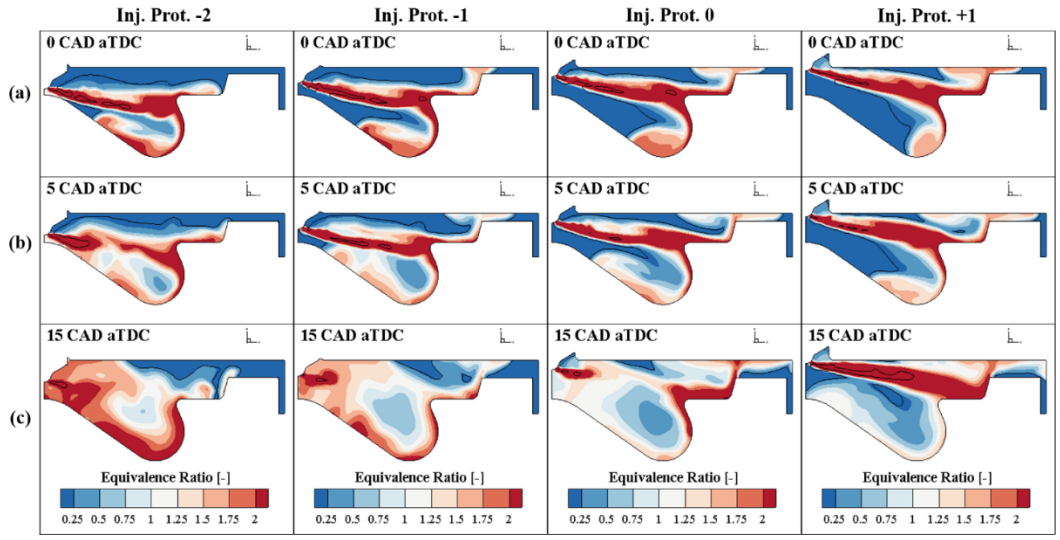

Figure 4–24: Equivalence Ratio contour plot on the selected vertical plane, for each injector protrusion under investigation with nominal SR. Black line: isoline at constant temperature equal to 1500K. WP3: 4000 RPM x 18.5 bar BMEP.

To further assess the effect of different SR on the combustion process, the equivalence ratio distribution for the nominal injector protrusion at +15 CAD aTDC was reported in **Figure 4–25**. The total cylinder mass was binned by equivalence ratio into twenty intervals for both the baseline and the reduced SR. The nominal SR highlights the mode of the distribution near to the stoichiometric range, reducing the cylinder mass fraction in the tails of the distribution. Therefore, the distribution for the baseline SR suggests a faster combustion process and lower soot formation due to the reduced cylinder mass fraction in the high equivalence ratio range. Specifically, the red dashed line of **Figure 4–25** is for the equivalence ratio equal to 1.5 and it is the same value adopted as tracer for the cylinder rich mass in the **Eq. 4–1**. Therefore, the higher is the cylinder mass fraction above this threshold the higher is soot formation, as observed for the reduced SR in **Figure 4–20**.

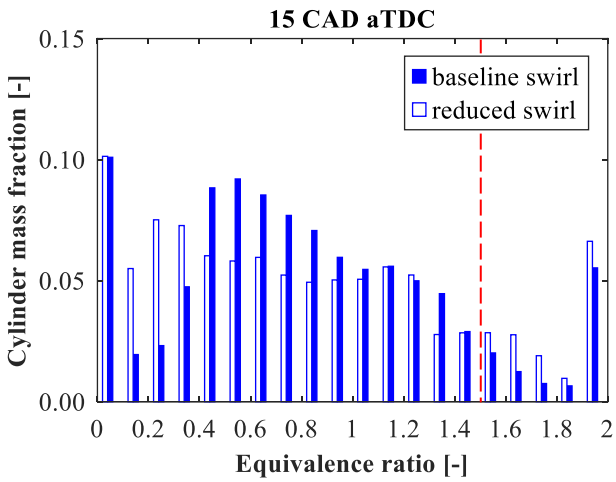

Figure 4–25: Equivalence Ratio bins distribution for the nominal injector protrusion at +15 CAD aTDC. WP3: 4000 RPM x 18.5 bar BMEP.

The spray targeting analysis was also carried out at partial load (WP1), as shown in **Figure 4–26**. Similar results can be observed, highlighting the best soot and BSFC at the nominal injector protrusion. Specifically, 70% soot reduction and a slight BSFC improvement (less than 1%) can be observed with respect to the re-entrant bowl.

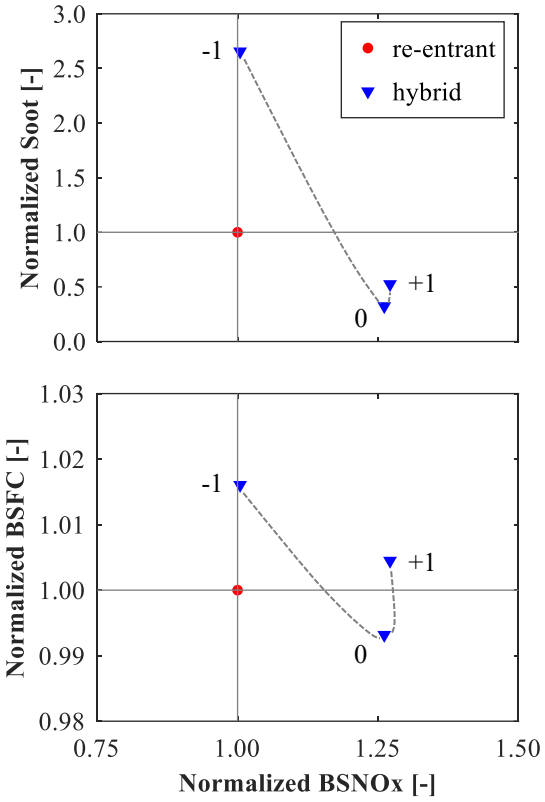

Figure 4–26: Injector protrusion sensitivity for the nominal swirl ratio: normalized trade-offs with respect to the baseline configuration. Top: Soot-BSNOx trade-off; bottom: BSFC-BSNOx trade-off. WP1: 1500 RPM x 5.0 bar BMEP.

4.3 Optical engine analysis

In this chapter, the 3D-CFD results were compared with the experimental data coming from an optical access engine that is based on the same engine architecture. The CIV and OH* chemiluminescence techniques were used to assess the flame evolution. Then, the 2-color pyrometry optical soot density (KL) was compared with the numerical soot distribution. For this scope, two numerical indices were defined: one is based on the soot volume fraction, while the other provides the optical soot density KL in the 3D-CFD environment. The description of the numerical methodologies was reported in the previous chapter '2.4 Optical engine analysis'. It is worth noting that just a qualitative comparison between the numerical and the experimental results was carried out. Indeed, on one side,

different engine operating conditions were compared (i.e., 3D-CFD: 1500 RPM x 4.6 bar IMEP, experimental: 1250 RPM x 4.5 bar IMEP). On the other side, the intrinsic differences in terms of engine layout (i.e., metal engine vs optical engine) can affect the comparison. Specifically, the piston used for the optical access engine had a reduced heat transfer due to the quartz features (lower heat conductivity and higher mechanical deformation). Then, the higher blow-by typical of the optical engine is not modeled in the 3D-CFD environment. Nevertheless, the comparison between the numerical and experimental results was considered a fundamental step to assess the predictive capabilities of the numerical methodology and to verify if the observed phenomena can be extended to the metal engine operating conditions.

4.3.1 Heat Release Rate

The numerical and experimental results were compared in terms of heat release rate, as shown in **Figure 4–27**. The same IMEP was reached both for simulations and experiments by using a similar injection strategy. Considering the numerical results of **Figure 4–27** – left, similar combustion of the first pilot injection is highlighted for both the piston bowls. Going near the TDC, the combustion of the second pilot and main injections provides a reduced HRR for the hybrid bowl. At this stage, the hybrid bowl highlights a reduced swirling flow that slightly affects the spray development, increasing the flame-to-wall interaction and thus reducing the combustion rate. A comparable behavior is observed for the experimental HRR of **Figure 4–27** – right, confirming the predictiveness of the numerical model. After the EOI of main event, the hybrid bowl promotes a higher HRR than with the re-entrant bowl. Indeed, the radial bumps mitigate the flame-to-flame interaction and enhance the mixing process, driving the flame toward the cylinder center. Also in this case, a qualitative good agreement is observed with respect to the experimental data, capturing the timing when this phenomenon occurs. Nevertheless, the experimental data show a reduced difference between the piston bowls under investigation. As already mentioned, this result was expected considering the different layout (metal engine vs optical engine) and the different operating conditions. After the EOI of post event, the re-entrant bowl shows a higher HRR with respect to the hybrid bowl due to the higher swirl ratio that increases the combustion rate of the residual fuel, as also confirmed by the experimental HRR of **Figure 4–27** – right.

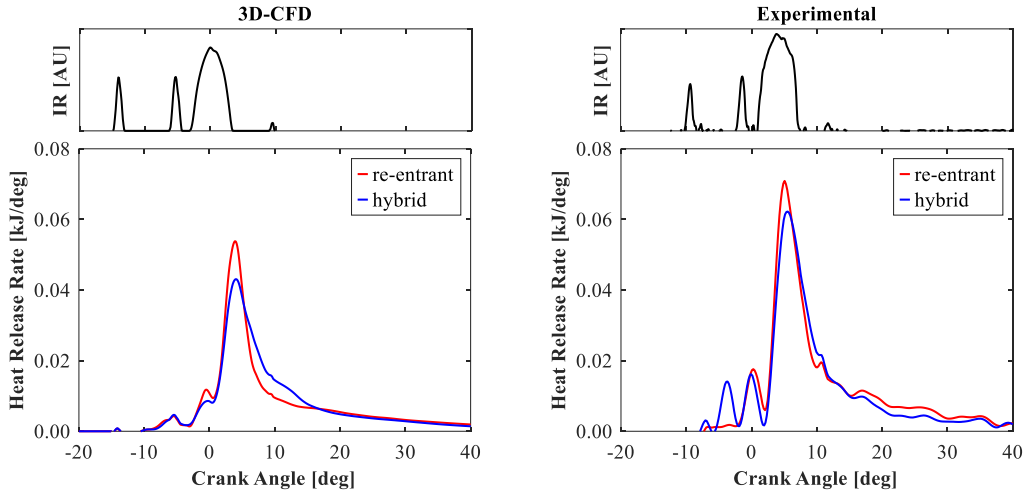

Figure 4–27: Injection rate profile and Heat Release Rate. Left: 3D-CFD. Engine operating condition: 1500 RPM x 4.6 bar IMEP; right: experimental. Engine operating condition: 1250 RPM x 4.5 bar IMEP.

4.3.2 CIV

The velocity field during the combustion process was investigated by comparing the CIV-resolved velocity field with the 3D-CFD results. With this aim, a single sector of the full cylinder geometry was considered, neglecting the squish region to avoid any light distortions induced by the high-curvature geometry. To compare the experimental and the numerical flow fields, the 3D-CFD velocity field was averaged along the cylinder axis, following the methodology described in the previous chapter '2.4.1 Combustion Image velocimetry (CIV)'. **Figure 4–28** shows the velocity field results during the injection event, at +3 CAD aEOI of main event. At this stage, the numerical results show a good correlation with the CIV data for both the piston bowls under investigation. More in detail, near the bowl periphery the flame propagates towards the bowl center, in the reverse flow and both the piston bowls show a high-magnitude velocity in this zone. However, the radial bumps for the hybrid bowl promote a faster reverse flow as outlined by the high-magnitude velocity vectors closer to the piston center (see **Figure 4–28** – right).

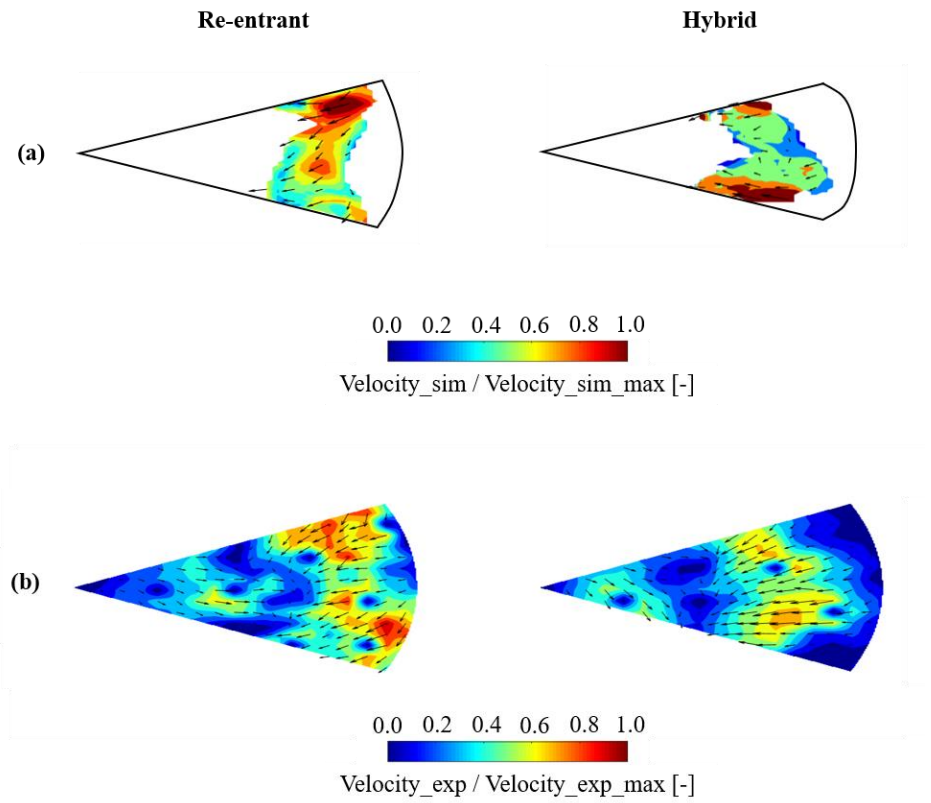

Figure 4–28: 3D-CFD z-average velocity (a) and experimental CIV-resolved velocity flow field (b) at +3 CAD aEOI of main event. Left: re-entrant; right: hybrid.

Figure 4–29 shows the velocity field results after the EOI of post injection, at +25 CAD aTDC. The numerical and experimental flow fields show a fairly good agreement, considering the total cylinder volume as path for the averaging computation; in this case the flow field is not influenced by any injection event. At this stage, the velocity field for the re-entrant bowl is swirl supported. Instead, for the hybrid bowl the velocity vectors are mainly directed towards the bowl periphery due to the more intense tumbling vortex that leads the flame outward above the step. This behavior is observed for both the numerical and experimental results, confirming that the numerical method can qualitatively reproduce the experimental flow field and this is crucial for a good prediction of soot oxidation in the late cycle.

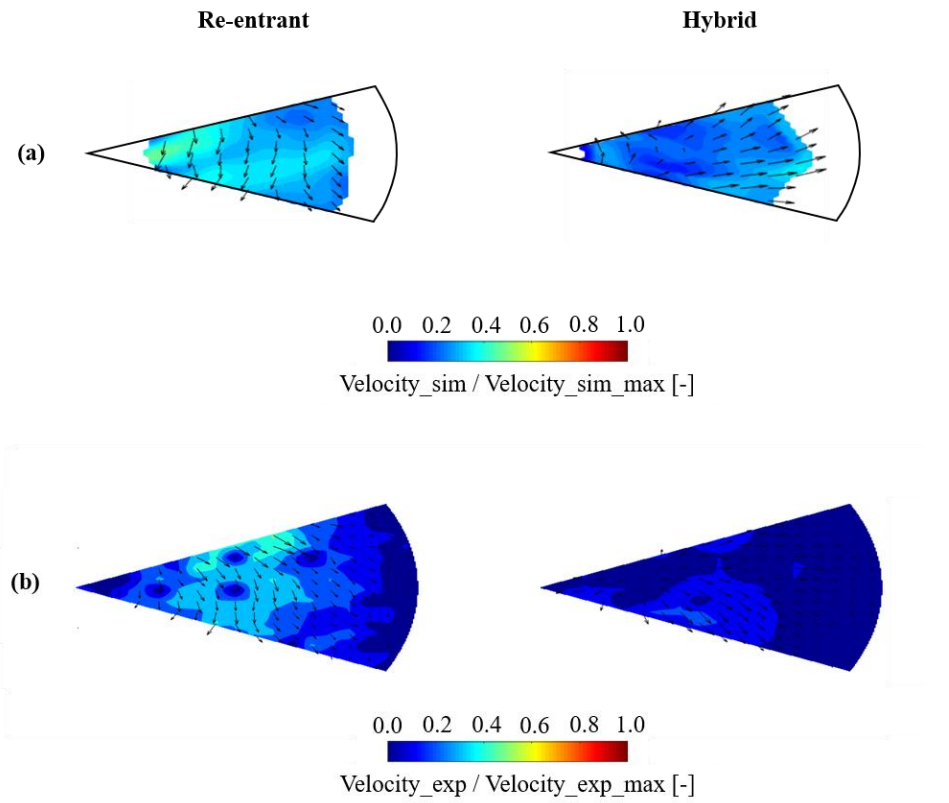

Figure 4–29: 3D-CFD z-average velocity (a) and experimental CIV-resolved velocity flow field (b) at +25 CAD aTDC – Late oxidation phase. Left: re-entrant; right: hybrid.

To further understand the piston bowl effect on the velocity field, a time-/spatial-resolved velocity magnitude map was designed. Particularly, the piston bowl was divided in angular sectors and the velocity in each sector was averaged. Thanks to this procedure, a 2D contour-map was defined as reported in **Figure 4–30**, where the temporal evolution of the velocity as a function of the sector location is shown for both simulations and experiments. On the y-axis, the azimuthal coordinate of the bowl sector is shown: 0 and 45 represent the axes of two consecutive radial bumps. For the numerical maps of **Figure 4–30** – a, to avoid the spray core effect on the flow field, the velocity in each sector was averaged considering only the computational cells with a temperature higher than 1500K, thus considering only the burned gas. Regarding the numerical results, both the piston bowls show a high-magnitude velocity zone close to the main EOI. However, the re-entrant bowl highlights a higher velocity magnitude in this region with respect to the hybrid bowl. Indeed, for the hybrid bowl part of the kinetic

energy is redistributed above the step due to the fuel split, thus reducing the velocity magnitude within the bowl. The same behavior can be observed for the experimental 2D-maps of **Figure 4–30** – b. Going ahead in the combustion process, the velocity magnitude is reduced especially for the hybrid bowl and different velocity distributions are highlighted. In particular, the higher swirling flow for the re-entrant bowl drives a directional motion from 0 to 45 sector angle as observed in **Figure 4–30** – left. Considering the hybrid bowl results of **Figure 4–30** – right, the peak of the velocity magnitude is lower than with the re-entrant design. Moreover, the high-magnitude zones are placed near 0 and 45 sector angles, at the radial bumps axes. Contrarily, the map center that refers to the center of the bowl shows a lower velocity magnitude. This behavior is due to the flame propagation toward the cylinder center that is mainly driven by the radial bumps, where a higher velocity magnitude is present. From +8 CAD aEOI of main event, the re-entrant bowl promotes a more intense velocity magnitude with respect to the hybrid bowl both for the numerical and experimental maps, due to the higher swirl vortex in the late cycle.

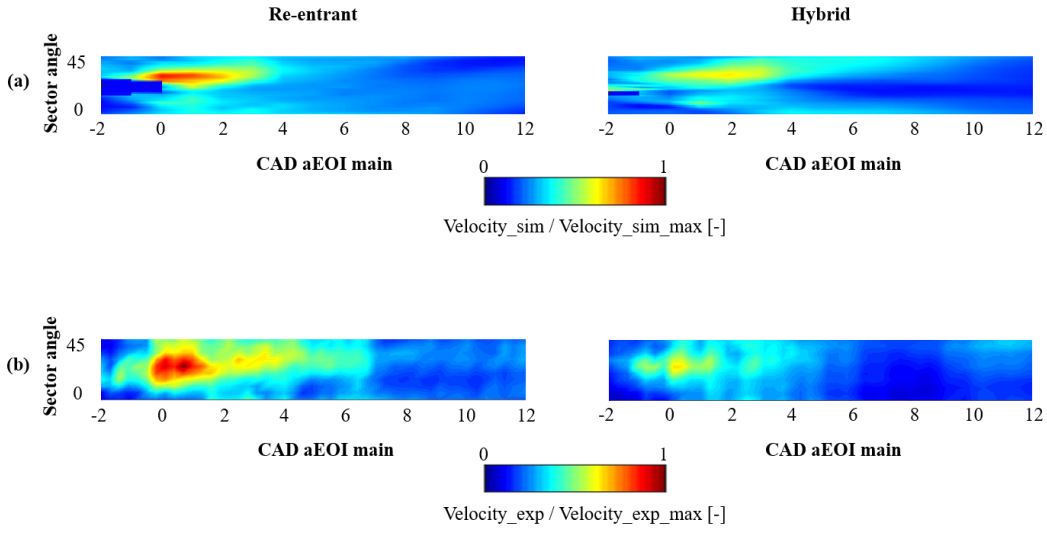

Figure 4–30: Average velocity evolution for each sector angle. (a) 3D-CFD; (b) experimental CIV-resolved.

4.3.3 OH* chemiluminescence

The evolution of the numerical OH radicals was compared with the experimental OH* chemiluminescence data to characterize the combustion in the near-stoichiometric high temperature flame front. **Figure 4–31** shows the numerical OH mass evolution for each piston bowls under investigation. Until the EOI of main event, when the OH is mainly placed around the spray core, the piston designs show comparable OH mass. Going near the SOI of post event, the hybrid bowl promotes a faster oxidation process, as confirmed by the higher peak of OH mass. Indeed, the radial bumps drive the flame toward the cylinder center, increasing the air/fuel mixing. Also, the higher air utilization above the step increases the OH content in the squish region. After the EOI of post event, the hybrid bowl highlights a lower OH mass than with the re-entrant bowl due to the higher oxidation rate that promotes a faster burn-out of the residual fuel.

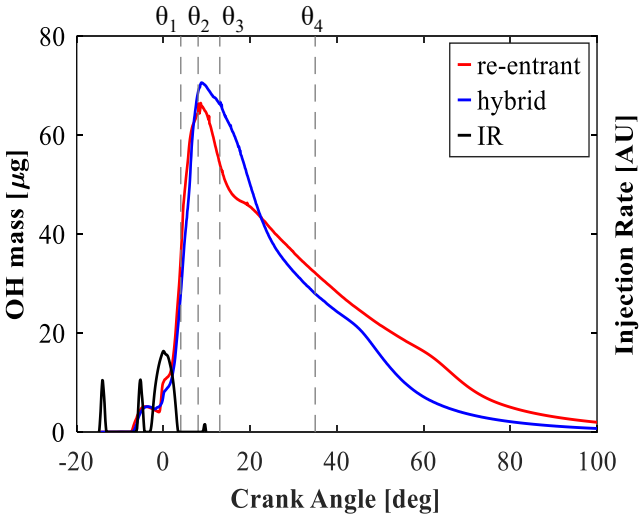

Figure 4–31: Numerical OH mass evolution and injection rate profile. Engine operating condition: 1500 RPM x 4.6 bar IMEP.

The 2D distribution of the OH mass fraction (yOH) was investigated following the methodology described in the previous chapter '2.4.2 OH* chemiluminescence'. This methodology allows the comparison between the numerical data and the optical OH* chemiluminescence images. The numerical

and experimental OH planar distributions for the four crank angle degrees highlighted in **Figure 4–31**, are reported in **Figure 4–32** for the re-entrant bowl and in **Figure 4–33** for the hybrid bowl. It is worth mentioning that, since the numerical and experimental injection profiles are slightly different, the experimental OH images refer to the same CAD after the EOI of main event of the 3D-CFD results.

At θ_1 = +0 CAD aEOI of main event

The numerical results of **Figure 4–32** – a and **Figure 4–33** – a highlight a similar OH distribution for the two piston bowls. The high-magnitude OH is mainly placed in the region of the flame-to-wall interaction, but some differences are highlighted within the bowl and in the squish region. In particular, the re-entrant bowl shows a stronger flame-to-flame interaction, as suggested by the higher OH content in the collision area of two adjacent flames. Regarding the squish region, only the hybrid bowl shows a high OH content due to the fuel split on the step. Similar results can be observed for the optical results of **Figure 4–32** – b and **Figure 4–33** – b. Also in this case, the re-entrant bowl shows a higher OH content in the flame collision area. However, a different shape of the collision area is shown between simulations and experiments due to the different operating conditions. Also, for the re-entrant bowl, the experimental distribution shows a stronger flame propagation in the squish region than the numerical distribution. This is mainly due to the retarded injection for the experiments that increases the fuel split above the bowl rim. For the hybrid bowl, the numerical and experimental distributions are comparable: the flame-to-flame interaction is reduced, as confirmed by the lower OH content in the flame collision area and the flame propagates in the squish region due to the fuel split.

At θ_2 = +4 CAD aEOI of main event

The numerical distribution for the re-entrant bowl of **Figure 4–32** – a shows a significant flame-to-flame interaction. The collision area of two adjacent flames propagates toward the cylinder center, while in the squish region the flame moves toward the liner. Regarding the hybrid bowl results of **Figure 4–33** – a, the flame-to-flame interaction is reduced, and the shape of the collision area is different than with the re-entrant bowl. Indeed, the flames interact only on the step due to the absence of the radial bumps. Moreover, the fuel split on the step increases the air utilization in the squish region, improving the oxidation rate as confirmed by the higher OH mass of **Figure 4–31**. Considering the optical distribution for the re-

entrant bowl of **Figure 4–32** – b, the radiation within the bowl is significantly attenuated, as highlighted by the region within the red dashed line. This luminosity attenuation is due to the higher soot content near the wall surface where the flame-to-flame interaction occurs. The higher soot content can significantly increase the absorption of the OH radiation, as also reported in [45]. The light attenuation from soot is not computed in the 3D-CFD environment, thus leading to some discrepancies between simulations and experiments. Instead, the optical image for the hybrid bowl of **Figure 4–33** – b, shows a negligible luminosity mitigation since the radial bumps reduce the flame-to-flame interaction, limiting the soot formation near the wall surface. Therefore, the numerical and experimental data show a fairly good agreement.

At θ_3 = +8 CAD aEOI of main event

As highlighted in **Figure 4–31**, after the EOI of post event, the hybrid bowl leads to higher OH mass, suggesting a higher oxidation rate in the flame front. At this stage, the flame motion toward the cylinder center, in the reverse flow, guides the oxidation process. Considering the numerical results for the re-entrant bowl of **Figure 4–32** – a, the OH concentration is mainly located near the outer bowl rim and in the squish area. Instead, by looking at the numerical results for the hybrid bowl of **Figure 4–33** – a, two zones with high OH content are highlighted. On one side, an intense OH region is significantly advanced toward the piston center due to the radial bumps. On the other side, the flame propagates above the step where a higher OH content is observed. The more intense OH zones toward the piston center and above the step suggest a higher combustion rate for the hybrid bowl. The numerical results show a good agreement with the experimental images of **Figure 4–32** – b and **Figure 4–33** – b. In particular, the experimental luminosity due to the OH tracing is again visible for the re-entrant bowl, due to the reduced soot content [45]. For the hybrid design, similar to the numerical results, a high OH content is located toward the piston center and above the step.

At θ_4 = +31 CAD aEOI of main event

Late in the cycle, the re-entrant bowl shows higher OH mass with respect to the hybrid bowl (see **Figure 4–31**) due to the slower oxidation of the residual fuel. Comparing **Figure 4–32** – a and **Figure 4–33** – a, the re-entrant bowl shows higher OH content than with the hybrid bowl and it is mainly placed in the bowl center, where the swirling flow mainly contributes to the oxidation rate. Contrarily, the hybrid bowl leads to a remarkable OH mitigation close to the bowl

center. A qualitative agreement with the optical data of **Figure 4–32** – b and **Figure 4–33** – b can be observed. In this case, the hybrid bowl promotes a stronger OH mitigation with respect to the numerical results. This may be related to a faster oxidation rate for the hybrid bowl in the experiments, as highlighted by the comparison between the numerical (**Figure 4–27** – left) and the experimental (**Figure 4–27** – right) HRR in the late cycle.

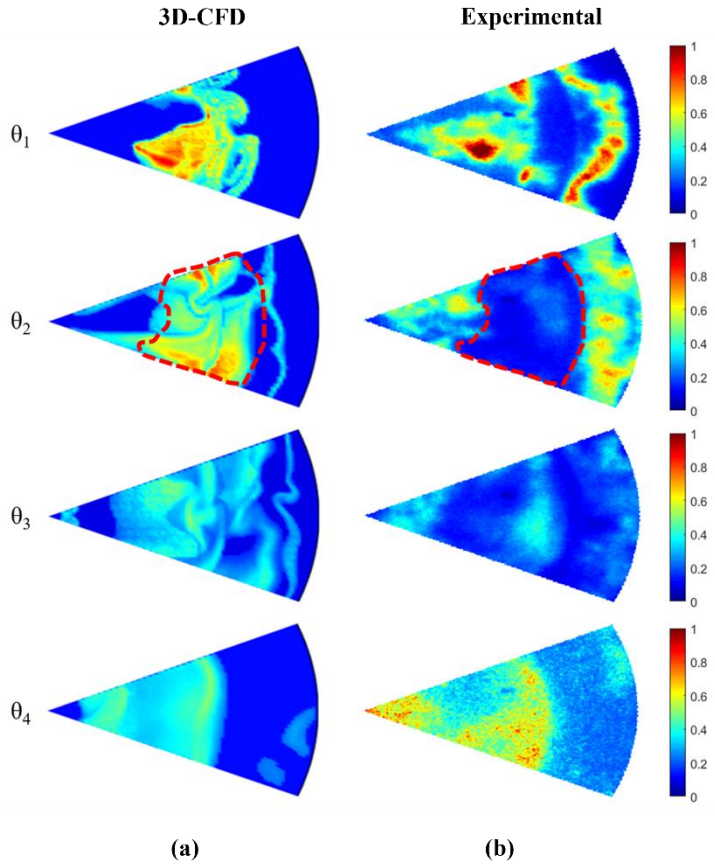

Figure 4–32: Re-entrant bowl results. (a) 3D-CFD OH mass fraction averaged along the cylinder axis. Engine operating condition: 1500 RPM x 4.6 bar IMEP; (b) Experimental OH* chemiluminescence images. Engine operating condition: 1250 RPM x 4.5 bar IMEP.

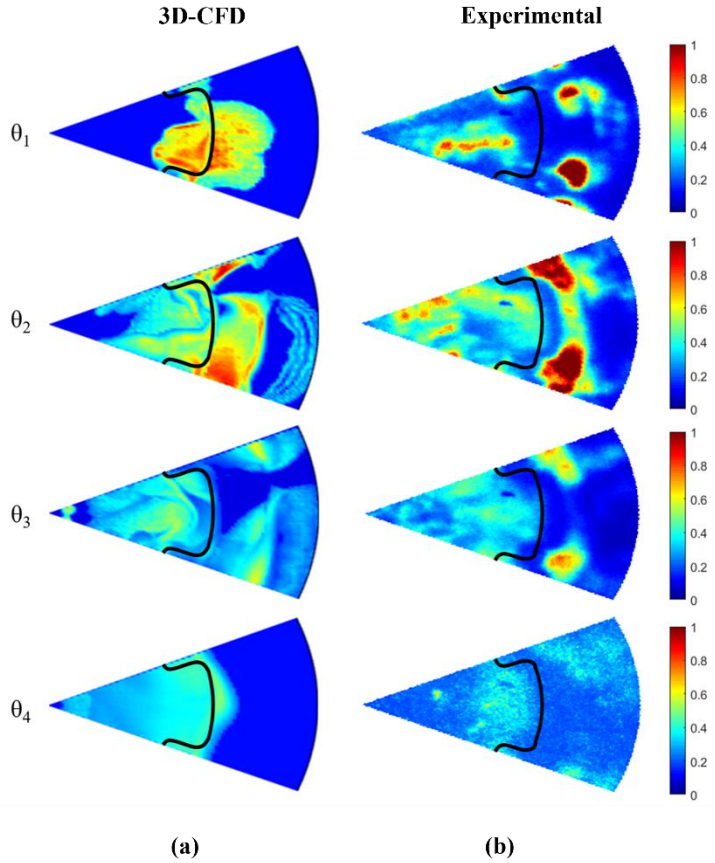

Figure 4–33: Hybrid bowl results. (a) 3D-CFD OH mass fraction averaged along the cylinder axis. Engine operating condition: 1500 RPM x 4.6 bar IMEP; (b) Experimental OH* chemiluminescence images. Engine operating condition: 1250 RPM x 4.5 bar IMEP.

4.3.4 Optical soot density (KL)

Once assessed the combustion by means of the CIV and OH* chemiluminescence techniques, the soot analysis was carried out, considering the numerical methodologies described in the previous chapter '2.4.3 Optical soot density (KL)'. The numerical soot distributions were compared with the optical soot density KL from the 2-colour pyrometry technique. With this aim, the analysis was focused only on a specific area of the bowl, as shown by the green area of **Figure 4–34** – right. The center of the bowl was neglected to avoid light reflections and distortions, while the squish zone was excluded due to the difficulty of isolating the impact of the bumps in this zone. The same region of interest was considered in the 3D-CFD analysis, as shown in **Figure 4–34** – left.

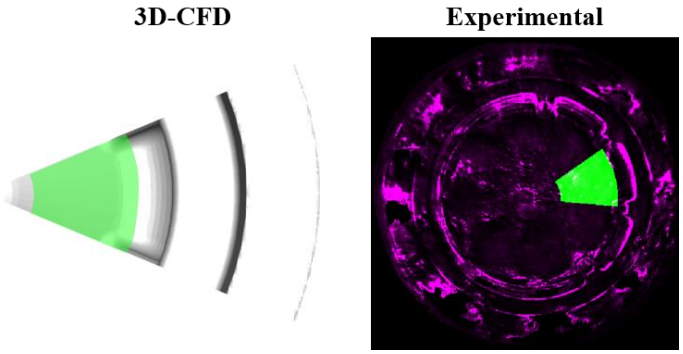

Figure 4–34: Numerical and experimental investigation area.

To provide a global index of the soot evolution, the average KL over the selected region was evaluated both in the numerical and experimental environments. With this aim, the total amount of cells/pixels (A_a) for the numerical/experimental images was computed following the **Eq. 4–2**:

$$A_a = \sum_{i=cells,a} i \qquad \text{Eq. 4–2}$$

The sum of KL over the cells/pixels of the selected region provided the cumulative KL ($KL_{cumul,a}$) following the **Eq. 4–3**:

$$KL_{cumul,a} = \sum_{i=cells,a} KL_i \qquad \text{Eq. 4–3}$$

Then, the global average KL over the selected region (KL_{mean}) was defined by the **Eq. 4–4**:

$$KL_{cumul,a} = \sum_{i=cells,a} KL_i \qquad \text{Eq. 4–4}$$

It is worth noting that only a qualitative comparison between the numerical and experimental results was performed, by looking to the normalized results. Indeed, a different magnitude of the KL was expected due to the intrinsic differences in terms of engine layout (i.e., metal engine vs optical engine) and the

different technique adopted for the KL evaluation (i.e., numerical methodology vs 2-colour pyrometry). However, the qualitative comparison between simulations and experiments, each of them normalized to its maximum value, was considered as crucial step to identify the piston bowl behavior in terms of soot formation/oxidation processes. **Figure 4–35** shows the normalized KL_{mean} over the selected region for each investigated piston bowl. Focusing on the numerical results of **Figure 4–35** – left, the two piston designs show a similar soot formation rate until +20 CAD aTDC. Then, the hybrid bowl leads to lower peak of KL than with the re-entrant bowl. Going ahead in the cycle, the hybrid bowl promotes a strong KL attenuation, suggesting a significant impact of the hybrid bowl geometry on soot oxidation rate. Regarding the experimental results of **Figure 4–35** – right, a qualitative agreement with simulations is observed. Also in the experimental tests, the hybrid bowl shows a strong improvement of the soot oxidation in the late cycle, leading to a strong KL reduction. Nevertheless, the time involved by the soot evolution is significantly reduced with respect to the simulations. This could be related to the intrinsic differences between the metal and the optical engines. Below a certain temperature and soot concentration the CCD camera cannot detect any signal, thus leading to faster KL attenuation in the experimental layout. Also, the soot PM model was validated against the experimental engine-out soot emissions from the 4-cylinder metal engine [48]. Therefore, the entire soot evolution (soot formation/oxidation rates) was not calibrated. However, the qualitative good agreement confirms the predictiveness of the numerical methodology and the beneficial effects of radial bumps on the soot evolution.

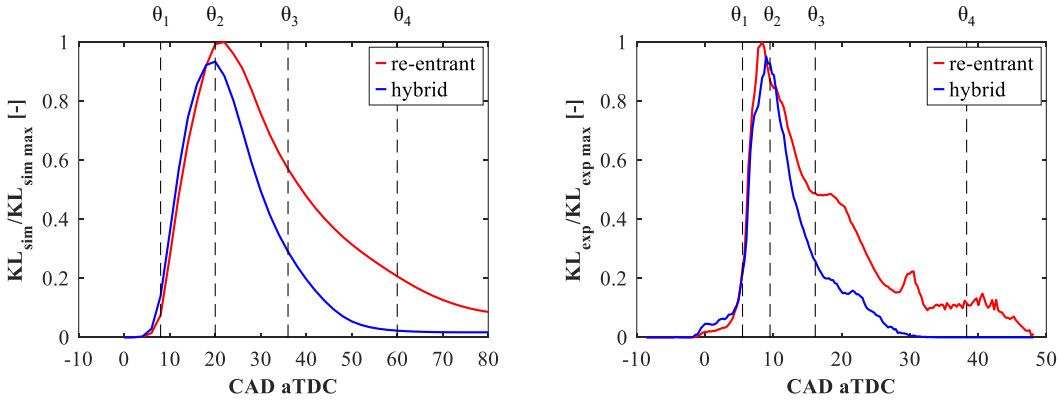

Figure 4–35: Normalized KL_{mean} over the defined region. Left: 3D-CFD. Engine operating condition: 1500 RPM x 4.6 bar IMEP; right: experimental. Engine operating condition: 1250 RPM x 4.5 bar IMEP.

To further understand the potential of the developed numerical methodology, the 2D distributions of the numerical f_vL and KL factors were compared with the optical soot density KL. The re-entrant bowl (**Figure 4–36**) and hybrid bowl (**Figure 4–37**) results are reported for the four crank angle degrees highlighted in **Figure 4–35**. Specifically, the numerical f_vL and KL (normalized with respect to its maximum value) are reported in the first and second columns, while the normalized experimental KL is in the third column.

At θ_1 – initial soot formation phase

Similar results are highlighted for the numerical f_vL and KL factors. This is due to the reduced soot content (high soot transmissivity) that introduces a negligible light attenuation in the radiation transfer process over the optical path length. Therefore, the f_vL can be considered as a proper index for the comparison with the optical soot density KL, although it is based on a simplified approach. By comparing the numerical distributions with the optical soot density KL, a qualitative good agreement is observed. Specifically, a high magnitude region is in the piston bowl rim where the flame-to-wall interaction appears. It is worth mentioning that the edges of the bowl provide a light distortion, thus leading to false KL values for the experimental 2-colour pyrometry. Therefore, the comparison with simulations should be done only far enough from the piston wall. Regarding the comparison between the re-entrant and the hybrid bowls, similar results can be observed as also confirmed by the global average KL of **Figure 4–35**.

At θ_2 – soot peak

At this stage, which corresponds to the maximum of KL on **Figure 4–35**, the two numerical methodologies provide similar results. In particular, the re-entrant bowl results of **Figure 4–36** highlights the high magnitude soot close to the bowl surface, both for simulations and experiments. Considering the hybrid bowl results of **Figure 4–37**, the radial bumps reduce the flame-to-flame interaction and consequently the soot intensity in the collision area. Moreover, the high magnitude soot is driven by bumps toward the piston center, where the high oxygen concentration enhances the soot oxidation rate. The optical analysis provides similar results, but in this case a region with a high KL value is observed

above the step, since the retarded injection promotes a different fuel split in the experiments.

At θ_3 – soot oxidation phase

Going ahead on soot oxidation, both the simulations and the experiments show significant soot attenuation. For the re-entrant bowl of **Figure 4–36**, both the numerical indices and the optical data highlight a homogeneous soot distribution within the bowl, while only the optical KL shows a still significant soot content above the step. For the hybrid bowl of **Figure 4–37**, a strong soot reduction toward the piston center is shown and the resulting global intensity of soot is lower than with the re-entrant bowl, as also confirmed in **Figure 4–35**. Even for this piston design, the optical KL shows a higher soot value in the squish region with respect to simulations.

At θ_4 – late stage

During the late phase of the soot oxidation process, both the numerical and the optical results show remarkable soot attenuation, as also reported in **Figure 4–35**. However, the re-entrant bowl shows a higher soot with respect to the hybrid bowl that provides an almost zeroed KL within the bowl. By looking at the optical results, a high magnitude KL region is still shown in the squish region, differently from simulations.

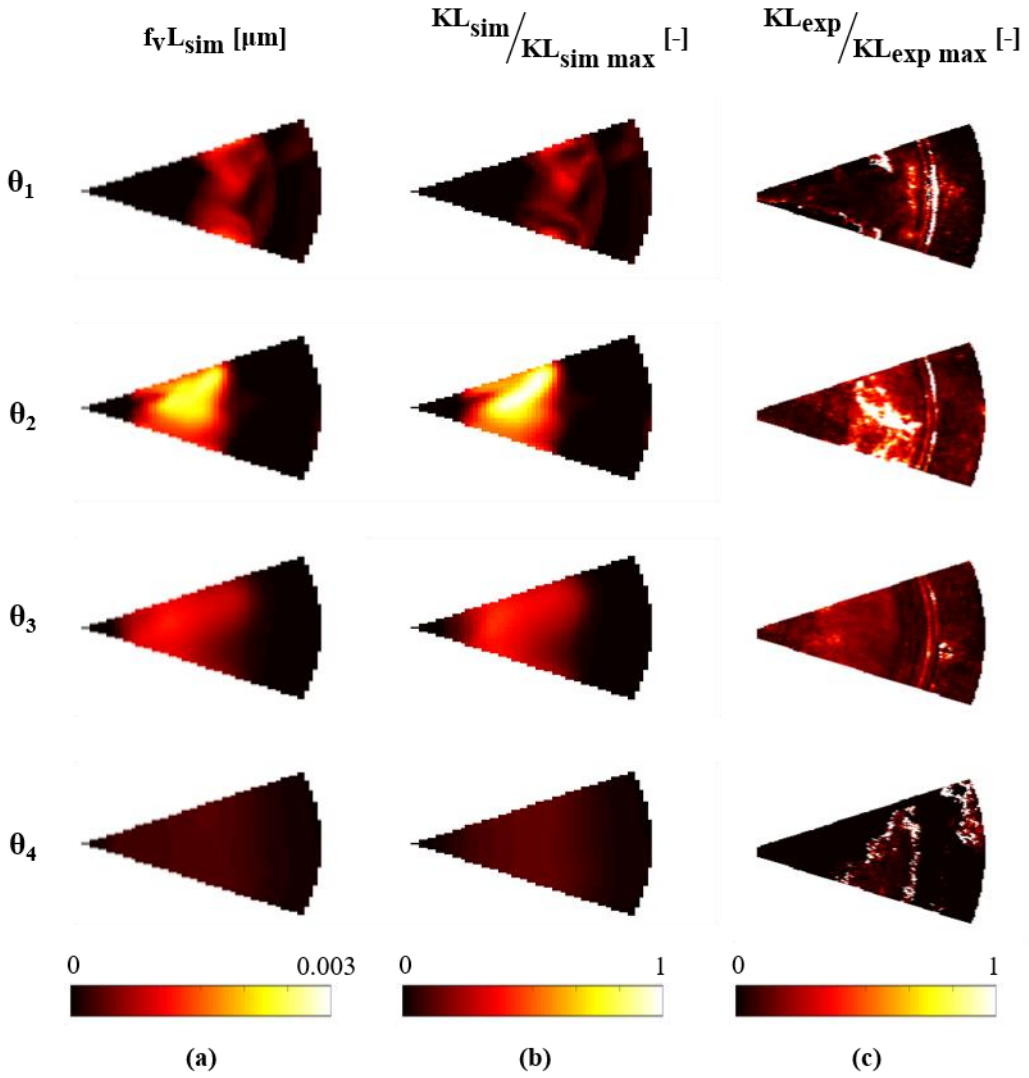

Figure 4–36: Re-entrant bowl results. 3D-CFD f_vL (a) and KL (b) normalized with respect to its maximum. Engine operating condition: 1500 RPM x 4.6 bar IMEP; (c) experimental KL normalized with respect to its maximum. Engine operating condition: 1250 RPM x 4.5 bar IMEP.

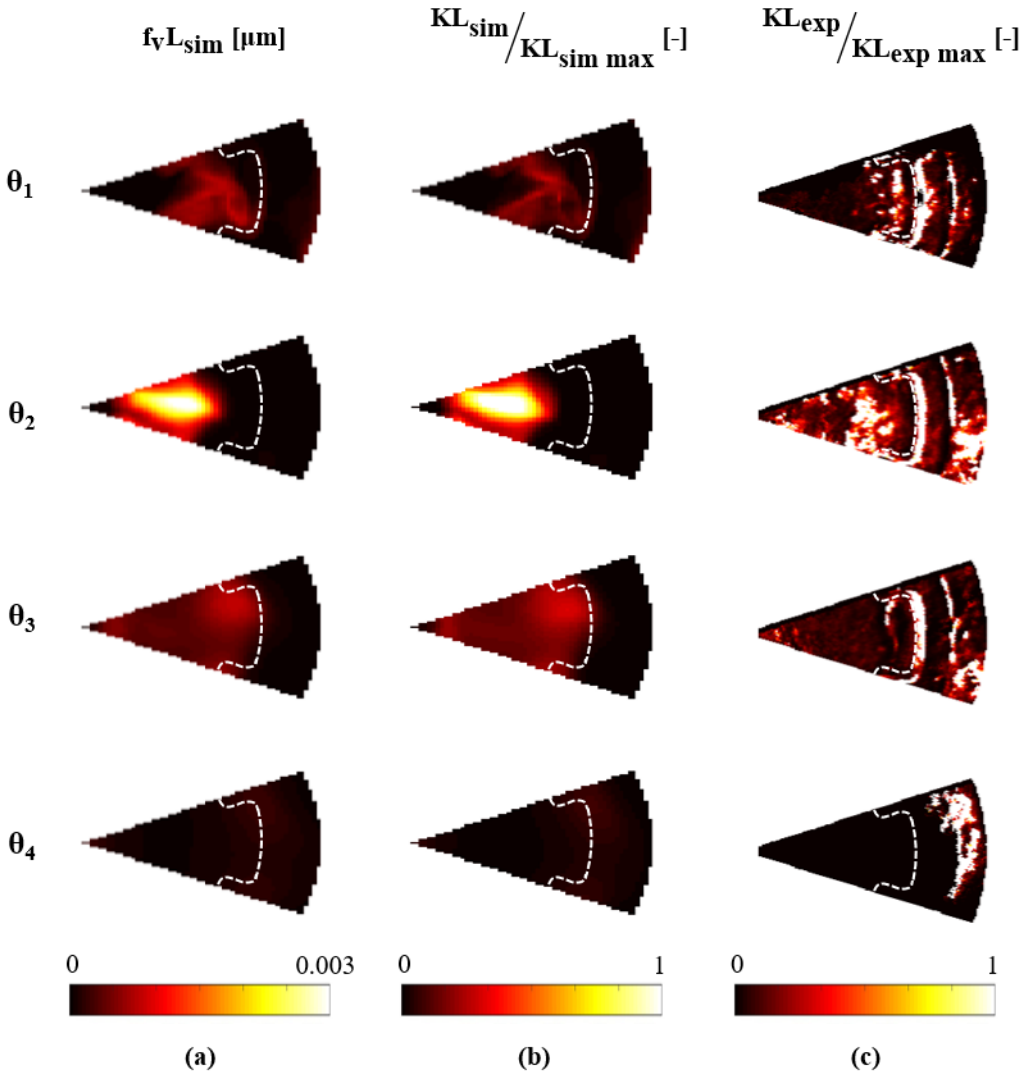

Figure 4–37: Hybrid bowl results. 3D-CFD f_vL (a) and KL (b) normalized with respect to its maximum. Engine operating condition: 1500 RPM x 4.6 bar IMEP; (c) experimental KL normalized with respect to its maximum. Engine operating condition: 1250 RPM x 4.5 bar IMEP.

To further assess the impact of the piston bowl on soot evolution, a time/spatial soot KL map was developed. For the experimental data, the optical area of interest was divided in 5°-wide angular sectors in the azimuthal direction (φ) as reported in **Figure 4–38** – right and the KL was averaged for each angular sector. Whit a similar approach, the numerical KL was averaged for each radial line, as shown in **Figure 4–38** – left. The resulting average KL was computed following the **Eq. 4–5**:

$$KL_{mean} = \frac{KL_{\ cumul,\varphi}}{A_{\varphi}} \qquad \text{Eq. 4–5}$$

where A_{φ} is the total amount of cells over the radial line/pixels in the angular sector, and the $KL_{cumul,\varphi}$ is the cumulative KL for each radial line/angular sector.

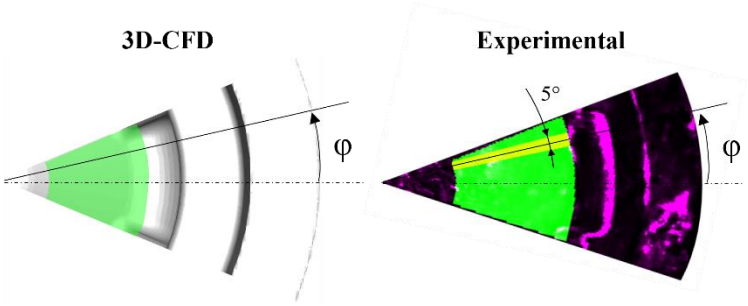

Figure 4–38: 3D-CFD radial lines (left) and experimental sector angles (right) used for the average computation.

Figure 4–39 shows the temporal evolution of the defined averaged KL as a function of the azimuthal direction, where the 0 and 40 represent the radial bumps. The numerical and experimental results were normalized with respect to the corresponding maximum. As previously reported, the numerical and experimental soot KL evolution involve different time intervals. Therefore, the KL evolutions of **Figure 4–39** were investigated considering two different time intervals, in which the soot evolution is similar, as reported in **Figure 4–39** – c.

Focusing on the numerical results for the re-entrant bowl of **Figure 4–39** – a, when the KL reaches its maximum, the KL map highlights the high magnitude

region all around the sector angles. Specifically, a significant KL intensity is observed in the sector periphery (0 and 40 sector angles), due to the flame-to-flame interaction that increases the soot formation. A similar result is shown also for the experimental map, but with different intensity. Going ahead in the cycle, both the numerical and experimental maps show a significant residual KL all over the sector domain. Considering the hybrid bowl of **Figure 4–39** – b, the numerical KL map shows a strong reduction of the intensity in the sector periphery due to the presence of the radial bumps. In addition, the radial bumps move the flame toward the sector center, where the high magnitude KL is shown. In this zone, late in the cycle, a more intense soot KL mitigation is observed with respect to the re-entrant bowl since the high oxygen content increases the soot oxidation rate. For the experimental map, comparable results are observed unless some differences. Specifically, a narrow high magnitude zone is still detectable in the sector angle 0, but it is strongly reduced in the late cycle in comparison with the re-entrant bowl.

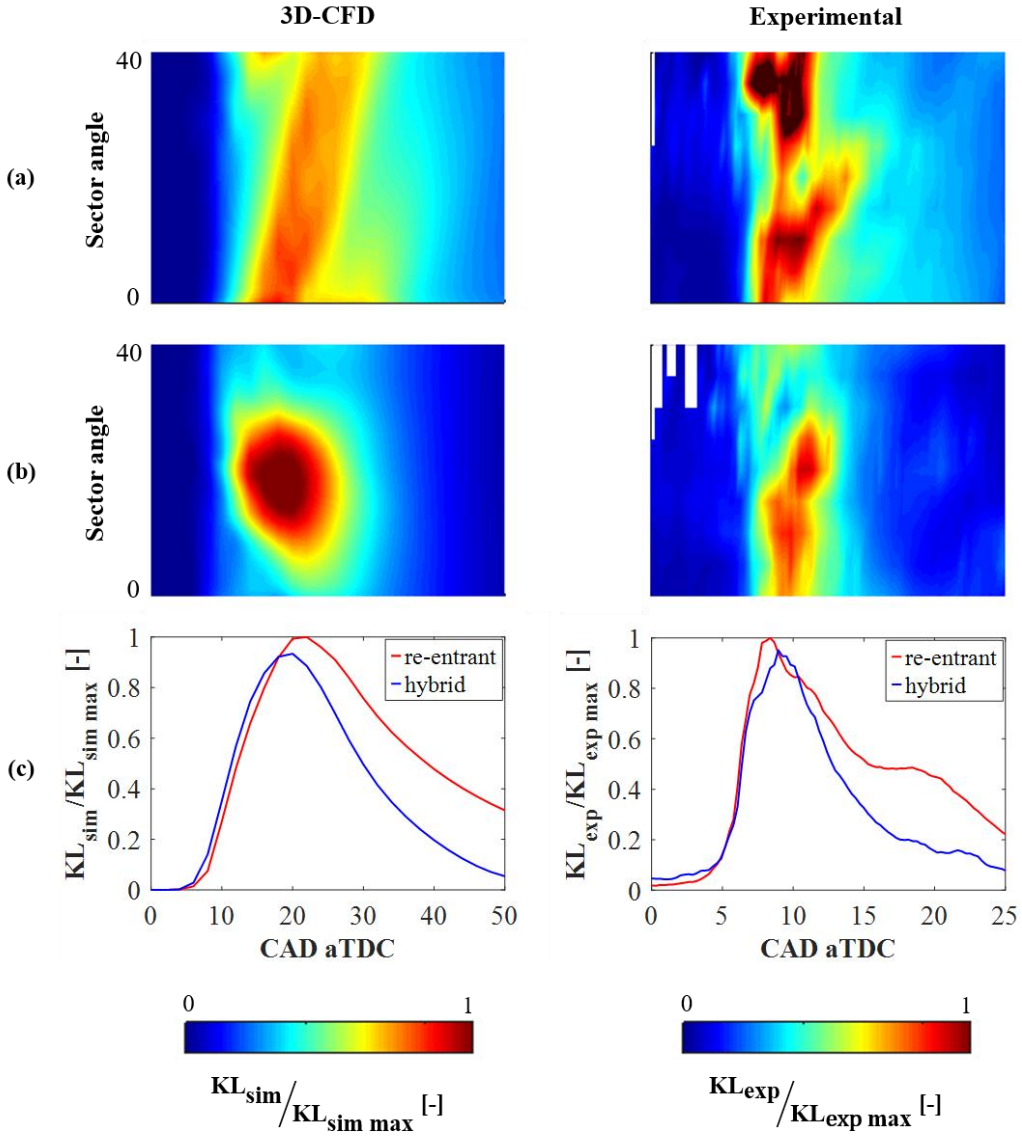

Figure 4–39: Numerical (left) and experimental (right) sector angle KL maps. (a) Re-entrant bowl; (b) hybrid bowl; (c) normalized KL_{mean}.

A similar methodology was developed to obtain a time/spatial evolution of the KL along the radial direction. For the scope, the optical region of interest was divided in rings with a thickness of 0.5 mm, as shown in **Figure 4–40** – right. The KL was averaged for each ring, providing an index of soot evolution along the radial direction (r). With a similar approach, the numerical KL was averaged for each arc as shown in **Figure 4–40** – left. The resulting average KL was defined by the **Eq. 4–6**:

$$KL_{mean} = \frac{KL_{\ cumul,r}}{A_r} \qquad \text{Eq. 4–6}$$

where A_r is the total amount of cells over the arc/pixels in the ring and the $KL_{cumul,r}$ is the cumulative KL for each arc/ring.

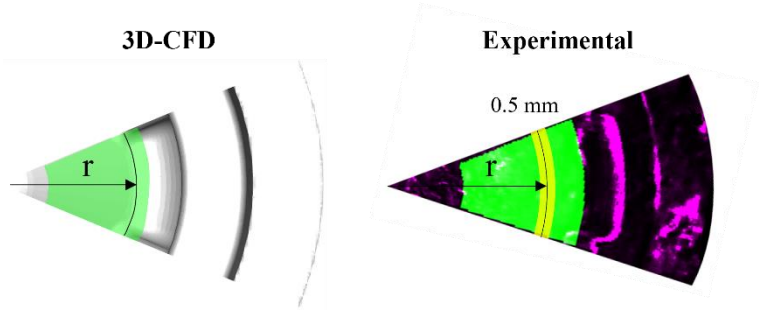

Figure 4–40: 3D-CFD arcs (left) and experimental rings (right) used for the average computation.

Figure 4–41 shows the temporal evolution of the normalized averaged KL as a function of the radius. Even in this case, the numerical and experimental maps were assessed considering two different time intervals that show comparable soot evolution, as reported in **Figure 4–41** – c.

Considering the numerical KL for the re-entrant bowl of **Figure 4–41** – a, a high magnitude zone starts to appear at the piston bowl surface (radius: 18 mm) due to the flame-to-wall interaction. Going ahead in the cycle, the flame goes toward the piston center and reaches the radius 6 mm at +30 CAD aTDC. Regarding the experimental map, a qualitative agreement is shown: a high

magnitude zone starts to appear at the piston bowl periphery and then it goes toward the piston center. Nevertheless, a higher KL attenuation is shown with respect to the numerical map, going toward the piston center. This could be related to the retarded injection for the experiments that results in different fuel split and thus different fuel content within the bowl. Focusing on the hybrid bowl results of **Figure 4–41** – b, the numerical map reports a strong reduction of KL close to the piston bowl surface, during the first stages of soot formation. Instead, the high magnitude KL is shifted toward the piston center (lower radius) due to the radial bumps that promotes a faster flame recirculation. Indeed, the flame reaches the 6 mm faster than the re-entrant bowl at +15 CAD aTDC. This results in higher soot oxidation rate, leading to a strong soot KL attenuation in the late cycle with respect to the re-entrant bowl. Even the experimental map shows a faster flame propagation toward the piston center for the hybrid bowl. However, some differences are highlighted in comparison with the numerical map. In particular, a higher intensity of KL is shown near the piston bowl periphery, while the zone close to the piston center shows a lower intensity. As already noted, this could be related to the different fuel split at the step that affects the soot distribution within the bowl.

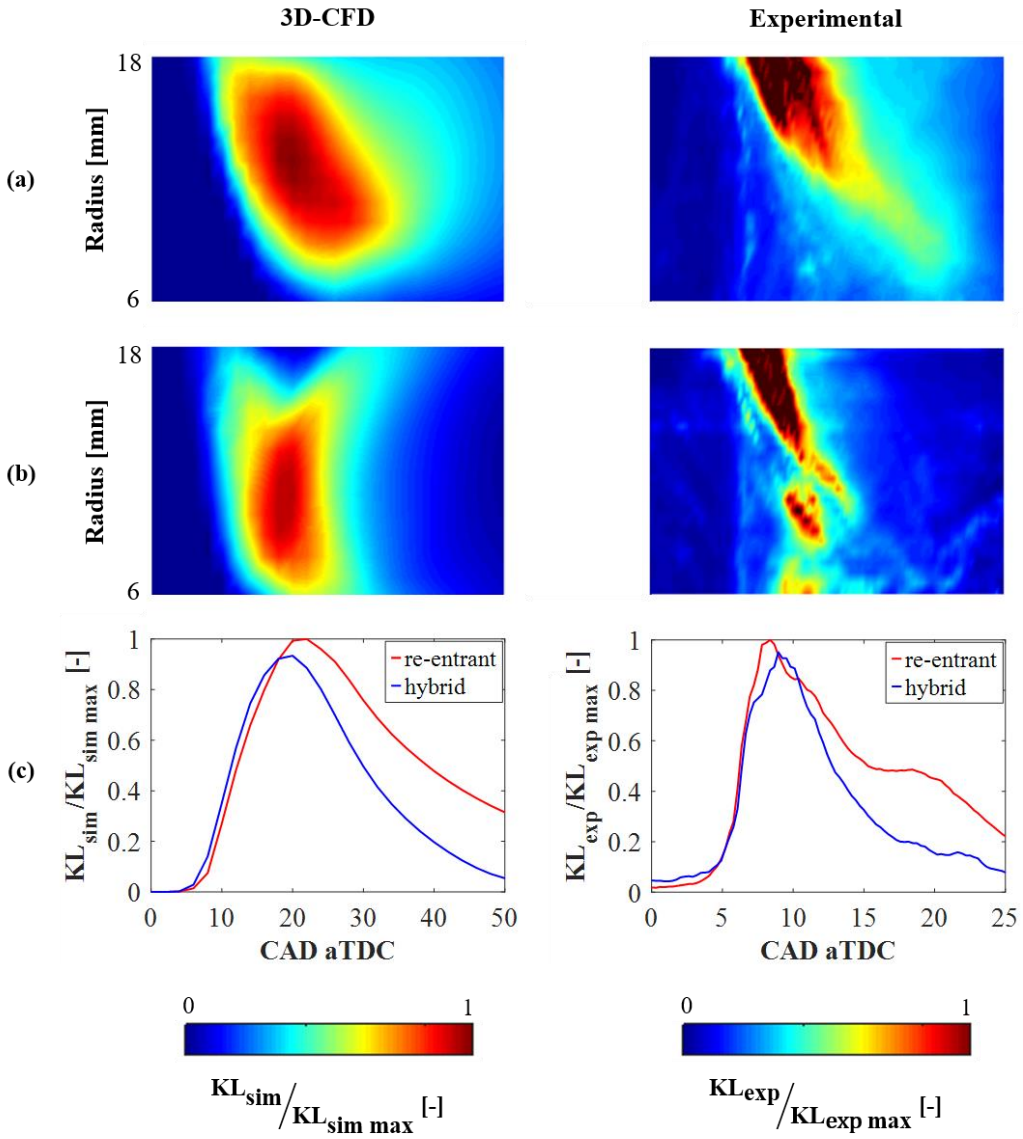

Figure 4–41: Numerical (left) and experimental (right) radius KL maps. (a) Re-entrant bowl; (b) hybrid bowl; (c) normalized KL_{mean}.

4.4 Single-cylinder engine analysis

In the framework of a collaboration between PUNCH Torino S.p.A/ formerly General Motors Global Propulsion Systems and CNR – STEMS, an experimental activity was carried with a SCE based on similar architecture and piston designs as the ones used in the numerical analysis. The results of the analysis were used to experimentally confirm the potential benefits provided by the innovative hybrid piston bowl.

The work described in this Chapter was previously published in the following publications:

- Belgiorno, G., Boscolo, A., Dileo, G., Numidi, F. et al., "Experimental Study of Additive-Manufacturing-Enabled Innovative Diesel Combustion Bowl Features for Achieving Ultra-Low Emissions and High Efficiency," SAE Int. J. Adv. & Curr. Prac. in Mobility 3(1):672-684, 2021, https://doi.org/10.4271/2020-37-0003.
- G. Di Blasio, R. Ianniello, C. Beatrice, F. C. Pesce, A. Vassallo, G. Belgiorno, "Experimental Investigation on an Innovative Additive Manufacturing Enabled Diesel Piston Design to Improve Engine-out Emissions and Thermal Efficiency beyond Euro6", THIESEL Conference 2020.

4.4.1 Experimental setup

The experimental activity was carried out for a 0.5 l/cyl SCE whose main features are listed in **Table 4–1**. It has a higher specific displacement than the engine used for the numerical analysis (i.e., 0.4 l/cyl). A fast-acting fuel injection system with a maximum rail pressure of 2500 bar and 7-hole solenoid injector were adopted. The SCE has a modular and variable design, to be flexible in the use of different engine configurations. This approach allowed the use of different piston designs. In particular, the baseline engine features a steel-forged re-entrant bowl, as shown in **Figure 4–42** – a. Then, an innovative piston was designed by means of a steel-based additive-manufacturing (AM) approach and the resulting prototype is reported in **Figure 4–42** – b. It has the same geometrical features of the hybrid design used for the numerical analysis (see **Figure 2–1** – d). Nevertheless, in this case a reduced number of radial bumps was used to match the number of nozzle hole (i.e., simulations: 8-hole vs experiments: 7-hole). The two investigated designs feature the same compression ratio and squish height.

Table 4–1: Single cylinder engine main features.

Specific displacement	0.5 l/cyl
Bore x Stroke	83.0 mm x 90.4 mm
Compression ratio	16:1
Valve #	4
Fuel injection system	Common rail Max Rail Pressure 2500 bar
Nozzle hole #	7

(a) **(b)**

Figure 4–42: (a) Conventional steel-forged re-entrant bowl; (b) hybrid bowl steel-based AM prototype. Adapted from [42].

The experimental activity was focused on the characterization of the novel combustion system in terms of both emissions and thermal efficiency. With this aim, four partial load engine working points were considered, as reported in **Table 4–2**. They cover the typical type-approval driving cycle (NEDC, WLTP) operating areas and are reference points for the efficiency and emissions estimation.

Table 4–2: Engine working points.

Speed [rpm]	BMEP [bar]
2000	2.0
1500	5.0
2000	8.0
1500	14.0

A preliminary sensitivity analysis on the injector tip protrusion was carried out by varying the washer thickness (WT) [42]. These tests were performed at fixed MFB50 and engine-out NOx (i.e., EU6b targets) by varying the SOI and the EGR rate, respectively. The resulting optimal WT was 1mm lower than the one adopted for the conventional re-entrant bowl (i.e., 2mm). Then, a further optimization of the injection pattern with the optimal WT was carried out by varying the number, dwell time and quantities of the pulses [42]. The results showed that only at the lowest engine load (i.e., 2000 RPM x 2.0 bar BMEP) an optimized injection pattern was necessary for soot reduction. Once determined the optimal injector tip protrusion and injection pattern, a design of experiment (DoE) approach was carried out for the optimization of MFB50 and rail pressure, keeping fixed NOx targets [43]. Finally, an EGR rate sweep was performed for the best calibration of each engine operating condition, assessing the soot-NOx trade-offs [43].

4.4.2 Results and discussion

The EGR rate sweep trade-offs for the working points 1500 RPM x 5.0 bar BMEP and 2000 RPM x 8.0 bar BMEP are reported in **Figure 4–43** – a and **Figure 4–43** – b, respectively. For both the working points, the optimal engine parameter calibration, which is based on the previous DoE in terms of MFB50 and rail pressure, was used as reference for the EGR rate sweep. The trade-offs refer to the indicated specific PM (ISPM) and NOx (ISNOx) emissions. The hybrid design shows a strong improvement of the trade-off for the two tested operating

conditions. At 1500 RPM x 5.0 bar BMEP of **Figure 4–43** – a, 75% ISPM reduction is reached with respect to the re-entrant bowl, keeping the ISNOx at the EU6b target of 0.6 g/kWh. This result is in line with the numerical trade-off of **Figure 4–17** at the same engine working point. The simulations highlighted at fixed BSNOx, a 70% soot reduction with respect the re-entrant bowl. Even at 2000 RPM x 8.0 bar BMEP of **Figure 4–43** – b, a significant ISPM reduction (-54%) is provided by the hybrid bowl, keeping the ISNOx at the EU6b target of 0.8 g/kWh. Again, the result is comparable with the numerical soot reduction of **Figure 4–18** at the same engine working point, where a 70% soot reduction was obtained at fixed BSNOx. Thanks to the improved trade-off for the hybrid bowl, higher EGR rate can be considered to reach the EU6d NOx target, still maintaining the ISPM reduction in the range of 50-60%.

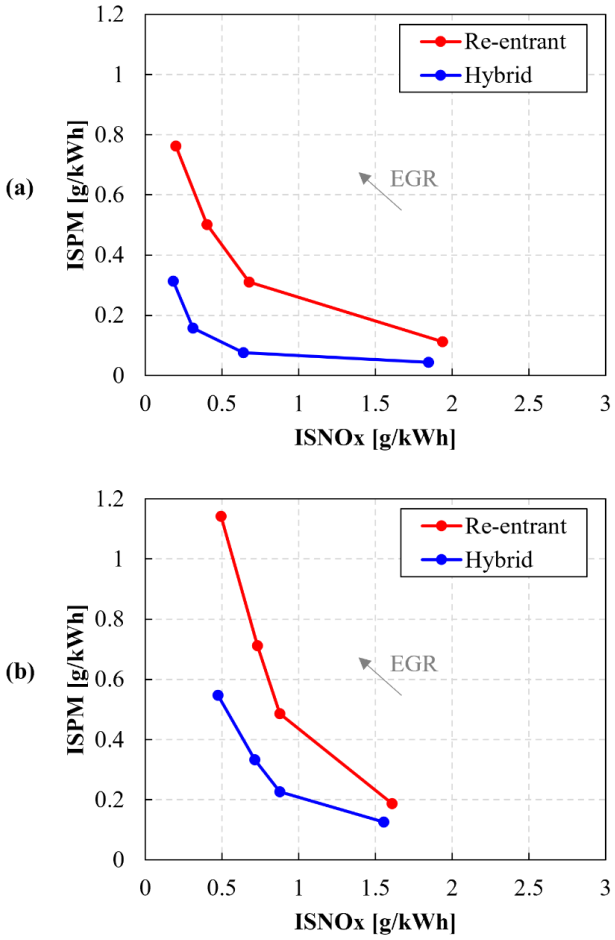

Figure 4–43: EGR sweep trade-offs. (a) Engine operating condition: 1500 RPM x 5.0 bar BMEP; (a) Engine operating condition: 2000 RPM x 8.0 bar BMEP. Adapted from [43].

Figure 4–44 the BSFC, combustion noise and specific brake emissions for both the piston bowls and all the engine operating conditions under investigation. The results from the SCE tests were reflected to the actual conditions of the muti-cylinder engine by means of the friction correlation reported in [86]. The brake specific results were normalized with respect to the conventional re-entrant bowl data. Also, the combustion noise absolute values were reported. All the comparison are at constant EU6b engine-out NOx targets. The radar plots show a BSFC reduction in the range 0-2% with respect to the re-entrant bowl. In general, at lower load, no significant change can be detected in terms of BSCO and BSTHC, while increasing the load a strong BSTHC increment is detected. This could be related to the low-quality roughness within the AM piston design that affects the wall wetting phenomenon. Although the BSTHC percentage increment is significant, at this high load and warm conditions, the HC absolute values are very low and within the tolerance range. The greatest benefit provided by the hybrid bowl is in terms of PM reduction. The reduction is in the range of 30-80% with respect to the re-entrant bowl, confirming the great potential of the hybrid bowl in terms of soot mitigation.

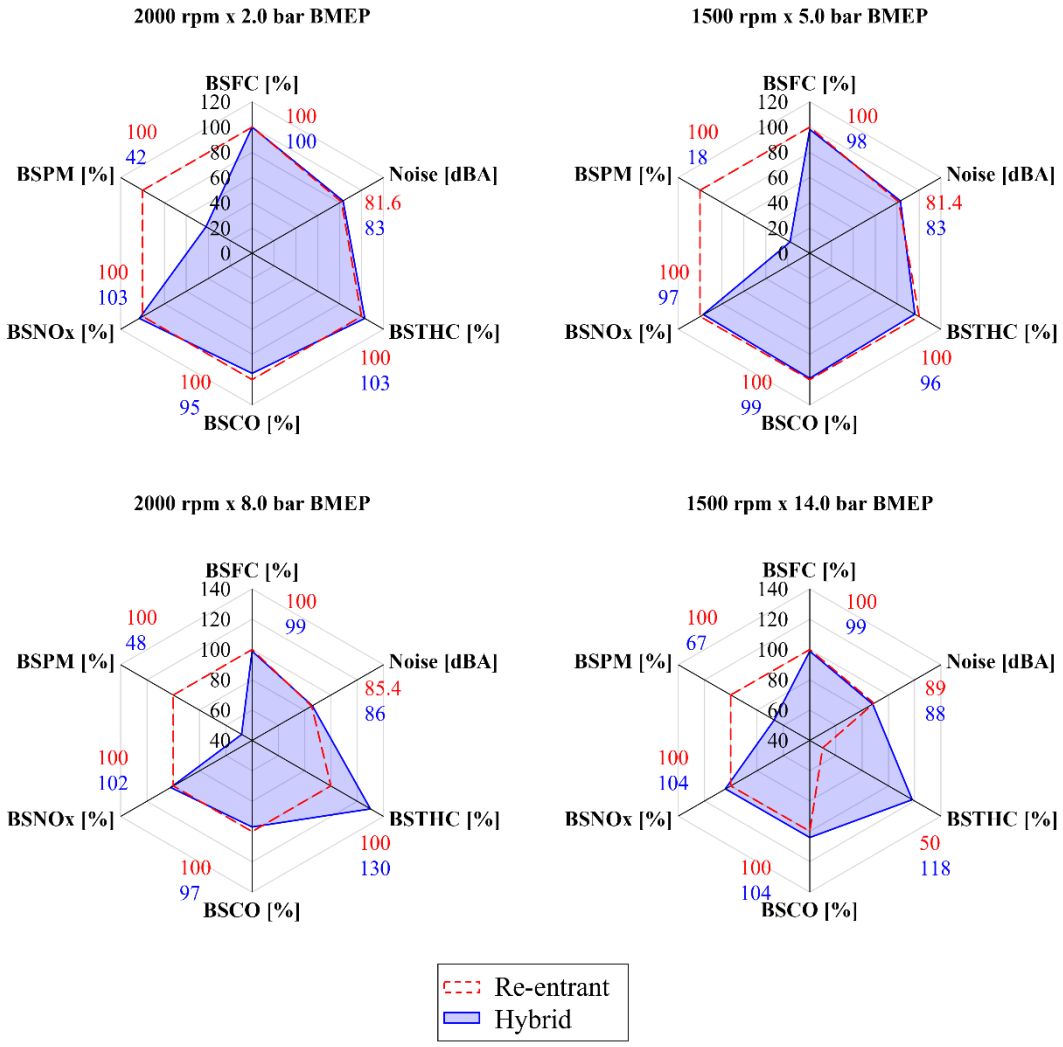

Figure 4–44: Experimental results in terms of BSFC, combustion noise and specific brake emissions for both piston and all the engine operating conditions. Adapted from [43].

Chapter 5

Conclusions and Outlook

In the last years, the increasingly demanding CO_2 legislative targets and the need to comply with tighter emissions regulations are pushing toward an unprecedent technological innovation. In this scenario, for a diesel engine, the in-cylinder control of pollutant emissions will still play a fundamental role to reduce the incremental cost due to the adoption of advanced aftertreatment systems. With this aim, the optimization of the piston bowl design was found to have a key role on the air/fuel mixing, resulting in lower fuel consumption and emissions. During the design optimization process, the 3D-CFD simulations can be used as virtual test rig for the preliminary assessment of the most promising geometries, saving time and cost with respect to the experimental tests.

In this work, the performance of different piston bowl geometries for a 1.6L diesel engine was investigated by means of a synergetic approach based on both 3D-CFD simulations and experimental tests. Regarding the simulation methodology, an integrated and automated 1D-/3D-CFD coupling approach was adopted which includes a calibrated spray model and detailed chemistry. Once the numerical model was validated considering a conventional re-entrant bowl, two innovative bowl geometries were numerically investigated: a stepped-lip and a radial-bumps bowl. Under non-reacting conditions, both the stepped-lip and radial-bumps bowls highlighted an improved air/fuel mixing with respect to the re-entrant design. In particular, the stepped-lip bowl provided a dual toroidal vortex that increases the air utilization in the squish region, while the radial-bumps bowl mitigated the jet-to-jet interaction and promoted the recirculation of

the jet downstream to the bump, where the available oxygen enhanced the air/fuel mixing rate. The combustion simulations confirmed that the enhanced mixing led to improved combustion, increasing the engine efficiency at full load, and minimizing the engine-out soot at part load. Then, to further assess the potentials of these innovative designs, a sensitivity analysis over different engine calibration parameters was carried out. At full load, a faster mixing-controlled combustion was reached with both innovative designs due to the optimal injection phasing. Also, a higher swirl ratio was found to be necessary for improved mixing, especially for the radial-bumps bowl. Both the innovative bowls highlighted high potential in reducing the ISFC, -1% and -3% for the stepped-lip and radial-bumps bowls, respectively. At partial load, both the stepped-lip and the radial-bumps bowls showed a remarkable improvement of the soot-NOx trade-off, providing 40% and 50% of soot reduction with respect to the re-entrant bowl.

Once assessed the combustion improvement due to the stepped-lip and radial-bumps bowls, a further step on the combustion system optimization was carried out. To understand if there are synergies between these two pistons, an innovative hybrid piston was designed. The hybrid bowl combined a highly-reentrant sharp-stepped bowl and a number of radial bumps in the inner bowl rim equal to the injector nozzle holes. Due to the geometrical complexity of this piston design, an AM oriented steel-based approach was adopted. The hybrid bowl was firstly investigated through 3D-CFD simulations. Then, the numerical results were compared against the experimental data coming from an optical access engine. The CIV and OH* chemiluminescence data were used for the characterization of the flame structure. Then, the 2-color pyrometry KL data were adopted for the investigation of soot. To directly compare the numerical and experimental data, a numerical methodology was developed, providing an equivalent soot KL also in the 3D-CFD environment. Regarding the 3D-CFD simulations, under non-reacting conditions, the hybrid bowl showed a strong improvement of the air/fuel mixing with respect to the re-entrant bowl. The jet-to-jet interaction was reduced, increasing the air entrainment into the jet front. Moreover, a higher jet recirculation toward the bowl center was reported, improving the mixing rate due to the higher available oxygen. The combustion simulations have confirmed the mixing behavior, resulting in higher HRR in the mixing-controlled combustion for both full load and partial loads operating conditions. At partial loads, the hybrid bowl has shown a great EGR tolerance over the soot-BSNOx and BSFC-BSNOx trade-offs. At baseline BSNOx, up to 70% soot reduction was obtained with negligible fuel consumption worsening. To fully optimize this innovative

combustion system, the hybrid bowl potentials were also investigated for different injector protrusions and swirl ratio. The hybrid bowl showed high sensitivity to the injector protrusion both in terms of soot and BSFC, suggesting that the optimal fuel split on the step is crucial for the combustion enhancement. Moreover, high swirl ratio was required to keep lower soot and BSFC than with the re-entrant bowl due to the enhanced mixing process. At full load, for the optimal injector protrusion and the higher swirl ratio, 40% soot and 2% BSFC reduction were obtained with respect to the conventional re-entrant bowl. The summary of the numerical results is reported in **Table 5–1** in terms of soot, BSFC and power percentage difference with respect to the re-entrant bowl.

Table 5–1: Numerical results. Soot, BSFC and power percentage difference with respect to the re-entrant bowl.

		Stepped-lip	**Radial-bumps**	**Hybrid**
WP1	**Soot**	-40%	-50%	-70%
	BSFC	-0.5%	-5.0%	-0.7%
WP3	**Power**	+0.3%	+3.3%	+1.7%

Then, the experimental data from an optical access engine were used to characterize the hybrid bowl design in terms of flame and soot evolutions. The qualitative comparison between the numerical and CIV-resolved velocity flow fields showed a good agreement. Interestingly, the hybrid bowl highlighted a higher flame velocity toward the piston center, and it was mainly driven by the radial bump geometry. This faster reverse flow of the flame resulted in higher air entrainment into the flame front, thus improving the combustion rate. Also, the comparison between the numerical OH distribution and the OH* chemiluminescence data showed a qualitative good agreement, confirming the potential of the hybrid bowl on the combustion rate. In particular, a higher OH content was observed both in the piston center and above the step, providing a faster oxidation process. Concerning soot evolution, the numerical soot KL was compared with the optical soot density KL showing also in this case a qualitative

good agreement. More in detail, a strong improvement of soot formation/oxidation processes was highlighted due to the hybrid bowl geometry. On one side, the reduced flame-to-flame interaction significantly mitigated the soot formation, while, on the other side, the faster flame recirculation toward the piston center increased the oxidation rate. In the framework of a collaboration between PUNCH Torino S.p.A/ formerly General Motors Global Propulsion Systems and CNR – STEMS, an experimental activity was carried with a SCE based on similar architecture and piston designs as the ones used in the numerical analysis. The results of this analysis have confirmed the great soot reduction potential of the hybrid bowl. The experimental soot reduction was in the range of 30-80% with respect to a conventional re-entrant bowl, keeping fixed ISNOx equal to EU6b target. The summary of the numerical and experimental results for the hybrid bowl is reported in **Table 5–2** in terms of soot and BSFC percentage difference with respect to the re-entrant bowl.

Table 5–2: Hybrid bowl, numerical and experimental results. Soot and BSFC percentage difference with respect to the re-entrant bowl.

		3D-CFD	**Experimental**
WP1	**Soot**	-70%	-75%
	BSFC	-0.7%	-2.0%
WP2	**Soot**	-70%	-54%
	BSFC	-1.0%	-1.0%

The optimization of the piston bowl design was found to be crucial for fuel efficiency and emissions reduction, thanks to the improvement of the mixing behavior. The developed 3D-CFD methodology has shown great predictive capabilities, paving the way for further geometrical optimization. In this framework, the DoE and GA algorithms as well as the recent rising of the machine learning approach can support the optimization process. From a manufacturing perspective, the recent improvement of AM steel-based method

enabled the possibility of strong geometrical complexity, while keeping the durability request of a diesel engine application. Then, further steps can be done for the next generation of diesel engines to minimize their environmental impact on the transportation sector.

References

1. International Council On Clean Transportation (ICCT), “Vision 2050: A strategy to decarbonize the global transport sector by mid-century,” 2020, https://theicct.org/publication/vision-2050-a-strategy-to-decarbonize-the-global-transport-sector-by-mid-century/, accessed June 2023.

2. Belgiorno, G., Dimitrakopoulos, N., Di Blasio, G., Beatrice, C. et al., “Effect of the Engine Calibration Parameters on Gasoline Partially Premixed Combustion Performance and Emissions Compared to Conventional Diesel Combustion in a Light-Duty Euro 6 Engine,” Applied Energy 228 (2018):2221-2234, https://doi.org/10.1016/j.apenergy.2018.07.098.

3. Benajes, J., García, A., Monsalve-Serrano, J., and Lago Sari, R., “Fuel Consumption and Engine-Out Emissions Estimations of a Light-Duty Engine Running in Dual-Mode RCCI/CDC with Different Fuels and Driving Cycles,” Energy 157 (2018): 19-30, https://doi.org/10.1016/j.energy.2018.05.144.

4. Pastor, J.V., García, A., Micó, C., and Lewiski, F., “An Optical Investigation of Fischer-Tropsch Diesel and Oxymethylene Dimethyl Ether Impact on Combustion Process for CI Engines,” Applied Energy 260 (2020): 114238, https://doi.org/10.1016/j.apenergy.2019.114238.

5. Zhang, T., Eismark, J., Munch, K., and Denbratt, I., “Effects of a wave-shaped piston bowl geometry on the performance of heavy duty Diesel engines fueled with alcohols and biodiesel blends,” *Renewable Energy* 148:512–522, 2020, https://doi.org/10.1016/j.renene.2019.10.057.

6. Millo, F., Piano, A., Rolando, L., Accurso, F. et al., "Synergetic Application of Zero-, One-, and Three-Dimensional Computational Fluid Dynamics Approaches for Hydrogen-Fuelled Spark Ignition Engine Simulation," SAE Int. J. Engines 15(4):561-580, 2022, https://doi.org/10.4271/03-15-04-0030.

7. International Energy Agency (IEA), “World Energy Outlook 2022,” 2022, https://www.iea.org/reports/world-energy-outlook-2022, accessed June 2023.

8. International Council On Clean Transportation (ICCT), “European Vehicle

Market Statistics," 2023, https://theicct.org/publication/european-vehicle-market-statistics-2022-23/, accessed June 2023.

9. Lückert, P., Arndt, S., Duvinage, F., Kemmner, M. et al., "The New Mercedes-Benz 4-Cylinder Diesel Engine OM654 – The Innovative Base Engine of the New Diesel Generation," 24th Aachen Colloquium Automobile and Engine Technology, 867–892, 2015.

10. Sanchez, F.P., Bandivadekar, A., and German, J., "Estimated cost of emission reduction technologies for LDVs," *Int. Counc. Clean Transp. (ICCT)*, 2012, https://theicct.org/publication/estimated-cost-of-emission-reduction-technologies-for-ldvs/, accessed June 2023.

11. Ragon, P.-L. and Rodríguez, F., "Estimated cost of diesel emissions control technology to meet future Euro VII standards," *Int. Counc. Clean Transp. (ICCT)*, 2021, https://theicct.org/publication/estimated-cost-of-diesel-emissions-control-technology-to-meet-future-euro-vii-standards/, accessed June 2023.

12. Dallmann, T., Posada, F., and Bandivadekar, A., "Costs of Emission Reduction Technologies for Diesel Engines Used in Non-Road Vehicles and Equipment," *Int. Counc. Clean Transp.* (ICCT), 2018, https://theicct.org/publication/costs-of-emission-reduction-technologies-for-diesel-engines-used-in-non-road-vehicles-and-equipment/, accessed June 2023.

13. Miles, P.C. and Andersson, Ö., "A review of design considerations for light-duty diesel combustion systems," *International Journal of Engine Research* 17(1):6–15, 2016, https://doi.org/10.1177/1468087415604754.

14. Andersson, Ö. and Miles, P.C., "Diesel and Diesel LTC Combustion," Encyclopedia of Automotive Engineering, 1-36, 2014, https://doi.org/10.1002/9781118354179.auto120.

15. Miles, P.C., "Turbulent Flow Structure in Direct-Injection, Swirl-Supported Diesel Engines," In: Arcoumanis C., Kamimoto T. (eds) Flow and Combustion in Reciprocating Engines. Experimental Fluid Mechanics. Springer, Berlin, Heidelberg, 2008, https://doi.org/10.1007/978-3-540-68901-0_4.

16. Broatch, A., Novella, R., Gomez-Soriano, J., Pal, P. et al., "Numerical Methodology for Optimization of Compression-Ignited Engines Considering Combustion Noise Control," SAE Int. J. Engines 11(6):625-642, 2018, https://doi.org/10.4271/2018-01-0193.

17. Martínez-Rodríguez, D., Novella, R., Bracho, G., Gomez-Soriano, J. et al., “A particle swarm optimization algorithm with novelty search for combustion systems with ultra-low emissions and minimum fuel consumption,” *Applied Soft Computing,* 143:110401, 2023, https://doi.org/10.1016/j.asoc.2023.110401.

18. Pei, Y., Pal, P., Zhang, Y., Traver, M. et al., "CFD-Guided Combustion System Optimization of a Gasoline Range Fuel in a Heavy-Duty Compression Ignition Engine Using Automatic Piston Geometry Generation and a Supercomputer," SAE Int. J. Adv. & Curr. Prac. in Mobility 1(1):166-179, 2019, https://doi.org/10.4271/2019-01-0001.

19. Badra, J., khaled, F., Sim, J., Pei, Y. et al., "Combustion System Optimization of a Light-Duty GCI Engine Using CFD and Machine Learning," SAE Technical Paper 2020-01-1313, 2020, https://doi.org/10.4271/2020-01-1313.

20. Moiz, A., Pal, P., Probst, D., Pei, Y. et al., "A Machine Learning-Genetic Algorithm (ML-GA) Approach for Rapid Optimization Using High-Performance Computing," SAE Int. J. Commer. Veh. 11(5):291-306, 2018, https://doi.org/10.4271/2018-01-0190.

21. Dolan, R., Budde, R., Schramm, C., and Rezaei, R., “3D Printed Piston for Heavy-Duty Diesel Engines”, in 2018 Ndia Ground Vehicle Systems Engineering and Technology Symposium, Power & Mobility (P&M) Technical Session, August 7-9, 2018 - NOVI, MICHIGAN, https://events.esd.org/wp-content/uploads/2018/07/3D-Printed-Piston-for-Heavy-Duty-Diesel-Engines.pdf, accessed June 2023.

22. Krause, M., Budde, R., Rezaei, R., and Kovàcs, D., “Development of an Additive Manufactured Heavy-Duty Piston with an Innovative Piston Bowl,” 21st Stuttgart International Symposium, Proceedings, 2021, https://doi.org/10.1007/978-3-658-33466-6_34.

23. Di Blasio, G., Ianniello, R., Beatrice, C., Pesce, F.C., et al., “Additive Manufacturing New Piston Design and Injection Strategies for Highly Efficient and Ultra-Low Emissions Combustion in View of 2030 Targets,” *Fuel,* 346:128270, 2023, https://doi.org/10.1016/j.fuel.2023.128270.

24. Busch, S., Zha, K., Perini, F., Reitz, R. et al., "Bowl Geometry Effects on Turbulent Flow Structure in a Direct Injection Diesel Engine," SAE Technical Paper 2018-01-1794, 2018, https://doi.org/10.4271/2018-01-1794.

25. Busch, S., Zha, K., Kurtz, E., Warey, A. et al., "Experimental and

Numerical Studies of Bowl Geometry Impacts on Thermal Efficiency in a Light-Duty Diesel Engine," SAE Technical Paper 2018-01-0228, 2018, https://doi.org/10.4271/2018-01-0228.

26. Zha, K., Busch, S., Warey, A., Peterson, R. et al., "A Study of Piston Geometry Effects on Late-Stage Combustion in a Light-Duty Optical Diesel Engine Using Combustion Image Velocimetry," *SAE Int. J. Engines* 11(6):783-804, 2018, https://doi.org/10.4271/2018-01-0230.

27. Yoo, D., Kim, D., Jung, W., Kim, N. et al., "Optimization of Diesel Combustion System for Reducing PM to Meet Tier4-Final Emission Regulation without Diesel Particulate Filter," SAE Technical Paper 2013-01-2538, 2013, https://doi.org/10.4271/2013-01-2538.

28. Sandia National Laboratories, "Piston Bowl Geometry Study," https://ecn.sandia.gov/engines/small-bore-diesel-engine/experimental-data/piston-bowl-geometry-study/, accessed June 2023.

29. Cornwell, R. and Conicella, F., "Direct Injection Diesel Engines," Ricardo UK Limited, West Sussex (GB), U.S. Patent 8770168 B2, 2014.

30. Styron, J., Baldwin, B., Fulton, B., Ives, D. et al., "Ford 2011 6.7L Power Stroke® Diesel Engine Combustion System Development," SAE Technical Paper 2011-01-0415, 2011, https://doi.org/10.4271/2011-01-0415.

31. Kogo, T., Hamamura, Y., Nakatani, K., Toda, T. et al., "High Efficiency Diesel Engine with Low Heat Loss Combustion Concept - Toyota's Inline 4-Cylinder 2.8-Liter ESTEC 1GD-FTV Engine -," SAE Technical Paper 2016-01-0658, 2016, https://doi.org/10.4271/2016-01-0658.

32. Millo, F., Piano, A., Peiretti Paradisi, B., Boccardo, G. et al., "The Effect of Post Injection Coupled with Extremely High Injection Pressure on Combustion Process and Emission Formation in an Off-Road Diesel Engine: A Numerical and Experimental Investigation," SAE Technical Paper 2019-24-0092, 2019, https://doi.org/10.4271/2019-24-0092.

33. Green Car Congress, "JCB's New Ecomax T4 Engine Uses Ricardo Low Emissions Combustion Technology; Tier 4 Interim Level Emissions With No Exhaust Aftertreatment", 2010, https://www.greencarcongress.com/2010/03/jcb-20100319.html, accessed June 2023.

34. Kurtz, E. and Styron, J., "An Assessment of Two Piston Bowl Concepts in a Medium-Duty Diesel Engine," *SAE Int. J. Engines* 5(2):344-352, 2012, https://doi.org/10.4271/2012-01-0423.

35. Eder, T., Kemmner, M., Lückert, P., and Sass, H., “OM 654 – Launch of a New Engine Family by Mercedes-Benz,” MTZ Worldwide, 2016.

36. Eismark, J., Balthasar, M., Karlsson, A., Benham, T. et al., "Role of Late Soot Oxidation for Low Emission Combustion in a Diffusion-controlled, High-EGR, Heavy Duty Diesel Engine," SAE Technical Paper 2009-01-2813, 2009, https://doi.org/10.4271/2009-01-2813.

37. Eismark, J. and Balthasar, M., “Device for reducing emissions in a vehicle combustion engine,” Volvo Lastvagnar AB, Göteborg (SE), U.S. Patent 8499735B2, 2013.

38. Eismark, J., Andersson, M., Christensen, M., Karlsson, A. et al., "Role of Piston Bowl Shape to Enhance Late-Cycle Soot Oxidation in Low-Swirl Diesel Combustion," *SAE Int. J. Engines* 12(3):233-249, 2019, https://doi.org/10.4271/03-12-03-0017.

39. Eismark, J., Christensen, M., Andersson, M., Karlsson, A., et al., “Role of fuel properties and piston shape in influencing soot oxidation in heavy-duty low swirl diesel engine combustion,” *Fuel*, Volume 254, 2019, 115568, ISSN 0016-2361, https://doi.org/10.1016/j.fuel.2019.05.151.

40. Gong, M., Derafshzan, S., Richter, M., Hemdal, S. et al., "An Optical Study of the Effects of Diesel-like Fuels with Different Densities on a Heavy-duty CI Engine with a Wave-shaped Piston Bowl Geometry," SAE Technical Paper 2023-01-0261, 2023, https://doi.org/10.4271/2023-01-0261.

41. Millo, F., Piano, A., Roggio, S., Bianco, A. et al., "Numerical Investigation on Mixture Formation and Combustion Process of Innovative Piston Bowl Geometries in a Swirl-Supported Light-Duty Diesel Engine," *SAE Int. J. Engines* 14(2):247-262, 2021, https://doi.org/10.4271/03-14-02-0015.

42. Belgiorno, G., Boscolo, A., Dileo, G., Numidi, F. et al., "Experimental Study of Additive-Manufacturing-Enabled Innovative Diesel Combustion Bowl Features for Achieving Ultra-Low Emissions and High Efficiency," SAE Int. J. Adv. & Curr. Prac. in Mobility 3(1):672-684, 2021, https://doi.org/10.4271/2020-37-0003.

43. Di Blasio, G., Ianniello, R., Beatrice, C., Pesce, F.C., et al., “Experimental Investigation on an Innovative Additive Manufacturing-Enabled Diesel Piston Design to improve Engine-out Emissions and Thermal Efficiency beyond Euro6,” *THIESEL 2020 Conference on Thermo- and Fluid Dynamic Processes in Direct Injection Engines*, 2020.

44. Pastor, J. V., García, A., Micó, C., Lewiski, F. et al., “Effect of a novel

piston geometry on the combustion process of a light-duty compression ignition engine: an optical analysis," *Energy* 221:119764, 2021, https://doi.org/10.1016/j.energy.2021.119764.

45. Pastor, J. V., García, A., Micó, C., and Lewiski, F., "Soot reduction for cleaner Compression Ignition Engines through innovative bowl templates," *International Journal of Engine Research*, 2020, https://doi.org/10.1177/1468087420951324.

46. Millo, F., Piano, A., Roggio, S., Pastor, J.V. et al., "Mixture formation and combustion process analysis of an innovative diesel piston bowl design through the synergetic application of numerical and optical techniques," *Fuel*, 2022, 309:122144, https://doi.org/10.1016/j.fuel.2021.122144.

47. Piano, A., Roggio, S., Millo, F., García, A. et al., "Numerical and optical soot characterization through 2-color pyrometry technique for an innovative diesel piston bowl design", *Fuel*, 2023, 333:126347, https://doi.org/10.1016/j.fuel.2022.126347.

48. Millo, F., Piano, A., Peiretti Paradisi, B., Marzano, M.R., Bianco, A., and Pesce, F.C., "Development and Assessment of an Integrated 1D-3D CFD Codes Coupling Methodology for Diesel Engine Combustion Simulation and Optimization," *Energies* 2020, *13*, 1612, https://doi.org/10.3390/en13071612.

49. Piano, A., Millo, F., Boccardo, G., Rafigh, M. et al., "Assessment of the Predictive Capabilities of a Combustion Model for a Modern Common Rail Automotive Diesel Engine," SAE Technical Paper 2016-01-0547, 2016, https://doi.org/10.4271/2016-01-0547.

50. Piano, A., Millo, F., Postrioti, L., Biscontini, G. et al., "Numerical and Experimental Assessment of a Solenoid Common-Rail Injector Operation with Advanced Injection Strategies," *SAE Int. J. Engines* 9(1):565-575, 2016, https://doi.org/10.4271/2016-01-0563.

51. Piano, A., Boccardo, G., Millo, F., Cavicchi, A. et al., "Experimental and Numerical Assessment of Multi-Event Injection Strategies in a Solenoid Common-Rail Injector," *SAE Int. J. Engines* 10(4):2129-2140, 2017, https://doi.org/10.4271/2017-24-0012.

52. Richards, K. J., Senecal, P.K. and Pomraning, E., "Converge 2.3 Manual," Convergent Science Inc.: Madison, WI, USA, 2016.

53. Issa, R.I., "Solution of the Implicitly Discretised Fluid Flow Equations by Operator-Splitting," Journal of Computational Physics 62, no. 1 (1986): 40-

65, https://doi.org/10.1016/0021-9991(86)90099-9.

54. Rhie, C.M. and Chow, W.L., “Numerical Study of the Turbulent Flow Past an Airfoil with Trailing Edge Separation,” AIAA Journal 21, no. 11 (1983): 1525-1532, https://doi.org/10.2514/3.8284.

55. Orszag, S. A., Yakhot, V., Flannery, W. S., Boysan, F. et al., “Renormalization Group Modeling and Turbulence Simulations,” *Near-Wall Turbulent Flows 1993*, 13, 1031–1046.

56. Yakhot, V., Orszag, S.A., Thangam, S., and Gatski, T.B., “Development of Turbulence Models for Shear Flows by a Double Expansion Technique,” Physics of Fluids A: Fluid Dynamics 4 (1992): 1510, https://doi.org/10.1063/1.858424.

57. Versteeg, H.K. and Malalasekera, W., "An Introduction to Computational Fluid Dynamics: The Finite Volume Method," Pearson Prentice Hall, 2007.

58. Amsden, A.A., "KIVA-3V: A Block Structured KIVA Program for Engines with Vertical or Canted Valves," Los Alamos National Laboratory Technical Report LA-13313-MS, 1997.

59. Reitz, R.D. and Bracco, F.V., “Mechanisms of Breakup of Round Liquid Jets,” *Encyclopedia of Fluid Mechanism*, 1986, 3, 233–249.

60. Amsden, A.A., O’Rourke, P.J., and Butler, T.D., "KIVA-II: A Computer Program for Chemically Reactive Flows with Sprays," Los Alamos National Laboratory Technical Report LA-11560-MS, 1989.

61. Schmidt, D.P. and Rutland, C.J., “A New Droplet Collision Algorithm,” *Journal of Computational Physics*, Volume 164, Issue 1, 2000, Pages 62-80, ISSN 0021-9991, https://doi.org/10.1006/jcph.2000.6568.

62. O'Rourke, P. and Amsden, A., "The Tab Method for Numerical Calculation of Spray Droplet Breakup," SAE Technical Paper 872089, 1987, https://doi.org/10.4271/872089.

63. O'Rourke, P. and Amsden, A., "A Spray/Wall Interaction Submodel for the KIVA-3 Wall Film Model," SAE Technical Paper 2000-01-0271, 2000, https://doi.org/10.4271/2000-01-0271.

64. Postrioti, L., Grimaldi, C., Ceccobello, M., and Di Gioia, R., "Diesel Common Rail Injection System Behavior with Different Fuels," SAE Technical Paper 2004-01-0029, 2004, https://doi.org/10.4271/2004-01-0029.

65. Postrioti, L., Buitoni, G., Pesce, F.C., and Ciaravino, C., “Zeuch method-based injection rate analysis of a common-rail system operated with advanced injection strategies,” *Fuel* 128:188–198, 2014, https://doi.org/10.1016/j.fuel.2014.03.006.

66. Zeuch, T., Moréac, G., Ahmed, S.S. and Mauss, F., “A comprehensive skeletal mechanism for the oxidation of n-heptane generated by chemistry-guided reduction,” *Combustion and Flame*, Volume 155, Issue 4, 2008, Pages 651-674, ISSN 0010-2180, https://doi.org/10.1016/j.combustflame.2008.05.007.

67. Frenklach, M. and Wang, H., "Detailed Modeling of Soot Particle Nucleation and Growth," *Symposium (International) on Combustion*, Volume 23, Issue 1, 1991, Pages 1559-1566, ISSN 0082-0784, https://doi.org/10.1016/S0082-0784(06)80426-1.

68. Kazakov, A., Wang, H., and Frenklach, M., “Detailed modeling of soot formation in laminar premixed ethylene flames at a pressure of 10 bar,” *Combustion and Flame*, Volume 100, Issues 1–2, 1995, Pages 111-120, ISSN 0010-2180, https://doi.org/10.1016/0010-2180(94)00086-8.

69. Kazakov, A. and Frenklach, M., “Dynamic Modeling of Soot Particle Coagulation and Aggregation: Implementation With the Method of Moments and Application to High-Pressure Laminar Premixed Flames,” *Combustion and Flame*, Volume 114, Issues 3–4, 1998, Pages 484-501, ISSN 0010-2180, https://doi.org/10.1016/S0010-2180(97)00322-2.

70. Payri, F., Olmeda, P., Martín, J., and García, A., “A complete 0D thermodynamic predictive model for direct injection diesel engines,” Applied Energy 88(12):4632–4641, 2011, https://doi.org/10.1016/j.apenergy.2011.06.005.

71. Pastor, J.V., Olmeda, P., Martín, J., and Lewiski, F., "Methodology for Optical Engine Characterization by Means of the Combination of Experimental and Modeling Techniques," Applied Sciences. 2018; 8(12):2571. https://doi.org/10.3390/app8122571.

72. Thielicke, W. and Stamhuis, E.J., “PIVlab – Towards User-friendly, Affordable and Accurate Digital Particle Image Velocimetry in MATLAB,” J. Open Res. Softw. 2, 2014, http://doi.org/10.5334/jors.bl.

73. Dembinski, H., Angstrom, H., and Razzaq, H., "In-Cylinder Flow Pattern Evaluated with Combustion Image Velocimetry, CIV, and CFD Calculations during Combustion and Post-Oxidation in a HD Diesel Engine," SAE Technical Paper 2013-24-0064, 2013,

https://doi.org/10.4271/2013-24-0064.

74. Hottel, H. C. and Broughton, F. P., "Determination of True Temperature and Total Radiation from Luminous Gas Flames," *Industrial & Engineering Chemistry Analytical Edition*, 4(2):166-175, 1932, https://doi.org/10.1021/ac50078a004.

75. Yan, J. and Borman, G., "Analysis and In-Cylinder Measurement of Particulate Radiant Emissions and Temperature in a Direct Injection Diesel Engine," SAE Technical Paper 881315, 1988, https://doi.org/10.4271/881315.

76. Kamimoto, T. and Murayama Y., "Re-examination of the emissivity of diesel flames," International Journal of Engine Research, 12(6):580-600, 2011, https://doi.org/10.1177/1468087411418170.

77. Pastor, J. V., García-Oliver, J.M., García, A., Micó, C., and Möller, S., "Application of optical diagnostics to the quantification of soot in n-alkane flames under diesel conditions," *Combustion and Flame* 164:212–223, 2016, https://doi.org/10.1016/j.combustflame.2015.11.018.

78. Hessel, R., Yue, Z., Reitz, R., Musculus, M. et al., "Guidelines for Interpreting Soot Luminosity Imaging," SAE Int. J. Engines 10(3):1174-1192, 2017, https://doi.org/10.4271/2017-01-0716.

79. Yu, X., Zha, K., Florea, R., and Jansons, M., "Comparison of In-Cylinder Soot Evolution in an Optically Accessible Engine Fueled with JP-8 and ULSD," SAE Int. J. Fuels Lubr. 5(2):875-891, 2012, https://doi.org/10.4271/2012-01-1315.

80. Modest, M.F., "Radiative Heat Transfer," 2013, ISBN 9780123869449, https://doi.org/10.1016/B978-0-12-386944-9.50038-8.

81. Perini, F., Zha, K., Busch, S., Kurtz, E. et al., "Piston geometry effects in a light-duty, swirl-supported diesel engine: Flow structure characterization," *International Journal of Engine Research*, 19(10):1079–1098, 2018, https://doi.org/10.1177/1468087417742572.

82. Celik, I., Yavuz, I., Smirnov, A., Smith, J. et al., "Prediction of In-Cylinder Turbulence for IC Engines," *Combustion Science and Technology*, 153:1, 339-368, 2000, https://doi.org/10.1080/00102200008947269.

83. Lin, L., Shulin, D., Jin, X., Jinxiang, W. et al., "Effects of Combustion Chamber Geometry on In-Cylinder Air Motion and Performance in DI Diesel Engine," SAE Technical Paper 2000-01-0510, 2000,

https://doi.org/10.4271/2000-01-0510.

84. Dolak, J., Shi, Y., and Reitz, R., "A Computational Investigation of Stepped-Bowl Piston Geometry for a Light Duty Engine Operating at Low Load," SAE Technical Paper 2010-01-1263, 2010, https://doi.org/10.4271/2010-01-1263.

85. Verdino, V., Lavazza, P., Rampone, D., Garzarella, L., et al., "The New General Motors 3.0 Liter Duramax Diesel Inline 6-cylinder Engine for the 2019 Chevrolet Silverado and GMC Sierra," 40th International Vienna Motor Symposium, 2019.

86. Beatrice, C., Di Blasio, G., Pesce, F., Vassallo, A. et al., "Key Fuel Injection System Features for Efficiency Improvement in Future Diesel Passenger Cars," SAE Int. J. Adv. & Curr. Prac. in Mobility 1(3):1084-1099, 2019, https://doi.org/10.4271/2019-01-0547.

Publications

The research project described in this PhD thesis was also previously published in the following journal articles and presented at the following international conferences:

Journal articles

- Millo, F., Piano, A., Roggio, S., Bianco, A. et al., "Numerical Investigation on Mixture Formation and Combustion Process of Innovative Piston Bowl Geometries in a Swirl-Supported Light-Duty Diesel Engine," SAE Int. J. Engines 14(2):247-262, 2021, https://doi.org/10.4271/03-14-02-0015.
- Millo, F., Piano, A., Roggio, S., Pesce, F.C., Vassallo, A., Bianco, A., "Numerical Assessment on the Influence of Engine Calibration Parameters on Innovative Piston Bowls Designed for Light-Duty Diesel Engines," Energies, 15(10):3799, 2022, https://doi.org/10.3390/en15103799.
- Millo, F., Piano, A., Roggio, S., Bianco, A. et al., "Numerical Assessment of Additive Manufacturing-Enabled Innovative Piston Bowl Design for a Light-Duty Diesel Engine Achieving Ultra-Low Engine-Out Soot Emissions," SAE Int. J. Engines 15(3):2022, https://doi.org/10.4271/03-15-03-0022.
- Millo, F., Piano, A., Roggio, S., Pastor, J.V. et al., "Mixture formation and combustion process analysis of an innovative diesel piston bowl design through the synergetic application of numerical and optical techniques," Fuel, 2022, 309:122144, https://doi.org/10.1016/j.fuel.2021.122144.
- Piano, A., Roggio, S., Millo, F., García, A. et al., "Numerical and optical soot characterization through 2-color pyrometry technique for an innovative diesel piston bowl design", Fuel, 2023, 333:126347, https://doi.org/10.1016/j.fuel.2022.126347.

Proceedings and international conferences

- Millo, F., Piano, A., Roggio, S., Bianco, A. et al., "Numerical Assessment of an Innovative Piston Bowl Concept in a Light-duty Diesel Engine," Proceeding of the 2020 SIA Powertrain & Energy International Congress, November 16-29, 2020, digital platform.
- Millo, F., Piano, A., Roggio, S., Bianco, A. et al., "Numerical Investigation on Mixture Formation and Combustion Process of Innovative Piston Bowl Geometries in a Swirl-Supported Light-Duty Diesel Engine," SAE International's WCX2021 Digital Summit, April 13-15, 2021.
- Millo, F., Piano, A., Roggio, S., Bianco, A. et al., "Numerical investigation of an innovative piston bowl design in a light-duty diesel engine achieving ultra-low engine-out soot emissions," 15th International Conference on Engines & Vehicles, Capri, Napoli (Italy), September 12-16, 2021.
- Millo, F., Piano, A., Roggio, S., Pastor, J.V. et al., "Synergetic application of numerical and optical techniques for mixture formation and combustion process investigation of an innovative diesel piston bowl design," SAE International's WCX2022, April 5-7, 2022.
- Millo, F., Piano, A., Roggio, S., García, A. et al., "Numerical and optical soot characterization through 2-color pyrometry technique for an innovative diesel piston bowl design," SAE International's WCX2023, April 18-20, 2023.

As side research activity, the potentials of hydrogen internal combustion engine (H2-ICE) were numerically evaluated. A comprehensive 0/1/3D-CFD synergetic approach was developed to assess the H2-ICE performances, considering different architectures (PFI, DI, TJI, dual-fuel H2-diesel). The results of this research activity were published in the following journal article and presented in the following international conferences:

Journal articles

- Millo, F., Piano, A., Rolando, L., Accurso, F. et al., "Synergetic Application of Zero-, One-, and Three-Dimensional Computational Fluid Dynamics Approaches for Hydrogen-Fuelled Spark Ignition Engine Simulation," SAE Int. J. Engines 15(4):561-580, 2022, https://doi.org/10.4271/03-15-04-0030.

Proceedings and international conferences

- Millo, F., Rolando, L., Piano, A., Accurso, F. et al., "Synergetic application of 0/1/3D-CFD approaches for hydrogen-fuelled spark ignition engine simulation," 15th International Conference on Engines & Vehicles, Capri, Napoli (Italy), September 12-16, 2021.
- Bianco, A., Piano, A., Millo, F., Roggio, S., et al., "Synergetic application of 0/1/3D-CFD approaches for hydrogen-fuelled spark ignition engine simulation," CONVERGE Application Workshop Hydrogen, Turin, June 20, 2022.
- Piano, A., Millo, F., Roggio, S., Accurso, F. et al., "Dual Fuel H2 Diesel Combustion System Development for Off Highway Applications," CONVERGE Application Workshop Hydrogen, Turin, June 20, 2022.
- Fogla, N., Roggendorf, K., Roggio, S., Piano, A. and Millo, F., "3D-CFD driven development of a 0D empirical model to capture fuel stratification in Direct-Injected Hydrogen engines," SAE International's WCX2023, April 18-20, 2023.